

---


Electronic Theses and Dissertations, 2004-2019

---

2014

## Integrated Microwave Resonator/antenna Structures for Sensor and Filter Applications

Haitao Cheng  
*University of Central Florida*

 Part of the [Electrical and Computer Engineering Commons](#)  
Find similar works at: <https://stars.library.ucf.edu/etd>  
University of Central Florida Libraries <http://library.ucf.edu>

This Doctoral Dissertation (Open Access) is brought to you for free and open access by STARS. It has been accepted for inclusion in Electronic Theses and Dissertations, 2004-2019 by an authorized administrator of STARS. For more information, please contact [STARS@ucf.edu](mailto:STARS@ucf.edu).

---

### STARS Citation

Cheng, Haitao, "Integrated Microwave Resonator/antenna Structures for Sensor and Filter Applications" (2014). *Electronic Theses and Dissertations, 2004-2019*. 6675.  
<https://stars.library.ucf.edu/etd/6675>

INTEGRATED MICROWAVE RESONATOR/ANTENNA STRUCTURES FOR SENSOR  
AND FILTER APPLICATIONS

by

HAITAO CHENG

B.S. University of Electronic Science and Technology of China, 2006

M.S. Shanghai Institute of Microsystem and Information Technology, Chinese Academy of  
Sciences, 2009

A dissertation submitted in partial fulfillment of the requirements  
for the degree of Doctor of Philosophy  
in the Department of Electrical Engineering and Computer Science  
in the College of Engineering & Computer Science  
at the University of Central Florida  
Orlando, Florida

Spring Term  
2014

Major Professor: Xun Gong

© 2014 Haitao Cheng

## ABSTRACT

This dissertation presents design challenges and promising solutions for temperature and pressure sensors which are highly desirable for harsh-environment applications, such as turbine engines. To survive the harsh environment consisting of high temperatures above 1000°C, high pressures around 300 psi, and corrosive gases, the sensors are required to be robust both electrically and mechanically. In addition, wire connection of the sensors is a challenging packaging problem, which remains unresolved as of today. In this dissertation, robust ceramic sensors are demonstrated for both high temperature and pressure measurements. Also, the wireless sensors are achieved based on microwave resonators.

Two types of temperature sensors are realized using integrated resonator/antennas and reflective patches, respectively. Both types of the sensors utilize alumina substrate which has a temperature-dependent dielectric constant. The temperature in the harsh environment is wirelessly detected by measuring the resonant frequency of the microwave resonator, which is dependent on the substrate permittivity. The integrated resonator/antenna structure minimizes the sensor dimension by adopting a seamless design between the resonator sensor and antenna. This integration technique can be also used to achieve an antenna array integrated with cavity filters. Alternatively, the aforementioned reflective patch sensor works simultaneously as a resonator sensor and a radiation element. Due to its planar structure, the reflective patch sensor is easy for design and fabrication. Both temperature sensors are measured above 1000°C.

A pressure sensor is also demonstrated for high-temperature applications. Pressure is detected via the change in resonant frequency of an evanescent-mode resonator which corresponds to cavity deformation under gas pressure. A compact sensor size is achieved with a post loading the

cavity resonator and a low-profile antenna connecting to the sensor. Polymer-Derived-Ceramic (PDC) is developed and used for the sensor fabrication. The pressure sensor is characterized under various pressures at high temperatures up to 800°C. In addition, to facilitate sensor characterizations, a robust antenna is developed in order to wirelessly interrogate the sensors. This specially-developed antenna is able to survive a record-setting temperature of 1300°C.

## ACKNOWLEDGMENTS

I would like to express the sincere appreciation to my advisor, Prof. Xun Gong, for his great support and guidance to finish my Ph.D. dissertation. Along with his cooperation on research projects, he also helps increase my capacities in self-motivation, independence and confidence, which will benefit my future career. Additionally, I would like to thank my dissertation committee members: Prof. Linan An, Prof. Parveen Wahid, Prof. Thomas Wu, and Prof. Vikram Kapoor for their valuable suggestions.

I would like to thank Prof. Chengying Xu, Dr. Siamak Ebadi, Dr. Xinhua Ren, Dr. Gang Shao, Dr. Jian Liu, Dr. Yaohan Chen, Mr. Kyle Harris and Ms. Juan Li who worked closely with me on the sensor project. It has been also a pleasure to work with Dr. Yazid Yusuf and Ms. Tianjiao Li on integrated filter/antenna. In addition, I benefitted a lot during several discussions with Dr. Justin Luther and Mr. Kalyan Karnati. I appreciate the help from Dr. Brian Fisher and Mr. Mark Gallagher in cleanroom. Moreover, I would like to thank Mr. Weijie Zhu, and Mr. Michael Trampler for the support and encourage to my research.

I would like to thank the funding support: the National Science Foundation under Grant ECCS 0823950 and US Department of Energy under Grant DE-FE0001241.

Especially, I wish to express my gratitude to my parents, Fengzhi Sun and Yongyuan Cheng, for their unconditional love.

# TABLE OF CONTENTS

LIST OF FIGURES .....	ix
LIST OF TABLES .....	xvi
1.1 Motivation .....	1
1.2 Desired Characteristics of Sensors for Harsh-Environment Applications .....	4
1.3 Overview of Dissertation .....	7
2.1 Introduction of Filter/Antenna Integration .....	8
2.2 Three-Pole Filter Synthesis .....	9
2.3 Integrated Filter/Antenna Synthesis .....	12
2.4 Fabrication and Measurement Results .....	17
2.5 Conclusion.....	20
3.1 Wireless Sensing Mechanism based on Integrated Resonator/Antenna .....	22
3.1.1 Design of Integrated Resonator/Antenna.....	24
3.1.2 Fabrication and Wireless Interrogation of the Integrated Resonator/Antenna .....	30
3.2 Temperature Sensors using Resonator/Antenna Integration .....	32
3.2.1 Design and Simulation of the Temperature Sensor .....	33
3.2.2 Time-Domain Gating for the Wireless Interrogation.....	36
3.2.3 Fabrication and Measurement of the Temperature Sensor .....	39
3.3 Conclusion.....	43
4.1 Introduction of Reflective Patch Sensors .....	44

4.2	Principle and Design of the Reflective Patch Sensor .....	45
4.2.1	Principle of the Reflective Patch Working as a Temperature Sensor .....	45
4.2.2	Optimized Design of Thickness, Length and Width of the Patch Sensor.....	48
4.3	Wireless Interrogation of the Reflective Patch Sensor.....	53
4.4	Fabrication and Measurement of the Patch Temperature Sensor.....	57
4.5	Conclusion.....	62
5.1	Introduction of Robust Antennas for High-Temperature Applications .....	63
5.2	Design and Analysis of the Proposed Robust Interrogation Antenna.....	65
5.3	Fabrication of the Robust Antenna after Development of Platinum Pattern Process ....	70
5.4	Temperature Sensor Measurement by using the Robust Interrogation Antenna .....	73
5.5	Conclusion.....	75
6.1	Pressure Sensor Mechanism.....	77
6.2	Characterization of the Fully-Dense SiAlCN PDC.....	79
6.3	Design of the Pressure Sensor and Robust Interrogation antenna .....	80
6.3.1	Design of the Pressure Sensor based on an Evanescent-Mode Cavity Resonator ..	80
6.3.2	Design of the Patch Antenna Coupled with the Pressure Sensor.....	83
6.3.3	Design of the Robust Interrogation Antenna with Wide Bandwidth.....	86
6.4	Fabrication of the PDC Pressure Sensor and the Robust Interrogation Antenna.....	90
6.4.1	Fabrication Process of PDC Pressure Sensor.....	90
6.4.2	. Fabrication of the Robust Interrogation Antenna .....	94



6.5	Measurement Setup and Results .....	96
6.6	Conclusion.....	100
7.1	Summary .....	102
7.2	Future Work .....	104
7.2.1	Temperature Sensors for Harsh-Environment Applications.....	104
7.2.2	Pressure Sensors for Harsh-Environment Applications.....	104
7.2.3	Robust Antennas .....	104
7.2.4	Multifunctional Integrated Filters .....	105
	LIST OF REFERENCES .....	106

## LIST OF FIGURES

Figure 1.1: A gas turbine rotor. (Courtesy ALSTOM) .....	2
Figure 1.2: Efficiency and work output versus pressure ratio at different temperatures [1]. .....	3
Figure 2.1: Exploded view of (a) a vertically integrated three-pole filter and (b) a vertically integrated three-pole filter with a slot antenna. The length of Cavity 3 in (b) is less due to the loading effect from the slot antenna. Circuit schematics of (c) the band-pass filter and (d) the integrated filter/antenna. ....	10
Figure 2.2: (a) Bottom view of Cavity 1 of the reference filter. The coupling slot between Cavities 1 and 2 is shown in dashed lines. Cavity 3 is identical to Cavity 1. (b) Top view of Cavity 3 of the filter/antenna. The slot antenna is shown in solid line. ....	11
Figure 2.3: Equivalent circuit of Cavity 3 for the filter/antenna to find $Q_{ext, 2}$ . Metallic and dielectric losses are not included. ....	13
Figure 2.4: Simulated $Q_{ext,2}$ for different slot antenna position $X_a$ with slot antenna length $L_a = 10, 10.5, 11, 11.5, 12, 12.5$ mm. ....	14
Figure 2.5: (a) A dielectrically ( $\epsilon_r = 10.2$ ) loaded feeding waveguide, 8 by 1.6 mm in cross section, is used to design the Cavity 3 length $L_{c3}$ . (b) Simulated $S_{11}$ response of the feeding waveguide for $L_{c3} = 8.2$ mm. ....	15
Figure 2.6: (a) Reflections from coupling structures of the filter. (b) Simulated TD $S_{11}$ responses of the filter and filter/antenna. (c) Simulated $S_{11}$ and $S_{21}$ of the filter compared with $S_{11}$ and gain of the filter/antenna. ....	16
Figure 2.7: (a) Top and (b) bottom view of the fabricated filter/antenna. (b) Measured $S_{11}$ and gain of the filter/antenna. ....	18

Figure 2.8: Simulated and measured radiation patterns of the filter/antenna at the center frequency in (a) H-plane and (b) E-plane. ....	19
Figure 2.9: (a) Inset: photo of the fabricated 2×2 filter/antenna array. Simulated and measured radiation patterns of the 2×2 filter/antenna array at the center frequency in (b) H-plane and (c) E-plane. ....	20
Figure 3.1: Wireless passive sensing using an integrated resonator/antenna with compact size.	23
Figure 3.2: (a) An integrated resonator/antenna weakly coupled by two open-ended coaxial probes. (b) Top view of the resonator/antenna. ....	24
Figure 3.3: Simulated $S_{21}$ response of the resonator/antenna with weak coaxial coupling as shown in Fig. 3.2. ....	26
Figure 3.4: Wireless sensing of resonator/antenna using an OEWG. ....	27
Figure 3.5: Simulated $S_{11}$ of the OEWG for successive distances away from the resonator/antenna before TD gating. ....	27
Figure 3.6: Simulated TD responses of OEWG with or without the resonator at 30 mm distance. A TD gating is performed. ....	28
Figure 3.7: Simulated $S_{11}$ of the OEWG for successive distances away from the resonator/antenna after TD gating. ....	30
Figure 3.8: (a) Top view of the fabricated resonator/antenna, (b) Measurement setup in which the resonator is placed above the OEWG. ....	31
Figure 3.9: Measured $S_{11}$ response for each sensing distance after TD gating. ....	31
Figure 3.10: Wireless sensing of integrated resonator/antenna sensor. ....	33
Figure 3.11: (a) Schematic and (b) equivalent circuit of an open-ended cavity resonator/slot antenna. $W_a = 0.45$ mm, $W_c = 22.86$ mm, thickness = 1.016 mm. ....	34

Figure 3.12: Simulated $Q_{ext}$ for different slot antenna positions $X_a$ and lengths $L_a$ . The resonant frequency is fixed at 5.2 GHz. ....	35
Figure 3.13: Simulated $Q_{ext}$ for different slot width $W_a$ for $L_a = 20$ mm and $X_a = 0.8$ mm. ....	35
Figure 3.14: Simulated $S_{11}$ of the OEWG for successive distances away from the sensor <i>before</i> TD gating. ....	36
Figure 3.15: (a) Schematic of the proposed TD gating process; (b) simulated TD responses of OEWG with and without the sensor. ....	36
Figure 3.16: Simulated $S_{11}$ of the OEWG for successive distances away from the sensor <i>after</i> TD gating.....	37
Figure 3.17: Simulated $S_{11}$ of the OEWG: sensor resonant frequency changes with the dielectric constant of the alumina substrate. ....	38
Figure 3.18: The fabricated temperature sensor. $W_a = 0.45$ mm, $L_a = 20$ mm, $X_a = 0.8$ mm, $W_c = 22.86$ mm, $L_c = 5.93$ mm, $t = 1.016$ mm. ....	39
Figure 3.19: (a) Elevated OEWG for demonstration purpose. (b) The sensor is placed inside the heat pad with alumina board cover. ....	40
Figure 3.20: Measured $S_{11}$ responses of the OEWG for different temperatures. ....	41
Figure 3.21: Measured resonant frequency of the sensor and extracted dielectric constant of alumina versus temperature. ....	41
Figure 3.22: Measured Q factor of the sensor versus temperature. ....	42
Figure 4.1: Flow chart of the proposed wireless passive temperature sensing mechanism.....	45
Figure 4.2: 3-D views of the sensor structure in HFSS. An OEWG is used as the interrogation antenna to detect the reflective patch sensor.....	46

Figure 4.3: Electric field distributions inside the dielectric substrate at (a) resonant frequency $f_r = 5.05$ GHz (b) lower frequency $f_l = 5.00$ GHz (c) higher frequency $f_2 = 5.10$ GHz. ....	47
Figure 4.4: Coaxial weak coupling to simulate the $Q_T$ of the reflective patch in HFSS. ....	49
Figure 4.5: $S_{11}$ response by using the coaxial weak coupling probe. ....	49
Figure 4.6: Design of the alumina substrate thickness. In the simulation, $L = W = 9.3$ mm. ....	50
Figure 4.7: Reflective patch width design. The patch length and thickness are $L = 9.3$ mm and $h = 0.0635$ mm, respectively. ....	53
Figure 4.8: TD gating process: (a) Simulated $S_{11}$ of the OEWG antenna. (b) Compare of $S_{11}$ responses of the OEWG antenna along and the OEWG antenna with the reflective patch. (c) Responses for different sensing distances after the TD gating. ....	54
Figure 4.9: Simulated $S_{11}$ at the input port of the OEWG for various dielectric constants of the alumina substrate. ....	55
Figure 4.10: Simulated resonant frequency of the patch sensor for various dielectric constants of the alumina substrate. ....	56
Figure 4.11: Ground effect on the response of reflective patch after TD gating. ....	57
Figure 4.12: Top (a) and bottom (b) view of the fabricated reflective patch sensor. $W = 8$ mm, $L = 9.3$ mm, $L_g = 21$ mm. The thickness of alumina substrate is $h = 0.635$ mm. ....	58
Figure 4.13: (a) Elevated OEWG for demonstration purpose. (b) The sensor is placed inside the heat pad with alumina board cover. (c) Schematic of wave reflections due to the alumina board cover with $d = 0.635$ mm. ....	59
Figure 4.14: Measured $S_{11}$ at successive temperatures up to $1100^\circ\text{C}$ . Resonant frequency decreases with the increase in temperature. ....	60
Figure 4.15: Simulated and Measured resonant frequency of the sensor versus temperature. ....	61

Figure 5.1: Schematic of measurement setup using a robust interrogation antenna.....	64
Figure 5.2: Schematic of wireless sensing system in harsh environment with proposed interrogation slot antenna.....	64
Figure 5.3: Structure of the slot antenna with a tuning stub. ....	65
Figure 5.4: Simulated $S_{11}$ responses for various antenna parameters: (a) slot width $W_s$ . (b) tuning- stub width $W_t$ . (c) tuning-stub length $L_t$ . (d) slot length.....	67
Figure 5.5: Electric field distributions in the slot area at (a) 9.6 GHz, (b) 10.6 GHz and (c) 11.4 GHz. The equivalent magnetic currents are labeled. ....	68
Figure 5.6: Radiation pattern of the slot antenna. (a) E-plane. (b) H-plane. ....	70
Figure 5.7: Fabrication of the slot antenna. (a) Antenna layout on transfer paper. (b) Antenna layout transferred to alumina substrate. (c) Pattern of the platinum paste. (d) Platinum after high temperature sintering. (e) Fabricated antenna.....	72
Figure 5.8: (a) TRL calibration kits. (b) Measured and simulated $S_{11}$ response of the slot antenna at room temperature. ....	73
Figure 5.9: Measurement setup. (a) The interrogation antenna and the sensor/ antenna. (b) The interrogation antenna and sensor located in the furnace. ....	74
Figure 5.10: Measurement of the temperature sensor using $Si_4B_1CN$ substrate.....	75
Figure 6.1: Schematic of the wireless pressure sensor based on an evanescent-mode cavity resonator.....	78
Figure 6.2: Characterization of dielectric properties of the $SiAlCN$ PDC in a microwave cavity at room temperature. ....	79
Figure 6.3: Flow chart to design the microwave pressure sensor. ....	81

Figure 6.4: Optimized design of the evanescent-mode-resonator pressure sensor. (a) Side view with dimensions. (b) Simulated resonant frequency of the pressure sensor versus cavity gap. ... 82

Figure 6.5: Mechanical simulations of the pressure sensor under 600 psi pressure. (a) Sensor deformation. (b) Stress distribution. .... 83

Figure 6.6: Top (left) and 3-D (right) view of the patch antenna integrated with the pressure sensor. The patch antenna is at the top surface of the ceramic cap. The coupling aperture is at the bottom surface of the ceramic cap. .... 84

Figure 6.7: (a) Simulation setup for the wireless interrogation of the pressure sensor in HFSS. Parametric study of (b) patch length  $L_a$ . (c) coupling position  $X_p$  for the integrated patch antenna. (d) Sensor responses versus different gap sizes inside the cavity. .... 85

Figure 6.8: Interrogation antenna for pressure sensor measurement at high temperatures. (a) The schematic of the pressure sensor measurement with the interrogation antenna. (b) The schematic of the slot antenna loaded with a rectangular tuning stub. .... 87

Figure 6.9: Parameter study of (a) the slot length  $L_s$ , (b) the slot width  $W_s$ , (c) the tuning-stub width  $W_t$  and (d) the tuning-stub length  $L_t$  of the interrogation antenna. .... 88

Figure 6.10: Fabrication process flow of the PDC cavity bottom. (a) Machining of the Teflon mould. (b) Liquid ceramic precursor in the mould. (c) UV exposure. (d) Polymer demoulding. (e) PDC sintering. (f) Photos of the polymer (right) and sintered PDC (left). .... 90

Figure 6.11: (a) Top view and (b) 3-D profile of the PDC cavity bottom after the platinum metallization. (c) Cavity dimensions after fabrication. .... 92

Figure 6.12: Platinum metallization and bonding process. (a) The coupling aperture on the ground plane of the patch antenna. (b) The patch antenna. (c) The bonded pressure sensor consisting of both PDC cavity bottom and cap. .... 93

Figure 6.13: Fabrication of the robust interrogation antenna. (a) Antenna layout on a transfer paper. (b) Window cutting on an alumina substrate. (c) Antenna layout transered to the alumina substrate. (d) Pattern of platinum paste. (e) Platinum pattern after high temperature sintering. .. 95

Figure 6.14: The measurement of the interrogation antenna. (a) Fabricated TRL calibration kits. (b) The measured  $S_{11}$  response of the interrogation antenna. .... 96

Figure 6.15: The measurement setup. (a) Pressure sensor measurement under high temperatures and external forces. (b) The external force is applied on the pressure sensor which is below the interrogation antenna. .... 97

Figure 6.16: (a) Measured resonant frequency  $f_r$  of the pressure sensor versus the applied force at each temperature. (b) Extracted deflection of the pressure sensor cap due to the applied force at different tempertures. .... 98

Figure 6.17: Mechanical analysis of the pressure sensor. (a) The pressure sensor under test simulated in ANSYS. (b) Simulated sensor deformation for different Young's modulus of the PDC. (c) Extracted Young's modulus of the PDC versus temperature. .... 100

Figure 7.1: Summary map of this dissertation. .... 102



## LIST OF TABLES

Table 2.1: Parameter dimensions for the Cavity 1 (a) and Cavity 3 (b). .....	12
Table 3.1: Parameter dimensions to simulate the integrated resonator/antenna in Fig. 3.2. ....	25
Table 4.1: Compare of different microwave high temperature sensors based on alumina. ....	62
Table 5.1: Dimensions of the designed slot antenna.....	68
Table 6.1: The dimensions of the patch antenna.....	86
Table 6.2: The dimensions of the interrogation antenna.....	89

# CHAPTER 1 INTRODUCTION

This chapter introduces background of sensors for harsh-environment applications. The desired characteristics of sensors are analyzed based on the requirements in harsh environment. Additionally, the organization of this dissertation is presented.

## 1.1 Motivation

Real-time monitoring of physical parameters, including temperature and pressure, is highly desirable for harsh-environment applications, such as gas turbine engines. Today gas turbine engines are replacing steam turbines rapidly for power generation throughout the world, owing to the merits of compact volume, low weight and fuel versatility [1]. To improve fuel efficiency of a gas turbine, firing temperatures and pressure ratios have been increased continually in the past 50 years. The firing temperature is elevated from 750 to 1400°C, and the pressure ratio is increased from 7:1 to 40:1, respectively. To better understand the gas turbine environment, Fig. 1.1 presents a gas turbine working with a high pressure ratio of 35:1. During the turbine operation, temperature and pressure are the two most important parameters measured in a turbine monitoring system to achieve the optimal efficiency.

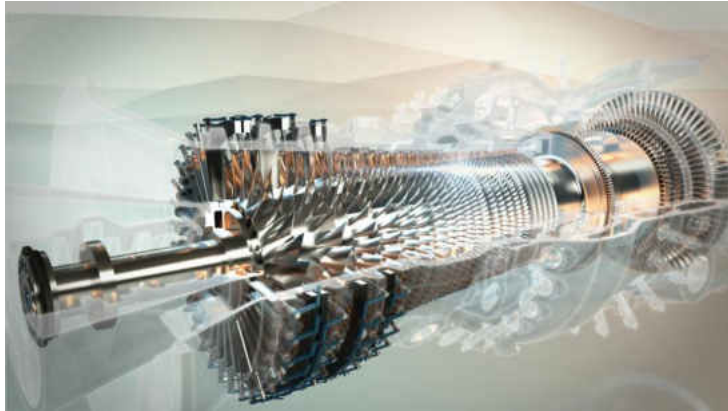


Figure 1.1: A gas turbine rotor. (Courtesy ALSTOM)

Temperature measurement is critical for gas turbine performance, due to the fact that temperatures prominently affect the efficiency, reliability and emission of a gas turbine. As shown in Fig. 1.2, the work output increases about 10% for every elevated firing temperature of 55°C. With temperature measurements at turbine exhaust, compressor inlet and discharge, a gas turbine can be controlled to work at designed temperatures. Therefore, fuel cost can be decreased by achieving high thermal efficiency.

In addition, temperature monitoring of turbine components is essential for improving the turbine reliability and turbine blade life [2]. The temperature of turbine metal blade is required to be below 700°C to minimize severe hot corrosion [3]. Temperature measurement of bearings is also necessary to avoid the bearing overheating or failure.

NO<sub>x</sub> emission can be controlled with temperature monitoring. NO<sub>x</sub> emission is increased due to oxidation of nitrogen at high temperatures in combustors [4]. Therefore, temperature sensors are

required to detect the temperature in the combustor, and then communicate with the control system in a turbine engine.

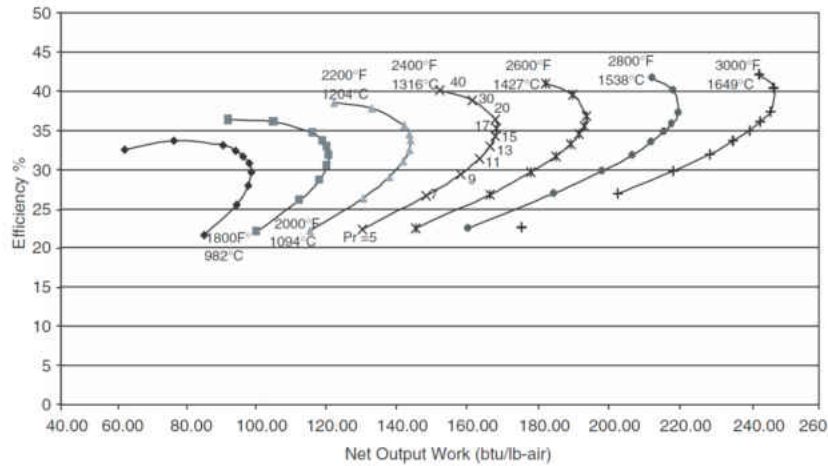


Figure 1.2: Efficiency and work output versus pressure ratio at different temperatures [1].

Pressure monitoring is also important to achieve high efficiency and reliability of a gas turbine. As presented in Fig. 1.2, there is an optimal pressure ratio to achieve the maximal thermal efficiency, for a given temperature. Pressures beyond or below the optimal value will result in a reduced thermal efficiency. Pressure measurements are normally carried out at compressor exhaust, turbine inlet and turbine exhaust to maintain the maximal thermal efficiency.

Additionally, online monitoring of pressure inside a gas turbine is necessary for safe operations. Higher pressure ratios than the designed value could lead to compressor surge which results in flameout, or even serious damage to compressor blades.

## 1.2 Desired Characteristics of Sensors for Harsh-Environment Applications

In order to improve turbine efficiency and reliability, temperature and pressure sensors are critical for condition monitoring. These sensors are required to work properly in the harsh environment consisting of high temperatures (1000-1400°C), high pressures (300-600 psi), and corrosive gases (containing sodium, vanadium and sulfate). Temperature and pressure sensors with passive, wireless, robust and compact characteristics are highly desirable to survive this harsh environment.

Sensors for such high-temperature applications are required to be passive, since active sensors that contain amplifying components and circuits fail at high temperatures [5]. Silicon carbide (SiC) and gallium nitride (GaN), as wide band-gap semiconductors, appear to be strong candidates for high-temperature integrated circuits. Junction-field-effect transistor (JEFT) and high-electron-mobility transistor (HEMT) are realized working at temperature of 600°C by using SiC [6]-[7] and GaN [8], respectively. Additionally, SiC high-temperature circuits are demonstrated up to 450°C for temperature [9] and pressure [10] detections. However, they are not suitable for turbine applications due to the limited operation temperature.

Alternatively, passive structures are widely adopted for sensor applications, such as interferometer-based temperature sensors [11], resistive [12]-[13] and capacitive [14]-[15] pressure sensors. All these sensors are wire connected for high-temperature applications, which is challenging for turbine applications.

Wireless sensors are strongly desirable, since the challenging electrical contacts and sensor packaging are avoided. Today resistive thermal detectors (RTD) and thermocouples that need

wire interconnection are mostly used as temperature sensors for turbine engines [16]. However, drilling holes that involves costly and complicated process [17], is required for sensor mounting to a gas turbine wall [18].

To solve this problem, wireless sensors for harsh-environment applications are proposed based on LC resonators and Surface Acoustic Wave (SAW) devices. Based on LC resonators, pressure and temperature sensors are realized by measuring capacitors that are pressure-dependent [19]-[20] and temperature-dependent [21], respectively. These sensors are wirelessly detected by using inductive coupling between the sensor inductors and reader antennas [22]. However, this inductive coupling approach suffers from low quality (Q) factors especially at high temperatures, which limits the measurement resolution and sensing range. Wireless passive surface acoustic wave (SAW) temperature sensors were realized based on Langasite (LGS) substrate up to 900°C [23]-[24]. The highest working temperatures of SAW sensors are limited by piezoelectric substrates which undergo phase transformation and chemical instability at high temperatures [25]. Additionally, the strong increasing acoustic loss of LGS substrate with frequency prohibits its applications above 1 GHz [26], and therefore results in a bulky antenna size.

The harsh environment in gas turbines requires sensors to survive high temperatures and corrosive gases. Therefore, robust materials are briefly introduced herein to facilitate the sensor design. Alumina ( $\text{Al}_2\text{O}_3$ ) has been identified as one of the robust materials for harsh environment applications by researchers at NASA Glenn Research Center in recent years. The material properties of alumina at microwave frequencies are characterized by presenting a coplanar waveguide (CPW) [27] and a CPW-fed folded slot antenna (FSA) [28] patterned on an alumina

substrate up to 400°C. Alumina substrate is also used to realize inductors operating up to 475°C [29]. It is shown in [30] that the dielectric constant of alumina is strongly temperature-dependent and monotonically increases up to 1600°C, which is a desirable characteristic for temperature sensor applications.

Silicon carbonitride (SiCN) ceramic exhibits excellent thermal and mechanical stabilities at high temperatures [31]-[32]. Other silicon-based ceramics, such as silicoboron carbonitride (SiBCN) [33] and silicoaluminum carbonitride (SiAlCN) [34]-[35], present remarkably high resistance to water-vapor, oxidation and salt corrosion at high temperatures. The outstanding thermal and mechanical stabilities of SiCN ceramic are highly attractive for pressure sensors working at high temperatures. Additionally, the dielectric constant of SiCN ceramic monotonically increases with temperature [36], which is a desirable property for temperature sensing. In addition, by using polymer-derived ceramic (PDC), the SiCN ceramic can be fabricated with a polymer precursor [37]-[38]. This feature shows a significant benefit for ceramic machining, given that the polymer precursor can be patterned before the ceramic sintering.

Microwave sensors are promising due to the passive, wireless and compact structures. Wireless and passive strain sensors were proposed in [39] and [40], based on the fact that the resonant frequency of a microwave resonator is determined by cavity deformation due to external strain applied on the resonator sensor. By using evanescent-mode resonators [41] for sensor applications, high sensor sensitivity and compact volume can be achieved. Evanescent-mode based sensors were demonstrated successfully to wirelessly detect pressure [42]-[43] and air flow [44]. However, all the mentioned microwave sensors are not for high-temperature applications.

By adopting robust materials, microwave sensors can be used for harsh-environment applications. Microwave temperature sensors using SiCN ceramic were presented in [45]-[46], in which the dielectric constant of the ceramic substrate is determined by the temperature. However, the total volume of the microwave sensor is dominated by the antenna size, which is due to the separated design of sensors and antennas. This problem will be solved in this dissertation by using resonator/antenna integration.

### 1.3 Overview of Dissertation

This dissertation presents robust ceramic sensors for high temperature and pressure measurements. Sensor interrogation is wirelessly achieved by adopting integrated sensor/antenna structures and robust interrogation antennas. Chapter 2 shows a vertically integrated three-pole filter/antenna, and an antenna array is designed based on this integration technique. In Chapter 3, a temperature sensor is realized for high-temperature applications, based on resonator/antenna integration. Additionally, Chapter 4 presents a temperature sensor by using a reflective patch working at high temperatures. In order to validate sensor interrogations, Chapter 5 shows the design and fabrication of a robust interrogation antenna. In addition, Chapter 6 presents a pressure sensor based on an evanescent-mode resonator for high-temperature applications. Finally, Chapter 7 summarizes this dissertation, and future work is suggested.



## CHAPTER 2      VERTICALLY INTEGRATED THREE-POLE FILTER/ANTENNAS FOR ARRAY APPLICATION

This chapter presents about an integration method for the filters and antennas. The vertically integrated slot antenna above the three-pole cavity filter occupies negative volume and exhibits high efficiency. Finally, a four-element antenna array is demonstrated based on this integration technique.

### 2.1 Introduction of Filter/Antenna Integration

There is an increasing demand for high-performance and compact RF front-end circuits. High-Q-factor resonators can reduce the insertion loss of a filter and help improve the signal-to-noise ratio of a communications system. Waveguide cavity resonators are popular choices for low-loss filters due to their high Q factors. In order for them to be used in an antenna array in which the spacing between antenna elements is usually less than one wavelength, vertically integrating the resonators using silicon micromachining [47] or low-temperature co-fired ceramics (LTCC) [48]-[49] is an effective way to reduce the footprint.

However, the aforementioned techniques require the use of standard 50-ohm connections such as microstrip-to-slot transitions to connect to the antenna. This approach often renders extra loss or undesirable substrate modes. All the losses from the antenna and filter as well as the transitions between the two are directly translated into the noise figure of a receiver system. Therefore, it is desirable to design low-loss filters and antennas as an inseparable unit to reduce the loss and minimize the volume simultaneously.

Recently, seamless integration of a four-pole cavity filter with a slot antenna was presented in [50]. This chapter extends the aforementioned work in two aspects. First, a three-pole vertical filter is employed in this work to reduce the footprint. Second, a  $2 \times 2$  antenna array consisting of the proposed integrated filter/antenna unit cells is presented for the first time.

In this work, we will present the vertical integration of a high-Q-factor ( $\sim 820$ ) three-pole cavity filter and a high-efficiency (97%) slot antenna. Near-zero transition loss is achieved between the filter and antenna. The total loss of the entire filter/antenna system is almost identical to the filter insertion loss alone. The footprint of  $0.43 \lambda_0 \times 0.55 \lambda_0$  of a single filter/antenna unit cell enables antenna arrays without grating lobes. A  $2 \times 2$  filter/antenna array is designed, fabricated, and measured.

## 2.2 Three-Pole Filter Synthesis

Before the integrated filter/antenna is designed, a reference three-pole filter as shown in Fig. 2.1(a) is synthesized. Then a three-pole filter/antenna is realized by replacing one coaxial port of the filter with a slot antenna as shown in Fig. 2.1(b). The circuit schematics of the cavity filter and the integrated filter/antenna are shown in Fig. 2.1(c) and Fig. 2.1(d), respectively. It should be noted that designing the integrated antenna without using standard 50-ohm transitions requires rigorous synthesis methods.

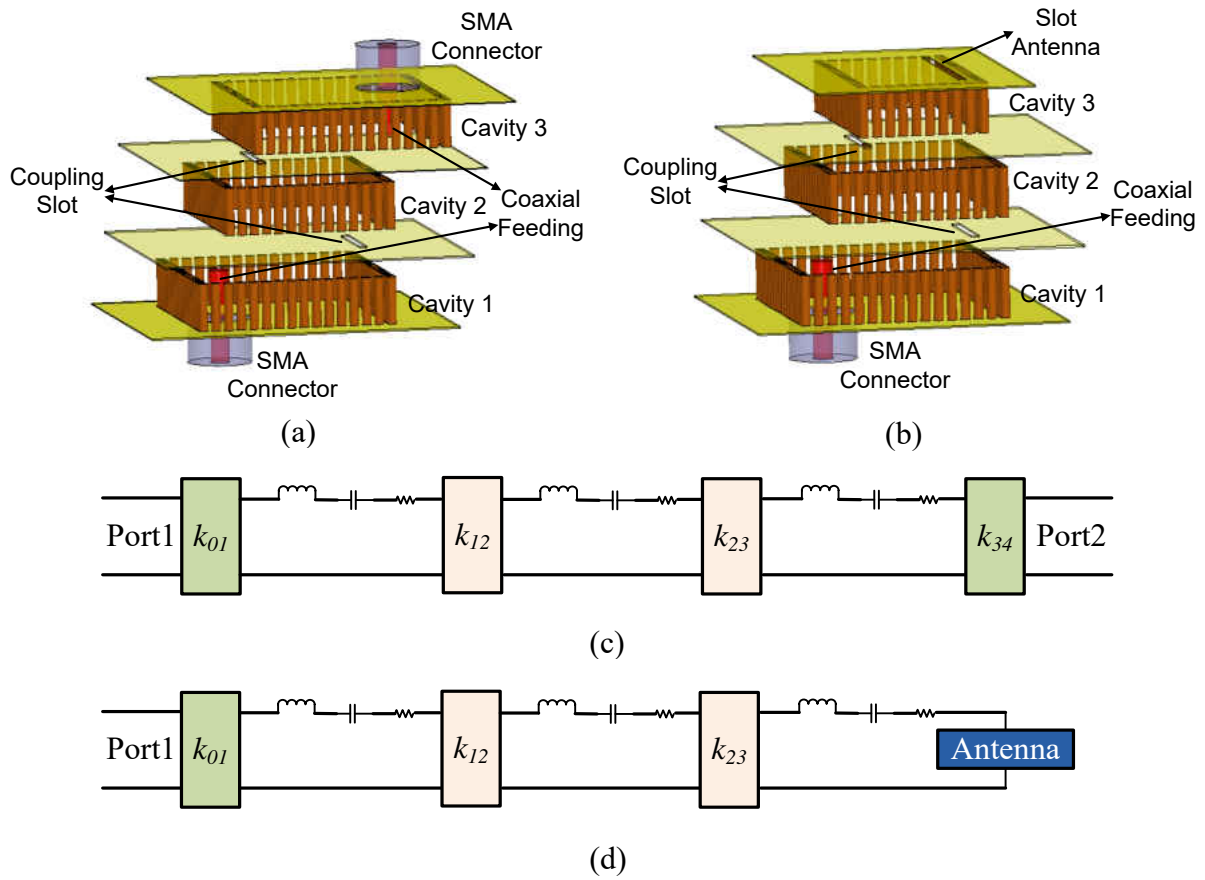


Figure 2.1: Exploded view of (a) a vertically integrated three-pole filter and (b) a vertically integrated three-pole filter with a slot antenna. The length of Cavity 3 in (b) is less due to the loading effect from the slot antenna. Circuit schematics of (c) the band-pass filter and (d) the integrated filter/antenna.

A three-pole cavity filter is designed using standard filter synthesis techniques [51]. The center frequency and bandwidth of the filter are 9.98 GHz and 5.3%, respectively. As shown in Fig. 2.1(c), the internal and external coupling coefficients of the band-pass filter are:

$$k_{12} = k_{23} = 0.036 \quad (2.1)$$

$$Q_{ext,1} = Q_{ext,2} = 26.2 \quad (2.2)$$

This filter consists of three layers of 3.18-mm-thick RT/Duroid 5880 substrates. Sidewalls of the resonators are formed by rows of copper vias as shown in Fig. 2.2. The diameter and separation of the vias are 0.635 and 0.2 mm, respectively. Compared with the wavelength at X-band, this separation is so small that the energy leakage through the sidewalls is negligible.

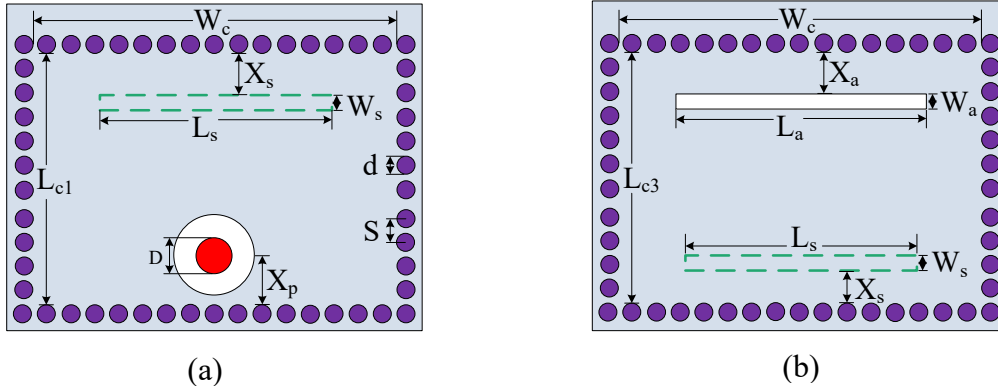


Figure 2.2: (a) Bottom view of Cavity 1 of the reference filter. The coupling slot between Cavities 1 and 2 is shown in dashed lines. Cavity 3 is identical to Cavity 1. (b) Top view of Cavity 3 of the filter/antenna. The slot antenna is shown in solid line.

The external coupling is achieved by shorted-ended coaxial connection, which provides magnetic coupling. The coupling value can be adjusted by changing  $X_p$ . Stronger external coupling occurs at a larger  $X_p$ . The internal coupling between the resonators is realized by creating open slots in their common ground plane. Stronger internal coupling occurs with a smaller  $X_s$  and larger  $L_s$  since the magnetic field is stronger at the perimeter of the cavity resonator.

The dimensions and positions of these coupling structures are optimized using Ansoft High Frequency Structure Simulator (HFSS) to realize the design parameters in (1) and (2) [51]. The

lengths of the three resonators are designed to be:  $L_{c1} = L_{c1}' = 16.6$  mm, and  $L_{c2} = 14.4$  mm. All other dimensions of the reference filter are listed in Table 2.1. The insertion loss of this filter is found to be 0.53 dB, corresponding to an unloaded Q factor of 820 for each of the cavity resonators.

Table 2.1: Parameter dimensions for the Cavity 1 (a) and Cavity 3 (b).

(a)									
Parameters	$W_c$	$L_{c1}$	$S$	$d$	$D$	$X_p$	$L_s$	$W_s$	$X_s$
Dimensions (mm)	13	16.6	0.87	0.635	1.27	2.2	6.1	0.5	1.5

(b)								
Parameters	$W_c$	$L_{c3}$	$L_a$	$W_a$	$X_a$	$L_s$	$W_s$	$X_s$
Dimensions (mm)	13	7.8	11.5	0.5	1	6.1	0.5	1.5

### 2.3 Integrated Filter/Antenna Synthesis

As shown in Fig. 2.1(b), no intermediate transition structure is needed between the filter and antenna in the proposed integration approach. In addition, the slot antenna utilizes the existing volume of one resonator of the filter as its substrate and therefore represents zero-added volume. It will be demonstrated that there is near-zero transition loss between the filter and antenna. Moreover, antenna efficiency as high as 97% will be achieved over a 5.3% fractional bandwidth of the filter/antenna system.

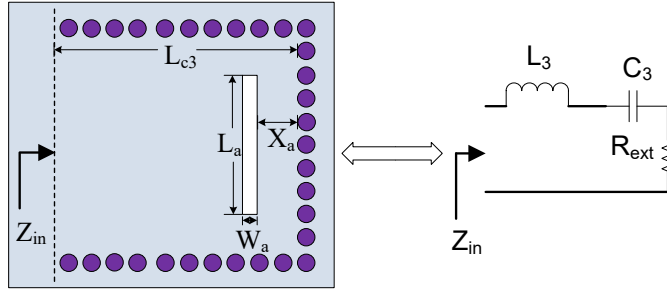


Figure 2.3: Equivalent circuit of Cavity 3 for the filter/antenna to find  $Q_{ext, 2}$ . Metallic and dielectric losses are not included.

The slot antenna is directly etched on the top surface of the third cavity as shown in Fig. 2.3. The structure acts as an equivalent series  $RLC$  resonator at the center frequency of filter. The coupling between the slot antenna and cavity resonator is controlled by antenna length  $L_a$  and location  $X_a$ .  $Q_{ext,2}$  from the slot antenna can be extracted using [50]:

$$Q_{ext,2} = \frac{\omega_0}{2 \operatorname{Re}(Z_{in}(\omega_0))} \left. \frac{d(\operatorname{Im}(Z_{in}))}{d\omega} \right|_{\omega=\omega_0} \quad (2.3)$$

where  $Z_{in}$  is the input impedance of the structure at the reference plane shown in Fig. 2.3. In simulations, the metallic and dielectric losses are set to zero, and  $L_{c3}$  is adjusted to make the structure resonant at the center frequency.

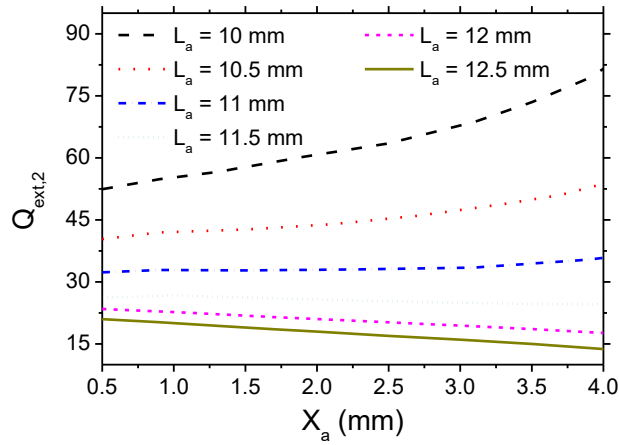


Figure 2.4: Simulated  $Q_{ext,2}$  for different slot antenna position  $X_a$  with slot antenna length  $L_a = 10, 10.5, 11, 11.5, 12, 12.5$  mm.

As shown in Fig. 2.4,  $Q_{ext,2}$  is dependent on both the dimension and position of the slot antenna.

This figure can be used as the design chart for synthesis of these two parameters. Finally,  $L_a$  and  $X_a$  are selected to be 11.5 and 1 mm, respectively, to realize  $Q_{ext,2}$  of 26.2.

In this design,  $L_{c3}$  of 9.1 mm is found to achieve the resonant frequency of 9.98 GHz. As presented in Fig. 2.5, Cavity 3 is excited by a feeding waveguide to take into account the frequency loading effect due to coupling slot.  $L_{c3}$  is then adjusted to be 8.2 mm.

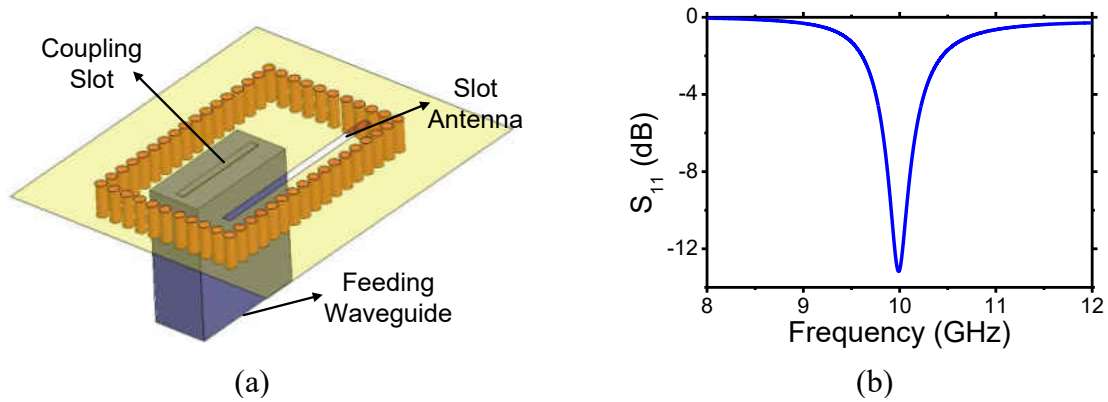


Figure 2.5: (a) A dielectrically ( $\epsilon_r = 10.2$ ) loaded feeding waveguide, 8 by 1.6 mm in cross section, is used to design the Cavity 3 length  $L_{c3}$ . (b) Simulated  $S_{11}$  response of the feeding waveguide for  $L_{c3} = 8.2$  mm.

It was shown in [50] that frequency-domain synthesis alone can provide a close but not exact matching between the filter and filter/antenna responses. To avoid the time-consuming optimization using full-wave simulations, a time-domain filter analysis technique, which was described in detail in [52], is used here to match the filter and filter/antenna responses with one parametric sweep in HFSS.

As shown in Fig. 2.6(a), reflections occur at external and internal coupling structures of the filter. Therefore, four peaks correspond to  $Q_{ext,1}$ ,  $k_{12}$ ,  $k_{23}$  and  $Q_{ext,2}$ , respectively, are shown in Fig. 2.6(b). Additionally, the three dips indicate the resonances of the three resonators. After performing the parametric sweep in HFSS and comparing the TD responses, the length of cavity 3,  $L_{c3}$ , is found to be 7.8 mm. All dimensions and positions of the slot antenna and cavity 3 of the filter/antenna are listed in Fig. 2.2(b).



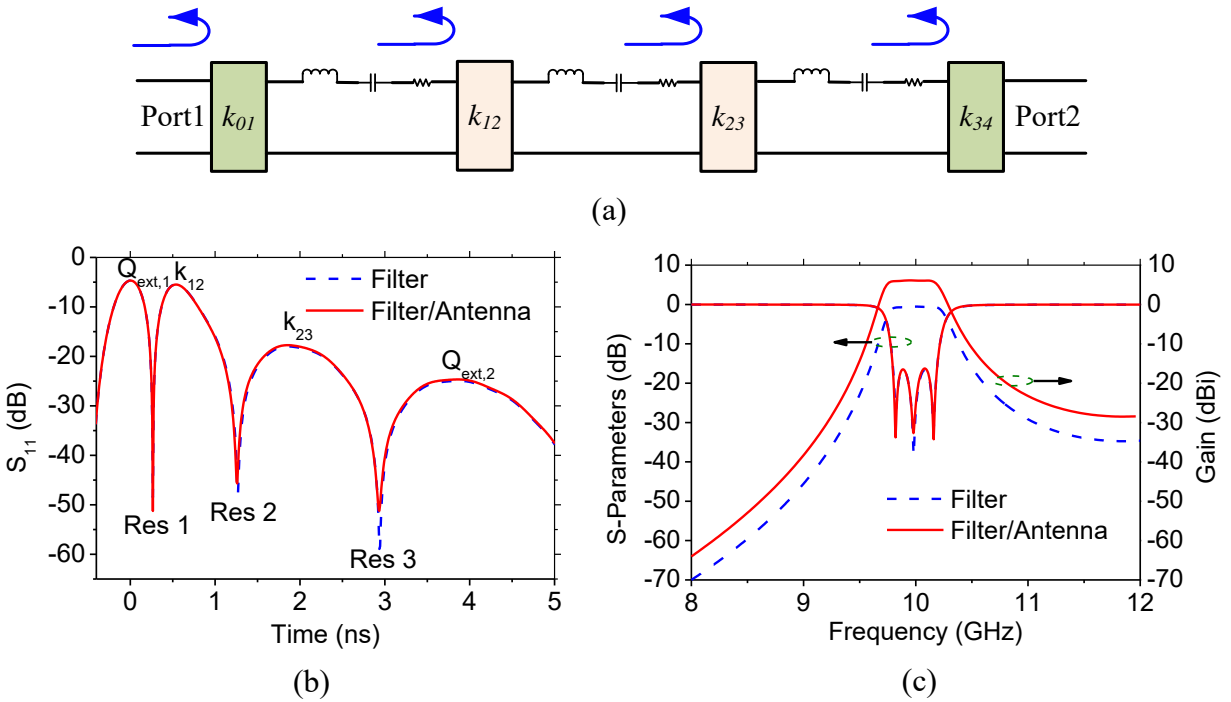


Figure 2.6: (a) Reflections from coupling structures of the filter. (b) Simulated TD  $S_{11}$  responses of the filter and filter/antenna. (c) Simulated  $S_{11}$  and  $S_{21}$  of the filter compared with  $S_{11}$  and gain of the filter/antenna.

The TD reflection coefficients of the filter and filter/antenna are found to be identical as shown in Fig. 2.6(b). Therefore, their frequency-domain reflection coefficients also match very well as shown in Fig. 2.6(c). Both the filter and filter/antenna have the same center frequency of 9.98 GHz and bandwidth of 5.3%. The designed return loss is larger than 17.3 dB within the passband.

Fig. 2.6(c) also shows the  $S_{21}$  of the filter and gain of the filter/antenna. It is apparent that the filter/antenna exhibits the same filtering function as the filter itself, which means the integration of slot antenna does not compromise the filtering shape. It is noted that the intrinsic bandwidth of the slot antenna should be greater than that of the filter [50]. The simulated gain and directivity are 6.10 and 6.77 dBi, respectively. Therefore, the overall efficiency of the filter/antenna in

simulations is found to be 86% (0.67 dB loss), which includes the 0.53-dB filter insertion loss. The difference between the two, i.e. 0.14 dB, corresponds to a 97% antenna efficiency.

## 2.4 Fabrication and Measurement Results

Each cavity layer is separately fabricated using standard PCB process. The vias are metallized using copper electroless plating followed by copper electroplating. Then the three cavity resonators are bonded together to form the vertical filter/antenna. Tin/indium is chosen to facilitate the metal-to-metal bonding between adjacent layers.

The bonding process flow is described as follows. First, tin/indium layers of approximately 10  $\mu\text{m}$  thick are applied on the copper ground planes. Then the three layers are aligned using alignment pins located at the four corners of the substrate as shown in Fig. 2.7(a). After that, a pressure of 2 MPa is uniformly applied on the aligned parts using a clamp apparatus. Finally the compressed multi-layer structure is placed into a reflow oven for 6 minutes at 200 °C to form a solid bonding. The photos of the fabricated filter/antenna are shown in Fig. 2.7(a) and 6(b).

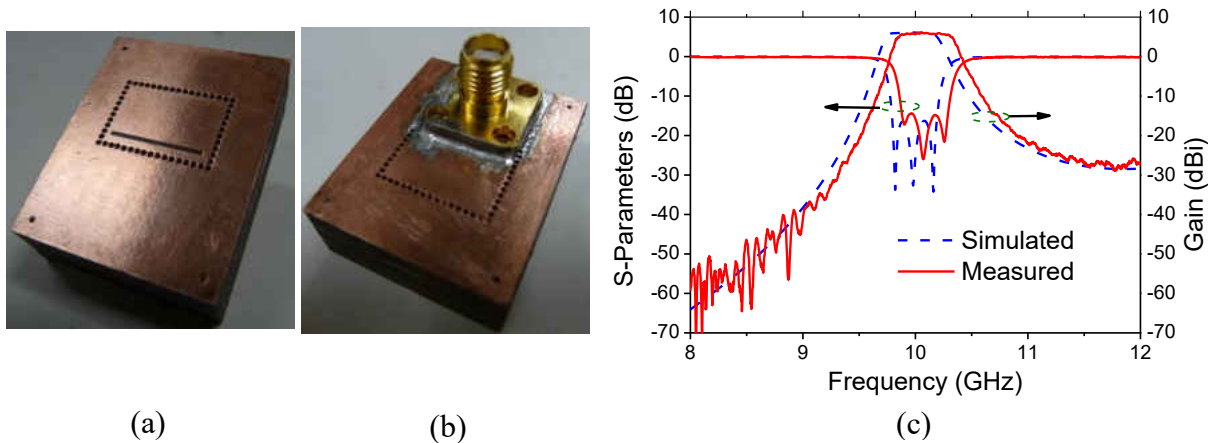


Figure 2.7: (a) Top and (b) bottom view of the fabricated filter/antenna. (c) Measured  $S_{11}$  and gain of the filter/antenna.

An SMA connector is soldered to Cavity 1 for measurement purposes. The measured  $S_{11}$  and gain of the filter/antenna are compared with simulation results in Fig. 2.7(c). The measured  $S_{11}$  is below -14.5 dB across the entire bandwidth. The measured bandwidth of 5.5% is very close to the simulated bandwidth of 5.3%. The 0.9% difference between the measured and simulated resonant frequencies, i.e. 10.07 and 9.98 GHz, respectively, is mainly due to the fabrication tolerances. The measured gain is 6.0 dBi, which is very close to the simulated 6.1 dBi. Therefore, the antenna efficiency is found to be 95% by taking the ratio between the measured gain and simulated directivity. The radiation patterns in both H and E-planes are shown in Fig. 2.8. Very close agreement is found between the simulated and measured results.

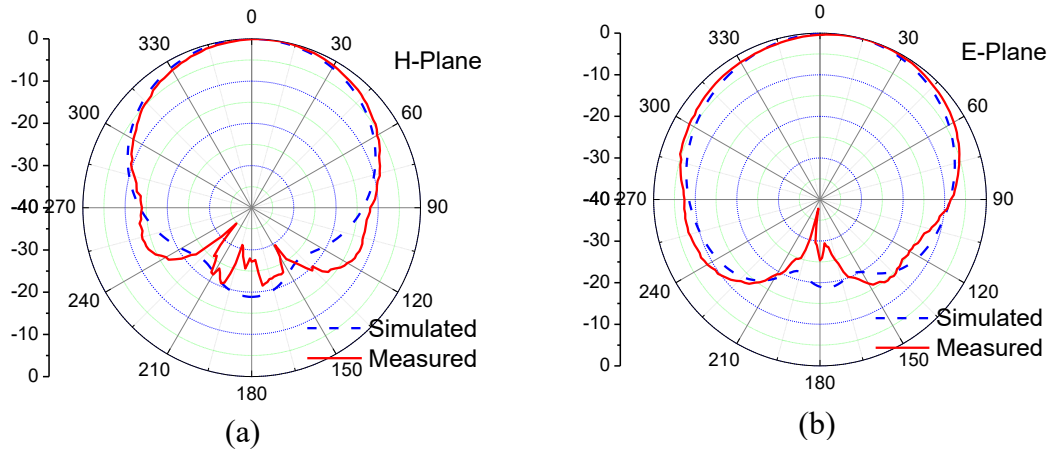
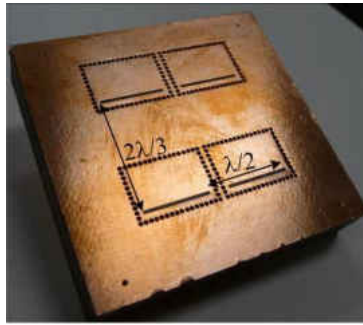
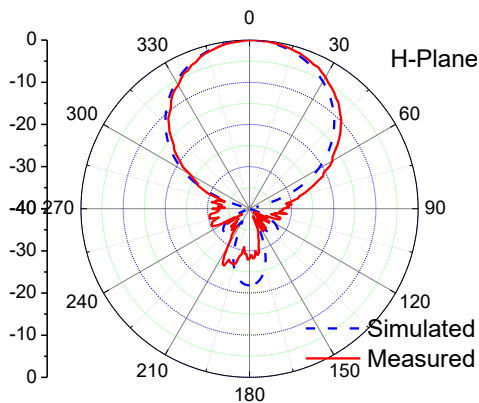


Figure 2.8: Simulated and measured radiation patterns of the filter/antenna at the center frequency in (a) H-plane and (b) E-plane.

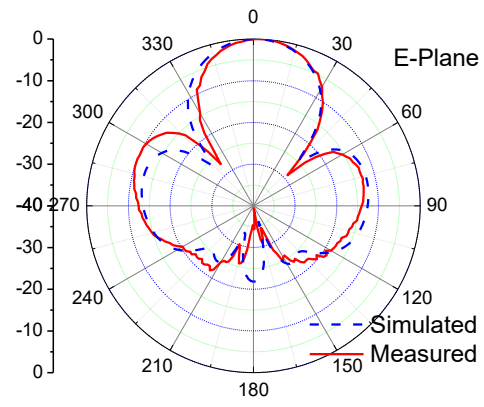
A  $2 \times 2$  filter/antenna array is fabricated and shown in Fig. 2.9(a). The spacing between antenna elements is  $\lambda/2$  in H-plane and  $2\lambda/3$  in E-plane. To measure the array, a four-way power divider is used to split the input power equally and feed each array element. By calibrating the loss of the power divider and connecting cables, the measured gain is 11.4 dBi, which is 0.3 dB lower than the simulated 11.7 dBi. The radiation patterns in both H and E-planes of the array are shown in Fig. 2.9(b) and 9(c), respectively. Again, very close agreement is apparent between simulation and measurement.



(a)



(b)



(c)

Figure 2.9: (a) Inset: photo of the fabricated  $2 \times 2$  filter/antenna array. Simulated and measured radiation patterns of the  $2 \times 2$  filter/antenna array at the center frequency in (b) H-plane and (c) E-plane.

## 2.5 Conclusion

A three-pole vertical cavity filter has been seamlessly integrated with a slot antenna. A synthesis method has been proposed to achieve the same response from the integrated filter/antenna. At the same time, good radiation characteristic is also achieved. Using the proposed integration method, the antenna exhibits zero-added volume and high efficiency. The integrated filter/antenna has a small footprint and therefore antenna arrays without grating lobes can be realized with high-Q

filtering functions. A four-element array of the proposed structure has also been successfully demonstrated. This technique could be extended for large phased array antennas with increased efficiency and reduced co-site interference. The thickness/volume/weight of the filter/antenna can be further reduced using substrates with higher dielectric constant.

It should be noticed that this resonator/antenna integration technique is also used for the microwave sensors which will be described in the following chapters.

## CHAPTER 3      A TEMPERATURE SENSOR BY USING CAVITY RESONATOR/ANTENNA INTEGRATION

Inspired by the filter/antenna integration in chapter 2, this chapter presents a wireless temperature sensor based on an integrated resonator/antenna for high-temperature applications. After demonstration of wireless sensing mechanism using a PCB prototype, a temperature sensor is realized on an alumina substrate and measured up to 1000°C.

### 3.1 Wireless Sensing Mechanism based on Integrated Resonator/Antenna

As introduced in chapter 1, an alternative wireless passive sensing method is to use electromagnetic propagation. In this approach, a passive sensing element, which can be in the form of a slot antenna, a dielectric resonator or a combination of them, responds to the environmental change in terms of the resonant frequency. Therefore, by sending a wide-band signal and receiving the reflection from such sensors, the resonant frequency corresponding to specific physical parameters can be measured. In [53], a slot antenna loaded with micro-electrical-mechanical-system (MEMS) varactor was used as the sensing element.

However, this approach cannot be directly applied for turbine engine applications since the slot antenna needs open space behind it, which is impossible on turbine blades. On the other hand, the resolution of this method is limited by the low Q factor of the slot antenna. This work will focus on another class of wireless passive sensors based on a seamlessly integrated resonator/antenna which not only can be used on large ground planes but also has higher resolution due to the high Q factor of the resonator.

In many wireless passive sensing applications, high-Q resonators are desirable for higher resolution and larger sensing distance. At the same time, transmit/receive antennas are needed as well. The transition between these two was commonly achieved using either coaxial or transmission line interconnections. Recently, a method of seamlessly integrating filter with slot antenna was reported in [54] with compact size and near 100% efficiency of the antenna. By extending this integration technique to a resonator/antenna, wireless passive sensors with small sizes and high efficiencies can be realized.

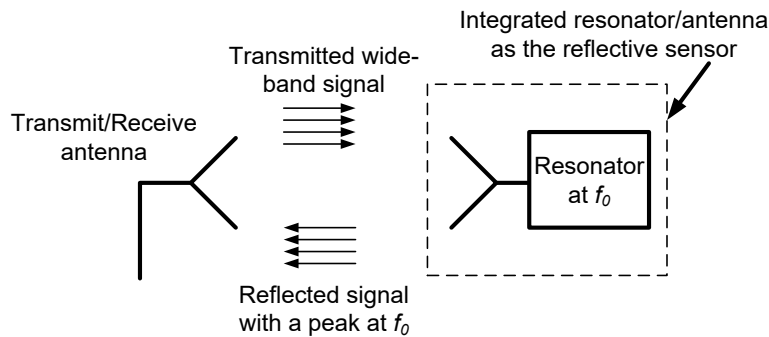


Figure 3.1: Wireless passive sensing using an integrated resonator/antenna with compact size.

A wireless passive sensing mechanism is proposed using a seamlessly integrated resonator/antenna as shown in Fig. 3.1. A wide-band signal is transmitted towards the passive sensor, and energy is coupled into the resonator through the integrated slot antenna. At the resonant frequency of the resonator, maximum transfer of energy into and out of the sensor happens. At other frequencies, the incident signal is mostly scattered. A combined frequency/time-domain processing technique is performed to wirelessly measure the resonant frequency of the resonator. Variations of physical parameters such as temperature can be



detected as a change in the resonant frequency by using proper dielectric materials with temperature-sensitive dielectric constants. The proposed compact, high-efficiency wireless sensing mechanism can enable novel wireless sensors for harsh environment applications such as turbines.

### 3.1.1 Design of Integrated Resonator/Antenna

In this section, a compact design of a cavity resonator integrated with a slot antenna is presented. The resonator/antenna is built inside a 3.18-mm-thick RT/Duroid 5880 substrate. Closely-spaced copper vias are used to form sidewalls of the resonator. Energy leakage through the sidewalls is negligible at X-band with a separation between vias of 0.2 mm. Eigenmode simulation in HFSS shows that the resonant frequency of the cavity resonator as shown in Fig. 3.2(a), but without the slot antenna and coaxial feedings, is 10.372 GHz. The unloaded Q factor ( $Q_u$ ) of this resonator due to metal and dielectric losses is found to be 822.

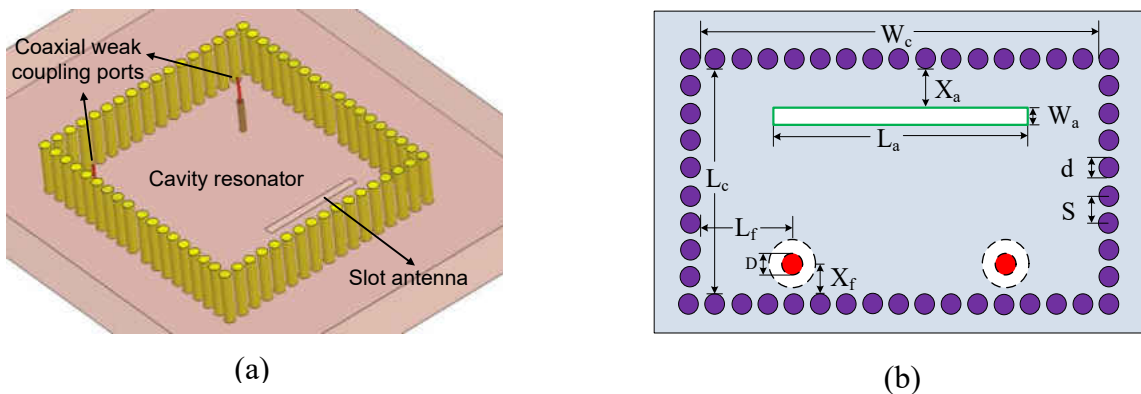


Figure 3.2: (a) An integrated resonator/antenna weakly coupled by two open-ended coaxial probes. (b) Top view of the resonator/antenna.

The slot antenna is etched on the top surface of the cavity resonator. The maximum energy coupling between the slot antenna and resonator occurs when the external Q factor ( $Q_{ext}$ ), which is due to the radiation through the slot antenna, is equal to  $Q_u$ . To find  $Q_{ext}$ , two open-ended coaxial probes are used to weakly couple to the resonator as shown in Fig. 3.2(a). The loaded Q factor ( $Q_L$ ) of the resonator due to radiation, dielectric, and metal losses can be calculated using the insertion loss method presented in [55]:

$$Q_L = \frac{f_0}{\Delta f_{3dB}} \frac{1}{1 - \text{mag}(S_{21}(\omega_0))} \quad (3.1)$$

Therefore,  $Q_{ext}$  can be obtained by

$$\frac{1}{Q_{ext}} = \frac{1}{Q_L} - \frac{1}{Q_u} \quad (3.2)$$

The desirable  $Q_{ext}$  can be realized by adjusting  $L_a$  and  $X_a$  as shown in Fig. 3.2(b). Since the coupling between the slot antenna and cavity resonator is primarily magnetic,  $Q_{ext}$  is smaller for larger  $L_a$  and smaller  $X_a$ . By performing parametric sweeps on  $L_a$  and  $X_a$ , the dimensions of the resonator/antenna can be found to achieve the desirable  $Q_{ext}$  and listed in Table. 3.1

Table 3.1: Parameter dimensions to simulate the integrated resonator/antenna in Fig. 3.2.

Parameters	$W_c$	$L_c$	$S$	$d$	$D$	$X_f$	$L_f$	$W_a$	$L_a$	$X_a$
Dimensions (mm)	13	14.4	0.87	0.635	0.174	0.635	1.0	0.9	6.0	0.3

Fig. 3.3 shows the transmission response of the resonator/antenna shown in Fig. 3.2(b). From this response,  $Q_L$  of the resonator/antenna is found to be 403 using (3.1), which implies  $Q_{ext}$  of 791, very close to  $Q_u$  of 822. The cavity resonant frequency is slightly detuned down to 10.110 GHz due to the slot antenna loading effect.

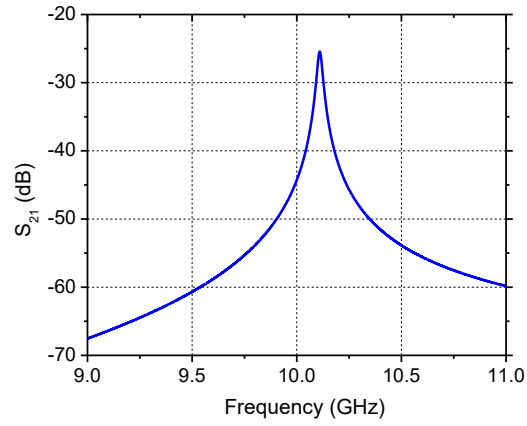


Figure 3.3: Simulated  $S_{21}$  response of the resonator/antenna with weak coaxial coupling as shown in Fig. 3.2.

To wirelessly detect the resonant frequency of the cavity resonator, an X-band open-ended waveguide (OEWG) with cross-sectional dimensions of 22.86 by 10.16 mm is used to transmit a wide-band signal to and receive reflected signals from the resonator/antenna as shown in Fig. 3.4. The gain of this OEWG is around 6 dBi within the frequency of operation.

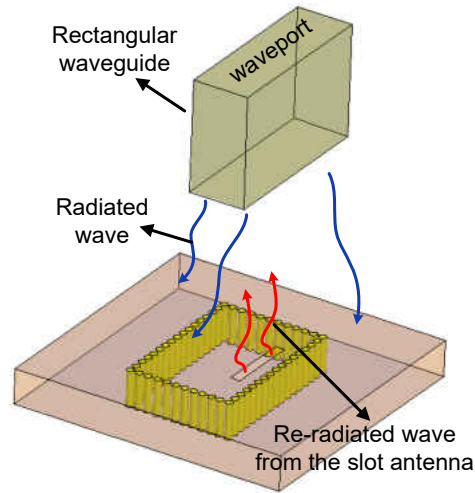


Figure 3.4: Wireless sensing of resonator/antenna using an OEWG.

Fig. 3.5 shows simulated  $S_{11}$  responses for different sensing distances between the OEWG and resonator/antenna. The waves reflected from the antenna ground plane are super-imposed upon signals radiated from the slot antenna. This makes the resonant frequency of the resonator unidentifiable in the frequency domain. Therefore, it is necessary to extract signal radiated from the cavity resonator using a time-domain (TD) gating technique.

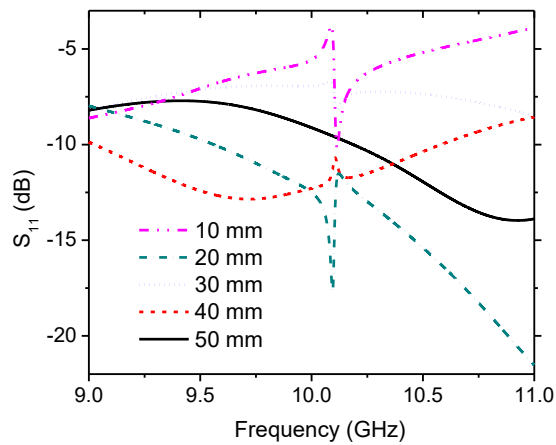


Figure 3.5: Simulated  $S_{11}$  of the OEWG for successive distances away from the resonator/antenna before TD gating.

The waves reflected back into the OEWG are attributed to two sources: one is scattered wave by the ground plane of antenna; the other is due to the energy coupled to the cavity through the slot antenna, and then re-radiated. The former can be considerable compared with the latter, which result in smeared frequency-domain responses in which the resonant frequency of the resonator is inundated in the scattered waves.

These two components of signal can be separated in time domain. Fig. 3.6 shows simulated  $S_{11}$  responses in TD for the OEWG with and without the resonator when the sensing distance is 30 mm. It is noted that in the case without the resonator, the metallic vias are removed and therefore the resonance from the resonator is eliminated.

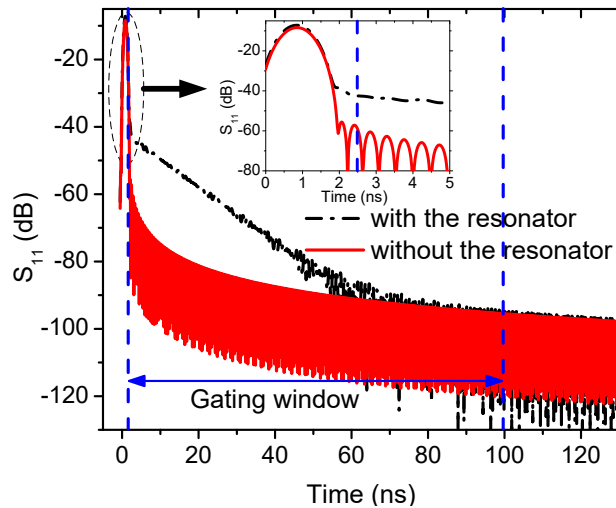


Figure 3.6: Simulated TD responses of OEWG with or without the resonator at 30 mm distance. A TD gating is performed.

The higher signal level after the main peak for the case with the resonator corresponds to the energy at the resonant frequency, which is absorbed by the cavity resonator first and then gradually re-radiated by the slot antenna. The damping of the signal intensity of the reflected wave is given by (3.3) in which  $A$  is a constant [56]:

$$E = Ae^{-\frac{\omega_0}{2Q_L}t} \quad (3.3)$$

The TD gating is performed in an Agilent Performance Network Analyzer (PNA) N5230A to selectively remove scattered waves from the ground plane of the antenna [57]. A gating window can be placed to isolate signals primarily from the resonator/antenna. The gating stop time should be equal to or larger than the time point when the two signals corresponding to cases with or without the resonator intersect. In this application, the gating stop time is chosen to be 100 ns. The gating start time is set as 2.5 ns in order to get a clear peak response in the frequency domain. Finally, TD gated signals are transformed back into frequency domain.

Similar processing procedure is carried out for each response with different sensing distances. The resonant frequency of the resonator/antenna can be clearly identified in the  $S_{11}$  responses after TD gating as shown in Fig. 3.7.

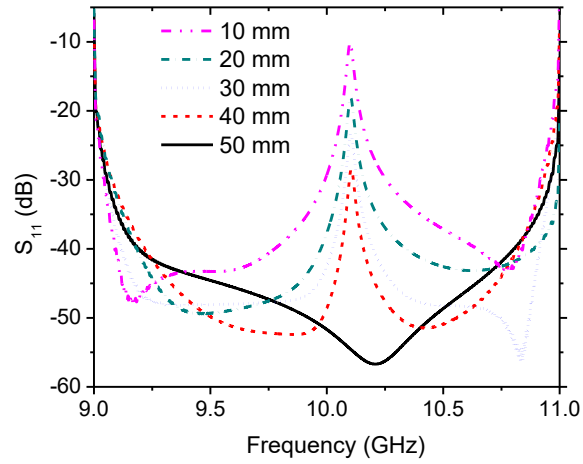


Figure 3.7: Simulated  $S_{11}$  of the OEWG for successive distances away from the resonator/antenna after TD gating.

### 3.1.2 Fabrication and Wireless Interrogation of the Integrated Resonator/Antenna

This cavity resonator/antenna is fabricated by standard PCB process. Copper vias are realized by drilling and then copper electroless plating followed by copper electroplating. Finally, the slot antenna is etched on top of the cavity resonator. Fig. 3.8(a) shows the photo of a fabricated resonator/antenna. The fabricated slot length,  $L_a$ , is 6.3 mm.

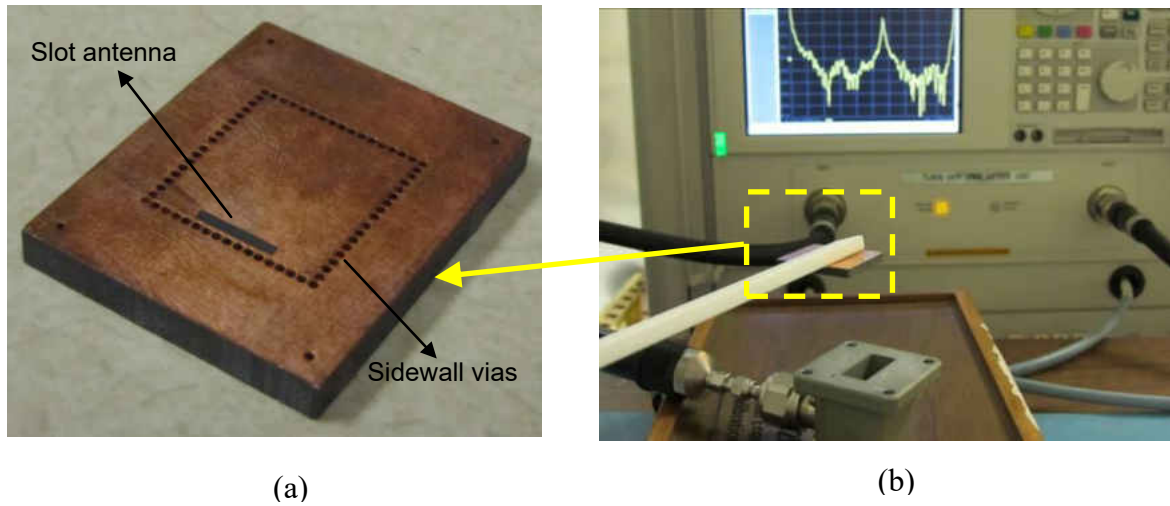


Figure 3.8: (a) Top view of the fabricated resonator/antenna, (b) Measurement setup in which the resonator is placed above the OEWG.

In the measurement, the resonator/antenna is placed above the OEWG using a plastic rod. The sensing distance between the resonator/antenna and OEWG can be manually controlled, as shown in Fig. 3.8(b). The PNA is connected to the OEWG to obtain  $S_{11}$  responses before and after the TD gating.

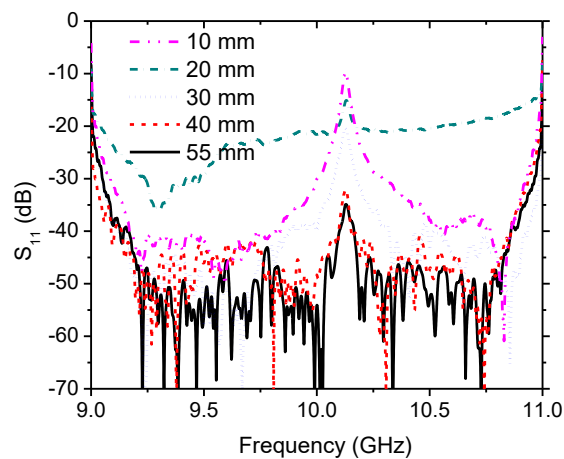


Figure 3.9: Measured  $S_{11}$  response for each sensing distance after TD gating.



The measured  $S_{11}$  after gating for different sensing distances is shown in Fig. 3.9. For distances from 10 to 55 mm, the reflected spectrum exhibits peaks within 10.127-10.131 GHz, which are very close to simulated 10.110 GHz. Using (3.3), the  $Q_L$  is derived to be 389, which is close to simulated 403. When the distance between the OEWG and resonator/antenna increases, the level of the received signal decreases due to the enlarged free space loss.

### 3.2 Temperature Sensors using Resonator/Antenna Integration

After the demonstration of the integrated resonator/antenna for wireless sensing in the section 3.1, a temperature sensor for high-temperature applications is realized and shown in Fig. 3.10. A slot antenna is seamlessly integrated with a rectangular microwave cavity resonator. This sensor is formed by coating an alumina substrate with platinum to realize a cavity resonator. The resonant frequency of this resonator sensor decreases versus temperature, which is primarily determined by the temperature-dependent material properties of alumina. This resonant frequency can be wireless sensed by an OEWG antenna through the integrated slot antenna. The seamless integration of slot antenna and resonator, demonstrated in [58] at room temperature, is able to provide efficient energy coupling between the sensor and free space without the need of additional volume for the antenna. This technique was also used to realize integrated filter/antennas with compact size and high efficiency [59]-[62].

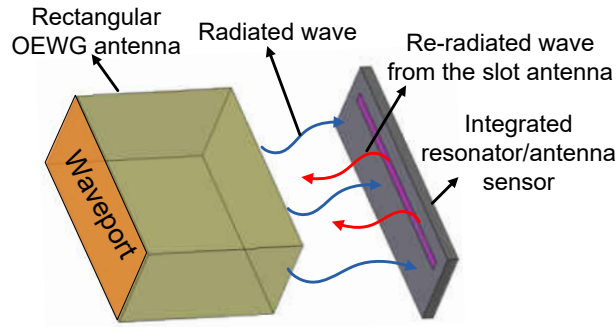


Figure 3.10: Wireless sensing of integrated resonator/antenna sensor.

The sensing mechanism shown in Fig. 3.10 is suitable for harsh environment applications due to the use of robust sensing materials and wireless passive sensing technique, which inherently functions over a ground plane. In practice, the interrogation antenna will be placed outside the high-temperature zone as described in [63]. A C-band prototype of the proposed sensor is fabricated and wirelessly evaluated in the laboratory environment. The concept can be readily scaled to other frequency bands based on the frequency characteristics of the engine [64].

### 3.2.1 Design and Simulation of the Temperature Sensor

Our previous work in [58] shows that the maximum energy coupling to and from the resonator through the slot antenna occurs when the unloaded Q factor  $Q_u$  of the resonator is equal to the radiation Q factor  $Q_{rad}$  of the slot antenna. Following the procedure described in [59],  $Q_{rad}$  can be extracted from the structure shown in Fig. 3.11(a) and its equivalent circuit in Fig. 3.11(b).  $Q_{rad}$  is equal to the external Q factor  $Q_{ext}$  in Fig. 3.11(b) assuming the metal and dielectric in Fig. 3.11(a) to be lossless in HFSS simulations.  $Q_{ext}$  can be calculated using:

$$Q_{ext} = \frac{\omega_0}{2 \operatorname{Re}(Z_{in}(\omega_0))} \frac{d(\operatorname{Im}(Z_{in}))}{d\omega} \Big|_{\omega=\omega_0} \quad (3.4)$$

where  $Z_{in}$  is the input impedance of the structure at the reference plane shown in Fig. 3.11(a).

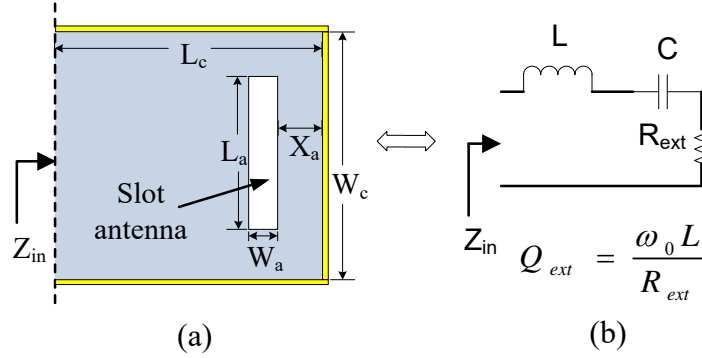


Figure 3.11: (a) Schematic and (b) equivalent circuit of an open-ended cavity resonator/slot antenna.  $W_a = 0.45$  mm,  $W_c = 22.86$  mm, thickness = 1.016 mm.

The design curve for  $Q_{ext}$  is given in Fig. 3.12 for different combinations of antenna length  $L_a$  and position  $X_a$ . When the antenna gets further away from the edge of the cavity or becomes longer,  $Q_{ext}$  decreases. At the room temperature,  $Q_u$  is found to be 208 in HFSS simulations by setting the corresponding metal and dielectric loss properties. Using Fig. 3.12,  $L_a$  and  $X_a$  are selected to be 20 and 0.8 mm, respectively, to match  $Q_u$  for maximum energy coupling.

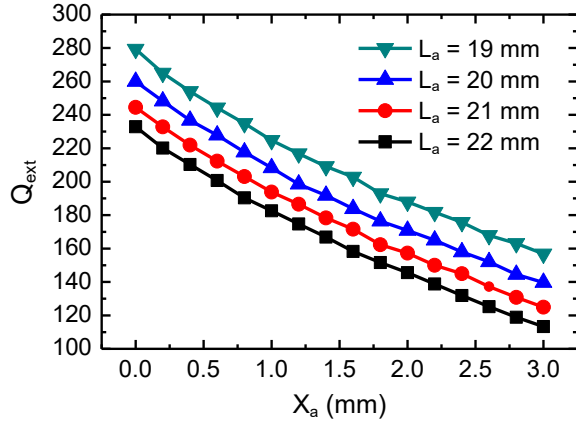


Figure 3.12: Simulated  $Q_{ext}$  for different slot antenna positions  $X_a$  and lengths  $L_a$ . The resonant frequency is fixed at 5.2 GHz.

For these specific values of  $L_a$  and  $X_a$ , effect of slot width  $W_a$  on  $Q_{ext}$  is demonstrated in Fig. 3.13.

It is observed that the  $Q_{ext}$  is reduced for increasing  $W_a$ , but the variation is not significant.

Eventually  $W_a = 0.45$  mm is selected.  $L_c$  in Fig. 3.11(a) is always adjusted to ensure  $f_0 = 5.2$  GHz

and finally found to be 5.93 mm for the selected  $L_a$  and  $X_a$ . To wirelessly detect the resonant

frequency of the sensor, a standard OEWG (3.95-5.85 GHz) is used as the interrogation antenna,

which exhibits a gain around 6 dBi within 4.74-5.12 GHz.

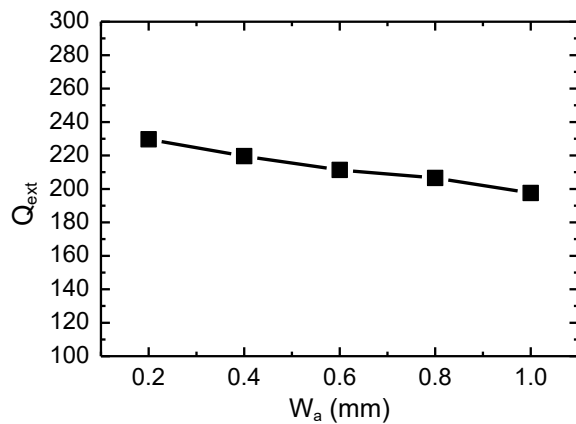


Figure 3.13: Simulated  $Q_{ext}$  for different slot width  $W_a$  for  $L_a = 20$  mm and  $X_a = 0.8$  mm.

### 3.2.2 Time-Domain Gating for the Wireless Interrogation

Fig. 3.14 shows simulated  $S_{11}$  responses for successive sensing distances between the OEWG and sensor. The resonant behavior of the sensor is difficult to distinguish due to superposition of reflections from the OEWG, and the re-radiated waves from the resonator as presented in Fig. 3.15 (a). Therefore, it is necessary to apply time-domain (TD) gating to isolate the response from the sensor itself.

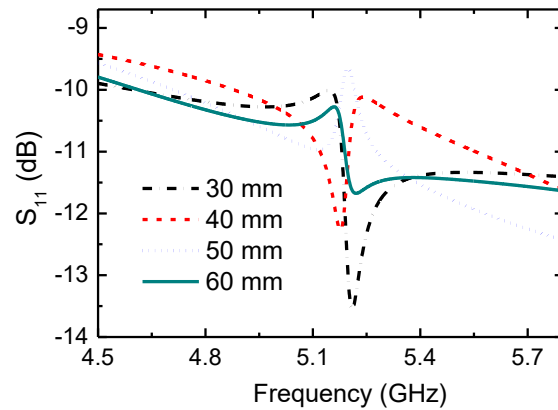


Figure 3.14: Simulated  $S_{11}$  of the OEWG for successive distances away from the sensor *before* TD gating.

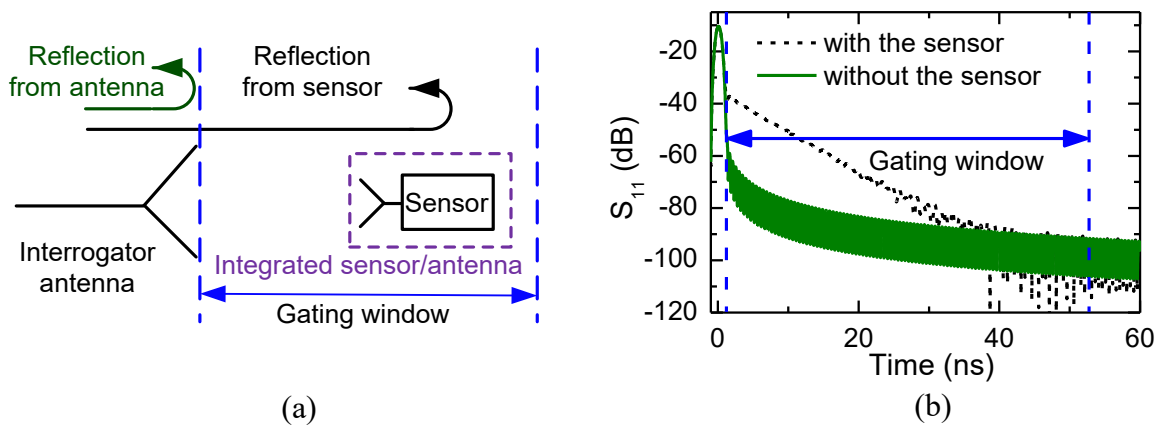


Figure 3.15: (a) Schematic of the proposed TD gating process; (b) simulated TD responses of OEWG with and without the sensor.

The  $S_{11}$  responses of the OEWG with and without the sensor are compared in time domain in Fig. 3.15(b) for a sensing distance of 30 mm. The main peak right after 0 ns is due to the reflection at the open aperture of the OEWG. For the case without the sensor,  $S_{11}$  quickly drops to the noise floor. When the sensor is present, it absorbs the incident wave from the OEWG and then re-radiates back to the OEWG in a periodically decaying manner. It is implied in (3.3) that the field damping is slower for higher  $Q_L$ , which leads to a longer sensing range. A TD gating window should be defined to isolate the response from the sensor. For a sensing distance of 30 mm, the *gating start time* is set to be 1.7 ns. The *gating stop time* is set to be 55 ns where the two curves in Fig. 3.15(b) intersect each other. Similar gating procedures are carried out for sensing distances of 30, 40, 50 and 60 mm. Finally, TD-gated signals are transformed back into frequency domain and shown in Fig. 3.16. The resonant frequency of the sensor can be clearly identified and is independent of the sensing distance.

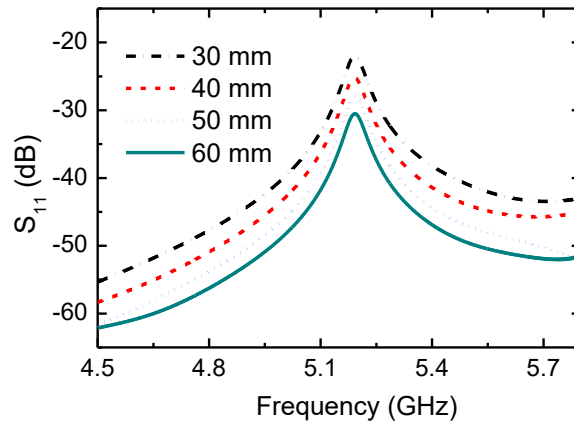


Figure 3.16: Simulated  $S_{11}$  of the OEWG for successive distances away from the sensor *after* TD gating.

As the temperature increases, the dielectric constant of alumina monotonically increases as indicated from previous research [30]. It is known that the resonant frequency of a cavity resonator is dependent on the dielectric properties of the constituting material. Therefore, as the temperature changes, the resonant frequency of the resonator also varies. This resonant frequency and temperature relationship is the basis of the sensing mechanism for the wireless passive sensors presented herein. To illustrate this phenomenon, the dielectric constant of alumina is swept from 9.6 to 10.5 in HFSS simulations. The  $S_{11}$  at the OEWG corresponding to different dielectric constants shown in Fig. 3.17 clearly indicates a resonant frequency downshift. Since the resonant frequency change against temperature is monotonic, the dielectric constant of alumina can be extracted from the measured  $S_{11}$  by knowing the temperature.

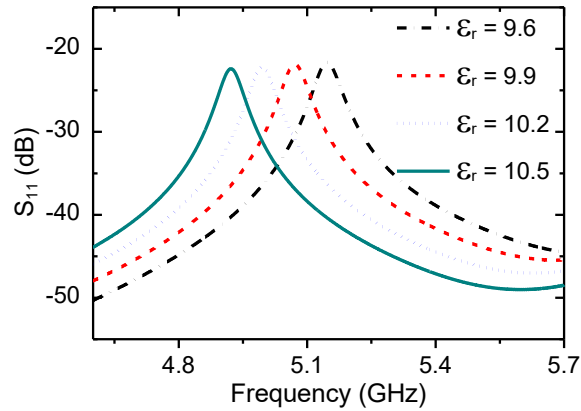


Figure 3.17: Simulated  $S_{11}$  of the OEWG: sensor resonant frequency changes with the dielectric constant of the alumina substrate.

### 3.2.3 Fabrication and Measurement of the Temperature Sensor

An alumina substrate (ADS-96R) is cut into  $22.86 \times 5.93 \times 1.016 \text{ mm}^3$  using MTI Precision CNC Dicing/Cutting Saw (SYJ-400). A layer of platinum paste (ESL 5542) is applied on all the faces of the substrate to form a waveguide cavity resonator. Then the substrate covered by platinum paste is dried at  $110^\circ\text{C}$  for 10 minutes and sintered at  $980^\circ\text{C}$  for 10 minutes. The ramp rate during the sintering is  $10^\circ\text{C}/\text{min}$ . The formed platinum layer is approximately  $12 \text{ }\mu\text{m}$  thick, which corresponds to 5.2 and 2.6 skin depths at 25 and  $1000^\circ\text{C}$ , respectively. The slot antenna with dimensions of  $20 \times 0.45 \text{ mm}^2$  is formed on the top surface of the cavity by milling process. The fabricated sensor is presented in Fig. 3.18.

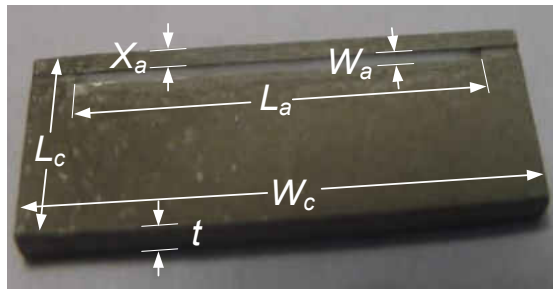


Figure 3.18: The fabricated temperature sensor.  $W_a = 0.45 \text{ mm}$ ,  $L_a = 20 \text{ mm}$ ,  $X_a = 0.8 \text{ mm}$ ,  $W_c = 22.86 \text{ mm}$ ,  $L_c = 5.93 \text{ mm}$ ,  $t = 1.016 \text{ mm}$ .

A 2-inch-diameter heat pad (Micropyretics Heaters International Inc.) is used to control the temperature of the sensor from  $50$  to  $1000^\circ\text{C}$  as shown in Fig. 3.19(a). A piece of alumina board is placed over the heat pad to prevent air convection and stabilize the temperature of the sensor as shown in Fig. 3.19(b). A *K*-type thermocouple (Omega HH11) is used to read the temperature and provide the feedback to the temperature controller.



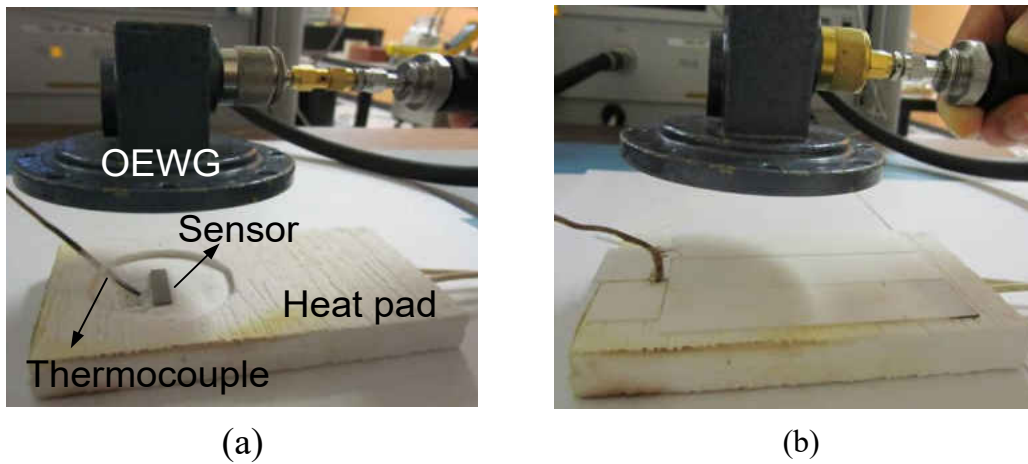


Figure 3.19: (a) Elevated OEWG for demonstration purpose. (b) The sensor is placed inside the heat pad with alumina board cover.

The *G*-band OEWG is used for the wireless sensing. One port Short-Open-Load (SOL) calibration is performed at the end of the coaxial cable and proper TD gating is applied using an Agilent 40-GHz PNA-L (N5230A). Thus, the real-time resonant frequency of the sensor can be measured wirelessly for different temperatures. It is observed that the temperature of the coaxial cable remains below 50°C even when the heat pad is heated up to 1000°C.

The measured  $S_{11}$  responses of the OEWG for several temperature values are presented in Fig. 3.20. Each curve corresponds to a single temperature in the 50-1000°C range. It is observed that at each temperature, there exists a unique peak with the highest signal level. This peak corresponds to the resonant frequency of the integrated cavity/resonator. The interrogating unit will be able to identify this peak by comparing the received signal levels through the frequency domain.

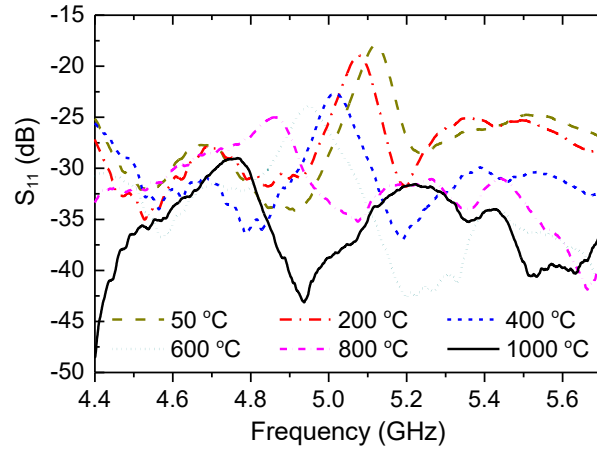


Figure 3.20: Measured  $S_{11}$  responses of the OEWG for different temperatures.

The resonant frequencies of the sensor for temperatures from 50 to 1000°C are derived by the curve peak of each plot in Fig. 3.20 and plotted in Fig. 3.21. The resonant frequency decreases from 5.12 to 4.74 GHz in this temperature range, which corresponds to a measured sensor sensitivity of 0.40 MHz/°C. Using full-wave simulation results from Fig. 3.17, the dielectric constant of alumina can be extracted for each measured resonant frequency and found to increase from 9.7 to 11.2 as shown in Fig. 3.21.

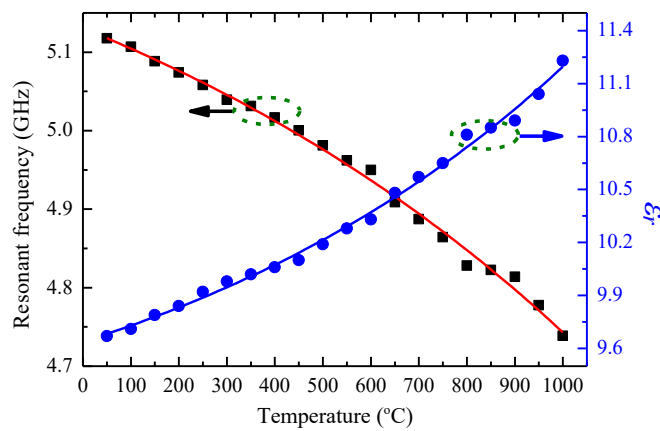


Figure 3.21: Measured resonant frequency of the sensor and extracted dielectric constant of alumina versus temperature.

Considering the thermal expansion coefficient (CTE) of  $8.2 \times 10^{-6}/^{\circ}\text{C}$  for alumina, the maximum dimensional change of the substrate is 0.8% from 50 to  $1000^{\circ}\text{C}$ , which is much less than the 8% resonant frequency change in this temperature range. Therefore, the dielectric constant change is the primary contributing factor to the resonant frequency variations. The distance between the OEWG and sensor for the data in Fig. 3.21 is 30 mm to ensure clear signal shape up to  $1000^{\circ}\text{C}$ .

The existing design is optimized for maximum energy coupling at the room temperature. As the temperature increases,  $Q_u$  is reduced almost linearly as shown in Fig. 3.22 due to the increased loss of both alumina and platinum. However,  $Q_{ext}$  is constant for all temperatures since it is only geometry-dependent. As a result, the mismatch becomes larger at higher temperatures. The sensing distance can be increased by designing the maximum energy coupling at  $1000^{\circ}\text{C}$ . In addition, the sensing distance can be improved by increasing the output power from the transmitter.

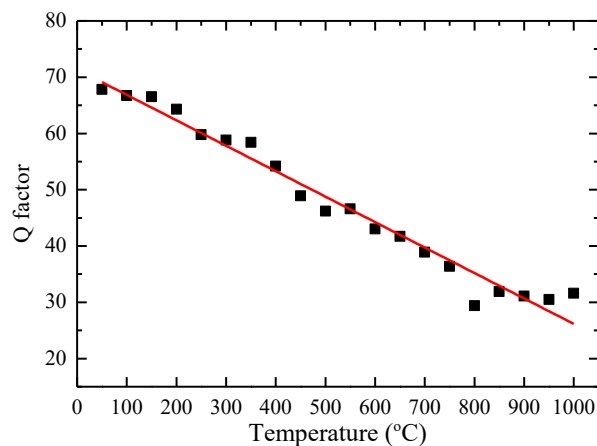


Figure 3.22: Measured Q factor of the sensor versus temperature.

The measured resonant frequency is repeatable and the sensor is intact after many heat cycles within 50-1000°C. In addition, other novel temperature-dependent and stable materials are under development at UCF which can withstand temperatures up to 1600°C. Those materials will replace alumina for final engineering version of the proposed sensing mechanism.

### 3.3 Conclusion

A wireless passive sensing mechanism is demonstrated first using a cavity resonator seamlessly integrated with a slot antenna. An interrogating signal is transmitted towards a resonator/antenna. The signal is modulated and reflected back with maximum reflection at the resonant frequency of the resonator. Being compact and efficient, the proposed passive sensing mechanism can be used to measure the resonant frequency of a passive resonator in a wireless manner.

Based on the demonstrated wireless sensing mechanism, a novel low-profile wireless passive temperature sensor prototype is realized up to 1000°C for harsh-environment applications. The integrated resonator/antenna approach is able to provide an antenna for the sensor with no additional volume and high coupling efficiency. This presented technique is scalable in terms of frequency or size depending on the requirements. Using the wireless passive sensing approach, temperatures on the most critical part of the gas turbines, i.e. rotating turbine blades, can also be monitored.

## CHAPTER 4      A TEMPERATURE SENSOR BASED ON A REFLECTIVE PATCH

In this chapter, a novel temperature sensor is proposed by using a rectangular reflective patch. This patch sensor simultaneously works as both a radiation element and a resonator sensor, which results in a compact volume and a planar structure. The patch sensor design is discussed, followed with sensor fabrication. For demonstration, this temperature sensor is measured up to 1100°C.

### 4.1 Introduction of Reflective Patch Sensors

The schematic of the reflective patch sensor is shown in Fig. 4.1. The resonant frequency of this patch sensor decreases with temperature, which is primarily determined by the temperature-dependent permittivity of the alumina substrate. For a wide-band interrogation signal, a maximum power reflection is expected at the resonant frequency of the reflective patch. This resonant frequency  $f_r$  can be wirelessly interrogated by an open-ended waveguide (OEWG) antenna.

Using robust material and wireless passive sensing configuration, the proposed temperature sensor shown in Fig. 4.1 is able to survive the harsh-environment conditions. The rectangular patch has inherent advantages of easy design and fabrication due to the planar structure. The low-profile patch sensor has a ground plane for shielding underneath the substrate. Thus, it could be mounted onto turbine blades.

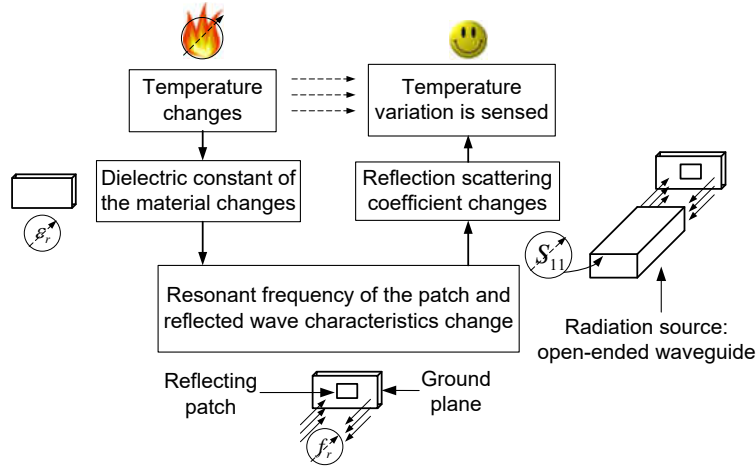


Figure 4.1: Flow chart of the proposed wireless passive temperature sensing mechanism.

## 4.2 Principle and Design of the Reflective Patch Sensor

In this section, the working principle of the reflective patch sensor is analyzed using HFSS simulation. After that, the antenna parameters, including thickness  $h$ , length  $L$  and width  $W$  are designed for sensor applications, respectively.

### 4.2.1 *Principle of the Reflective Patch Working as a Temperature Sensor*

For a rectangular patch operating at  $TM_{010}$  mode, the resonant frequency is:

$$f_r = \frac{c}{2L_{eff} \sqrt{\epsilon_r}} \quad (4.1)$$

in which  $L_{eff}$  is the effective patch length,  $\epsilon_r$  is relative permittivity of the patch substrate, and  $c$  is the speed of light in vacuum. With a rising temperature, the dielectric constant of the alumina

substrate increases [30], and therefore the resonant frequency  $f_r$  is reduced monotonically. By wirelessly reading  $f_r$  of the reflective patch, the environmental temperature can be detected, which is the working principle of the reflective patch as a temperature sensor.

The reflective patch antenna has the maximal power reflection at its resonant frequency, and thus  $f_r$  can be identified through the resonance peak. To demonstrate the concept of the reflective patch sensor, 3-D views of the rectangular patch in HFSS simulation are shown in Fig. 4.2. The patch length, width and substrate thickness are set to  $L = 9.3$  mm,  $W = 8$  mm, and  $h = 0.0635$  mm, respectively. The patch and ground metal are both platinum, and the dielectric constant of the alumina is set to  $\epsilon_r = 9.7$ . A  $G$ -band open-ended waveguide (WR-187) antenna is used to transmit a wide-band (3.95-5.85 GHz) signal to interrogate the reflective patch sensor. Working as a resonator, the reflective patch is excited after receiving the incident wave, and then re-radiates the power back to the waveguide antenna.

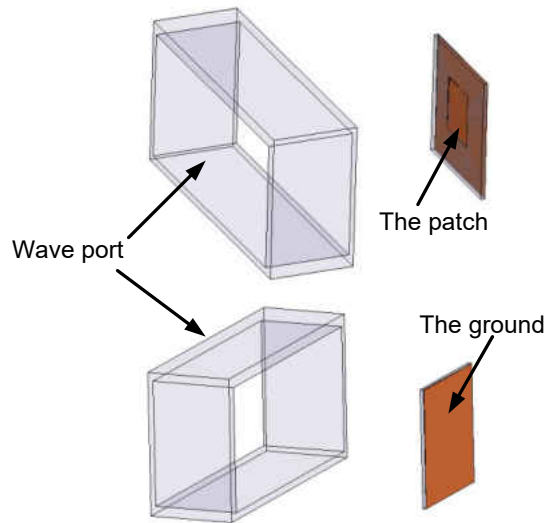


Figure 4.2: 3-D views of the sensor structure in HFSS. An OEWG is used as the interrogation antenna to detect the reflective patch sensor.

Electric field distributions inside the alumina substrate are illustrated in Fig. 4.3 at three different frequencies. It is observed that the electric fields are maximal at the two radiation edges for all the three frequencies, which means the reflective patch resembles a radiating patch antenna. In addition, the electric field is stronger at the patch resonant frequency  $f_r = 5.05$  GHz than the other two frequencies, which exhibits the characteristic of a microwave cavity resonator.

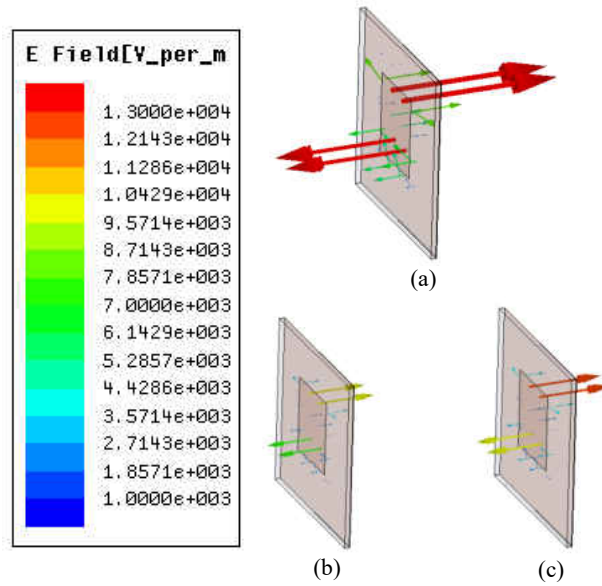


Figure 4.3: Electric field distributions inside the dielectric substrate at (a) resonant frequency  $f_r = 5.05$  GHz (b) lower frequency  $f_l = 5.00$  GHz (c) higher frequency  $f_h = 5.10$  GHz.

According to the radiation mechanism of a patch antenna, the equivalent magnetic current densities at the radiation slots are [65]:

$$M_s = -2\hat{n} \times E_a \quad (4.2)$$



From Fig. 4.3, it can be observed that the equivalent magnetic dipoles radiate more power at the resonant frequency  $f_r$ , due to the fact that the electric fields at the two radiation edges are stronger at  $f_r$  than other frequencies.

The wave intensity radiated from the sensor is modulated by the reflective patch, and this modulation is determined by the temperature-dependent substrate. During the wireless interrogation the interrogation antenna, i.e. OEWG antenna in this work, is used to transmit a wideband microwave signal for sensor excitation. The patch sensor receives the microwave power that is uniform in frequency domain, and then re-radiates the modulated microwave power. Finally, the resonant frequency of the reflective patch sensor can be identified by reading the resonance peak.

#### *4.2.2 Optimized Design of Thickness, Length and Width of the Patch Sensor*

The sensor performance of the reflective patch is dependent on several parameters such as the substrate thickness  $h$ , patch length  $L$  and patch width  $W$ . The effects of these patch parameters are investigated and discussed below.

##### *4.2.2.1 Design of the Substrate Thickness $h$*

The effect of  $h$  on total Q-factor ( $Q_T$ ) of the reflective patch is investigated first.  $Q_T$  is an essential parameter for the sensor application, since the higher  $Q_T$  leads to higher sensor resolution and longer wireless sensing distance. In order to study the effects of the patch parameters on  $Q_T$ , a weak coupling coaxial port is fed to extract the  $Q_T$  by using HFSS simulation as presented in Fig. 4.4.

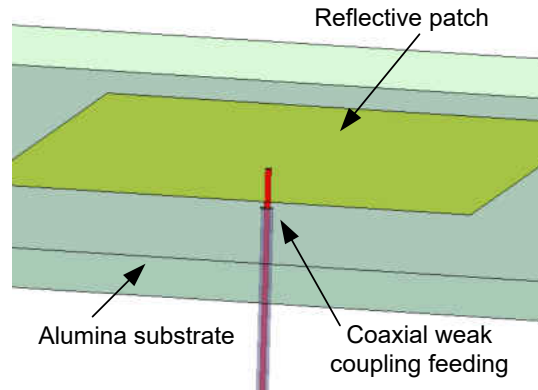


Figure 4.4: Coaxial weak coupling to simulate the  $Q_T$  of the reflective patch in HFSS.

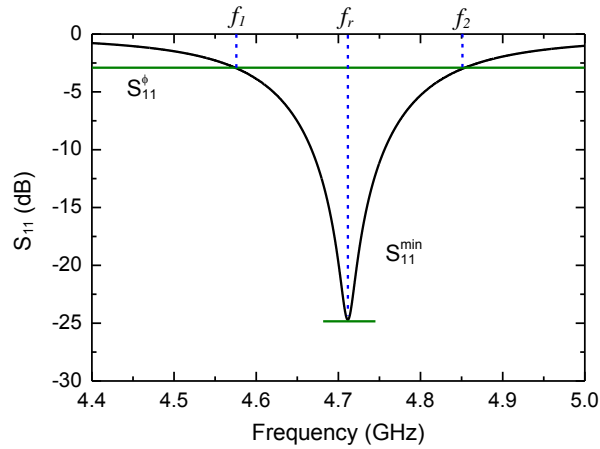


Figure 4.5:  $S_{11}$  response by using the coaxial weak coupling probe.

Fig. 4.5 shows a simulated  $S_{11}$  response of the feeding probe as shown in Fig. 4.4, in which the substrate thickness is set as  $h = 0.0635$  mm. By using the  $S_{11}$  response, the  $Q_T$  can be calculated by [51]:

$$Q_T = \frac{f_r}{f_2 - f_1} (1 + k) \quad (4.3)$$

in which,  $k$  is:

$$k = \begin{cases} \frac{1 - 10^{-S_{11}^{\min}/20}}{1 + 10^{-S_{11}^{\min}/20}} & \text{undercoupled} \\ \frac{1 + 10^{-S_{11}^{\min}/20}}{1 - 10^{-S_{11}^{\min}/20}} & \text{overcoupled} \end{cases} \quad (4.4)$$

and the  $S_{11}^{\phi}$  in Fig. 4.5 can be calculated by:

$$S_{11}^{\phi} = 10 \log \frac{1 + 10^{-S_{11}^{\min}/10}}{2} \quad (4.5)$$

The effect of the substrate thickness  $h$  is studied by this weak coupling method, and the result is shown in Fig. 4.6. In the HFSS simulations,  $h$  is varied, while both the patch length and width are both set to 9.3 mm.

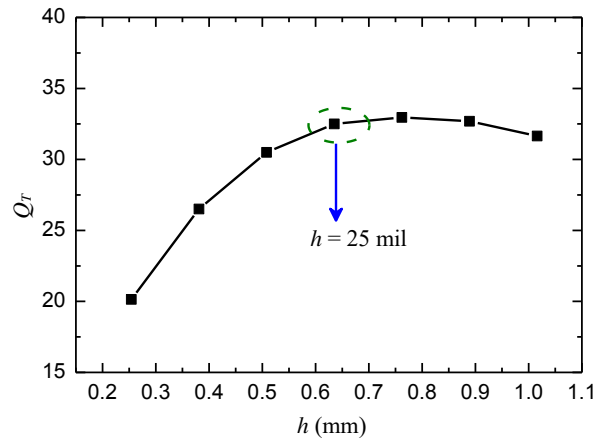


Figure 4.6: Design of the alumina substrate thickness. In the simulation,  $L = W = 9.3$  mm.

The simulated  $Q_T$  in Fig. 4.6 is relatively low due to the large metallic and dielectric losses. It can be observed that the  $Q_T$  increases with the substrate thickness because of the higher conduction Q-factor ( $Q_c$ ) given by:

$$Q_c = h\sqrt{\pi f_r \mu_0 \sigma} \quad (4.6)$$

Then  $Q_T$  decreases with  $h$  due to the growing dissipated power carried by surface wave [66]. Finally, considering the commercially available substrate thickness,  $h = 0.0635$  mm is chosen to achieve a high  $Q_T$ . According to our previous experiment result [67], the conductivity of the porous platinum is about  $\sigma = 5 \times 10^5$  S/m, and the dielectric loss of alumina substrate is  $\tan \delta = 0.012$  at  $1000^\circ\text{C}$ . In addition, the effect from the patch width  $W$  on the  $Q_T$  will be discussed in next section.

#### 4.2.2.2 Design of the Patch Length $L$

Then the patch length  $L$  is designed after the study of the substrate thickness  $h$ . The patch length  $L$  can be calculated by the resonant frequency  $f_r$  and the effective dielectric constant of the patch substrate [65]:

$$L = \frac{c}{2f_r \sqrt{\epsilon_{eff}}} \quad (4.7)$$

The  $f_r$  of the patch sensor is designed to be approximately 4.7 GHz at high temperatures. Additionally, based on our previous experiment result [67], the dielectric constant of the alumina substrate is  $\epsilon_r = 11.2$  at  $1000^\circ\text{C}$ . Therefore, the patch length is calculated as  $L = 9.3$  mm.

#### 4.2.2.3 Design of Patch Width $W$

After that the patch width  $W$  is designed, according to its effects on the  $Q_T$  and external Q factor ( $Q_{ext}$ ). For a patch antenna, the  $Q_T$  is expressed as:

$$\frac{1}{Q_T} = \frac{1}{Q_r} + \frac{1}{Q_{sur}} + \frac{1}{Q_c} + \frac{1}{Q_d} \quad (4.8)$$

And the  $Q_{ext}$  corresponds to the total effect of both the radiation Q ( $Q_r$ ) and surface wave Q ( $Q_{sur}$ ) factors:

$$\frac{1}{Q_{ext}} = \frac{1}{Q_r} + \frac{1}{Q_{sur}} \quad (4.9)$$

By setting the metallic and dielectric losses to zero in HFSS, the  $Q_{ext}$  can be extracted from the response of the weak coupling probe in Fig. 4.4.

The effects of  $W$  on  $Q_T$  and  $Q_{ext}$  are simulated and shown in Fig. 4.7. It is observed in Fig. 4.7 that the  $Q_T$  is almost constant as  $W$  is varied. In addition,  $Q_{ext}$  decreases as the patch width  $W$  is increased, which results in higher antenna efficiency. With higher antenna efficiency and larger antenna dimension, more power is radiated towards the interrogation antenna, which is desirable for wireless sensing.

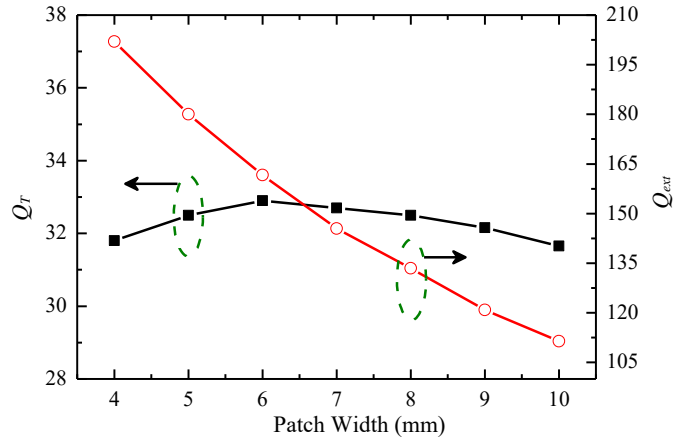


Figure 4.7: Reflective patch width design. The patch length and thickness are  $L = 9.3$  mm and  $h = 0.0635$  mm, respectively.

For a compact patch dimension, this reflective patch sensor is designed with operating mode of  $TM_{010}$ . Therefore, the patch width  $W$  is chosen to be smaller than the patch length  $L$ . Finally,  $W = 8$  mm is designed as the reflective patch width, as a trade-off between the antenna efficiency and patch dimension.

A space larger than quarter wave length is designed between the two edges of the patch and ground. Finally, the alumina substrate size is chosen to be 21 mm  $\times$  21 mm.

### 4.3 Wireless Interrogation of the Reflective Patch Sensor

In this section, wireless interrogation of the reflective patch sensor is discussed. Fig. 4.8(a) shows simulated  $S_{11}$  responses for successive sensing distances between the OEWG and the reflective patch. The resonant frequency is difficult to distinguish due to superposition of reflections from the OEWG antenna, and the re-radiated waves from the reflective patch. Therefore, it is necessary to apply time-domain (TD) gating to isolate the response from the

patch sensor itself. The  $S_{11}$  responses of the OEWG with and without the patch sensor are compared in time domain in Fig. 4.8(b), for a sensing distance of 30 mm. The main peak right after 0 ns is due to the reflection at the open aperture of the OEWG. For the case without the patch,  $S_{11}$  quickly drops to the noise floor. When the reflective patch is present, it absorbs the incident wave from the OEWG first and then re-radiates back to the OEWG in a periodically decaying manner.

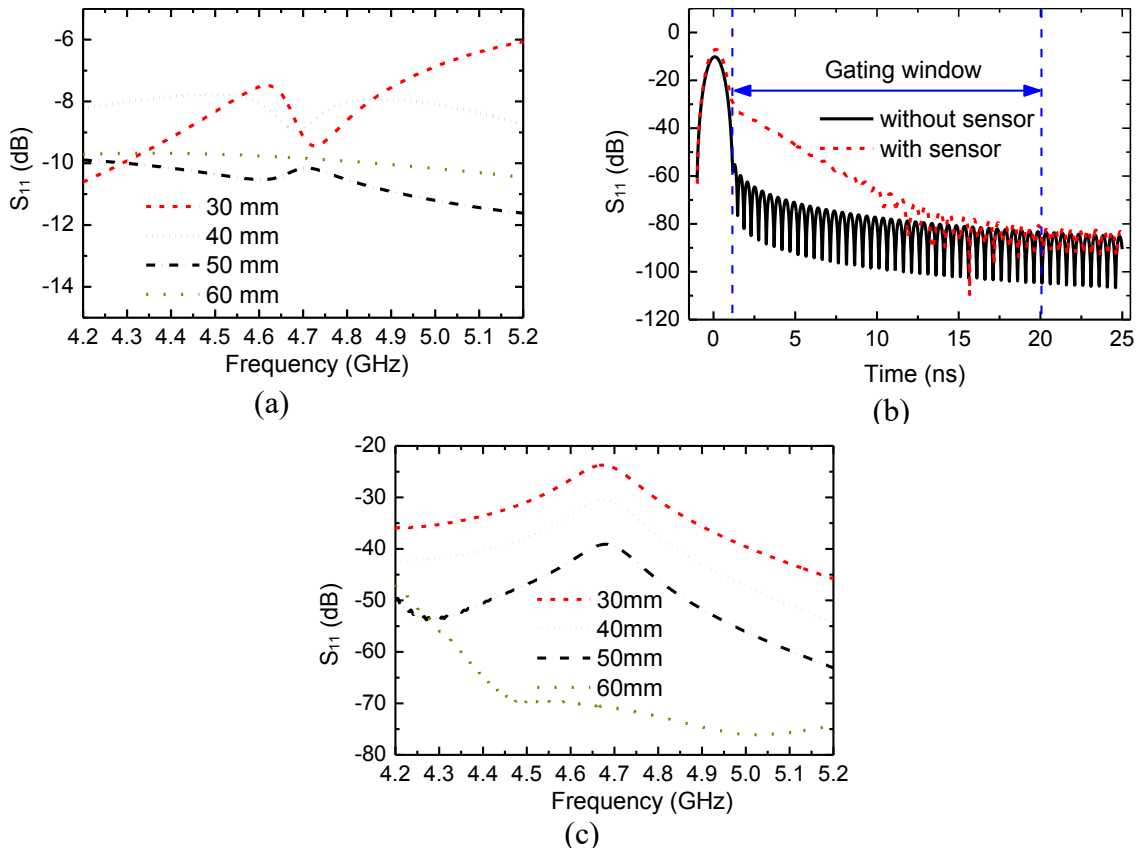


Figure 4.8: TD gating process: (a) Simulated  $S_{11}$  of the OEWG antenna. (b) Compare of  $S_{11}$  responses of the OEWG antenna along and the OEWG antenna with the reflective patch. (c) Responses for different sensing distances after the TD gating.

A TD gating window should be defined to isolate the response from the reflective patch. The gating start time is set to be 1.3 ns and the gating stop time is set to be 20 ns where the two curves intersect each other in Fig. 4.8(b). Similar gating procedures are carried out for sensing distances of 30, 40, 50 and 60 mm, respectively. Finally, TD-gated signals are transformed back into frequency domain and shown in Fig. 4.8(c). The resonant frequency of the sensor can be clearly identified and is independent of the sensing distance.

The resonant frequency  $f_r$  is only determined by the dielectric constant of the sensor substrate, since the patch dimension is fixed. To illustrate this phenomenon, the dielectric constant of alumina is swept from 9.6 to 11.6 in HFSS simulations. The  $S_{11}$  of the OEWG corresponding to different dielectric constants shown in Fig. 4.9 clearly indicates a resonant frequency downshift.

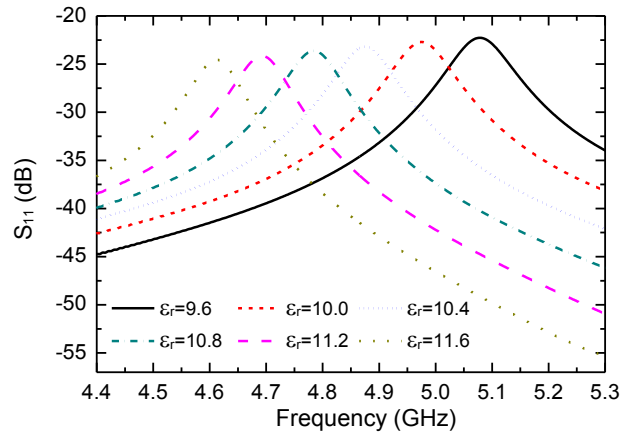


Figure 4.9: Simulated  $S_{11}$  at the input port of the OEWG for various dielectric constants of the alumina substrate.

The sensor resonant frequency  $f_r$  for different dielectric constant is also extracted by picking the resonance peaks in Fig. 4.9 and plotted in Fig. 4.10. The resonant frequency changes with the



dielectric constant in a monotonic manner, and is almost linear. Therefore, the dielectric constant of alumina substrate can be extracted from the measured  $S_{11}$  peak at a particular temperature.

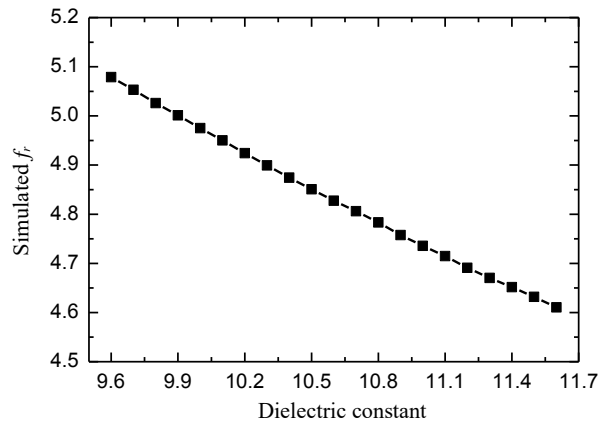


Figure 4.10: Simulated resonant frequency of the patch sensor for various dielectric constants of the alumina substrate.

This proposed patch sensor is also not sensitive to environmental influence because of the shielding effect of the ground plane beneath the patch substrate. This surrounding effect is verified by mounting the patch sensor on a metallic ground with sizes of  $\lambda_0 \times \lambda_0$  at 4.7 GHz in HFSS simulation. Fig. 4.11 shows that the resonant frequency is not influenced by the surrounding environment. This is important because of the complicated metal structures in a turbine engine.

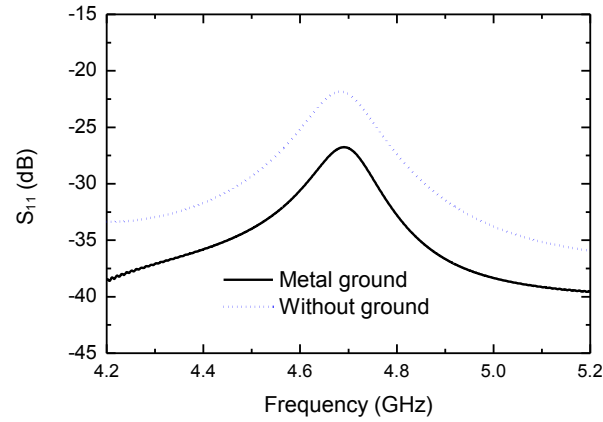


Figure 4.11: Ground effect on the response of reflective patch after TD gating.

#### 4.4 Fabrication and Measurement of the Patch Temperature Sensor

The patch sensor is fabricated on the alumina substrate with patterned platinum as the metal layer. An alumina ceramic substrate (ADS-96R) is cut into  $21 \times 21 \times 0.635 \text{ mm}^3$  by using MTI Precision CNC Dicing/Cutting Saw (SYJ-400). A layer of platinum paste (ESL 5542) is applied and patterned on both the top and bottom surfaces of the substrate to form the rectangular patch and the ground plane, respectively. Then the alumina substrate with platinum paste is dried at  $110^\circ\text{C}$  for 10 minutes and sintered at  $980^\circ\text{C}$  for 10 minutes to form a platinum film. The ramp rate during the sintering is  $10^\circ\text{C}/\text{min}$  for both the rising and declining temperature. The platinum paste is applied six times, and the formed porous platinum layer is approximately  $25 \text{ }\mu\text{m}$  thick. The photo of fabricated patch sensor is presented in Fig. 4.12.

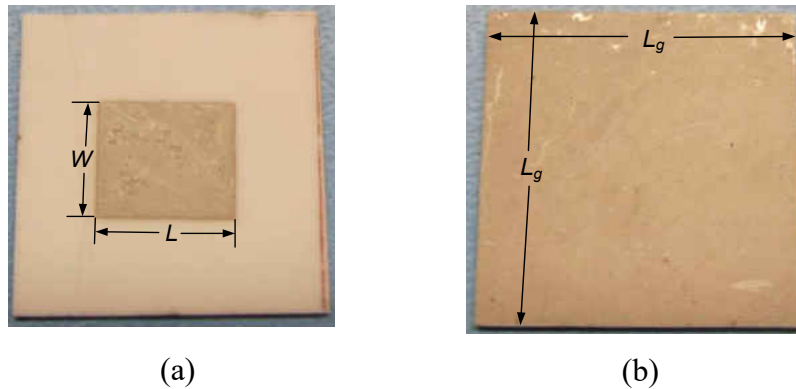


Figure 4.12: Top (a) and bottom (b) view of the fabricated reflective patch sensor.  $W = 8$  mm,  $L = 9.3$  mm,  $L_g = 21$  mm. The thickness of alumina substrate is  $h = 0.635$  mm.

The test temperature is controlled by a 2-inch-diameter heat pad (Micropyretics Heaters International Inc.) from 50 to 1100°C as shown in Fig. 4.13(a) and the patch sensor is placed inside the heat pad. A  $K$ -type thermocouple (Omega HH11) is used to read the temperature and provide the feedback to the temperature controller. Air convection is prevented by a piece of alumina board over the heat pad to stabilize the temperature of the sensor as shown in Fig. 4.13(b).

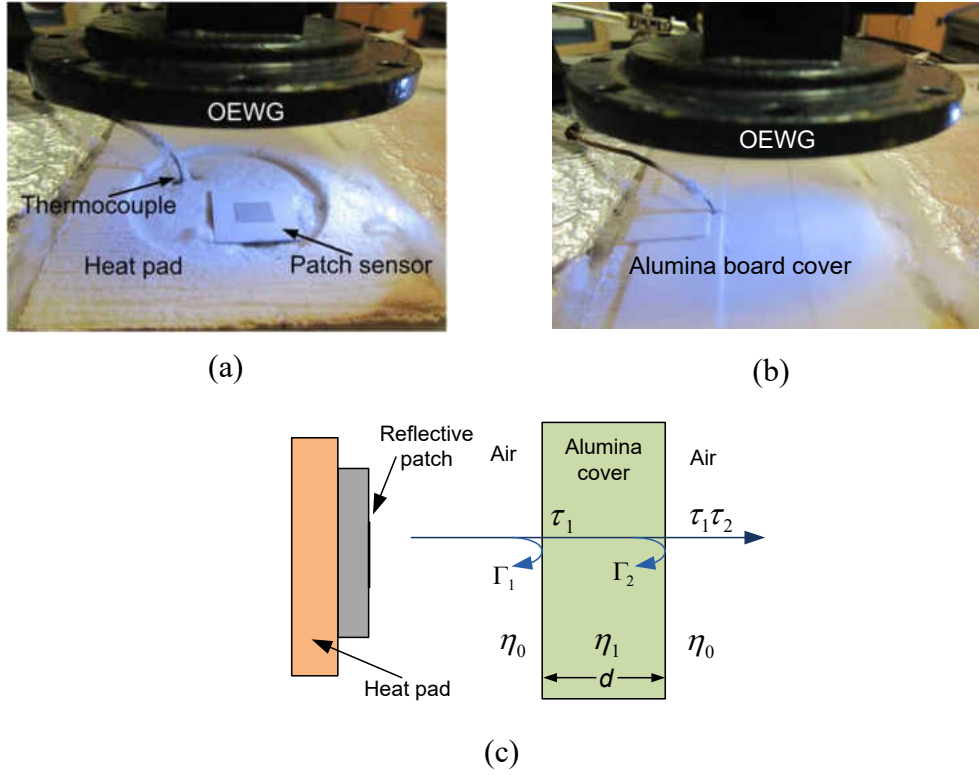


Figure 4.13: (a) Elevated OEWG for demonstration purpose. (b) The sensor is placed inside the heat pad with alumina board cover. (c) Schematic of wave reflections due to the alumina board cover with  $d = 0.635$  mm.

The re-radiated wave from the patch antenna gets reflections when passing through the alumina board cover due to the dielectric interface, as shown in Fig. 4.13(c). The total transition coefficient can be calculated by:

$$|\tau_1\tau_2| = \left| \frac{(1 + \Gamma_1)(1 + \Gamma_2)}{e^{j\beta_2 d} + \Gamma_2 e^{-j\beta_2 d}} \right| \quad (4.10)$$

For the alumina board used in the measurements, the loss due to the reflection is calculated to be about 0.4 dB.

The measurement setup includes a *G*-band OEWG antenna connected to an Agilent 40-GHz PNA-L (N5230A) for the wireless sensing after one port Short-Open-Load (SOL) calibration. The real-time sensor  $f_r$  is measured wirelessly for different temperatures with proper TD gating. The distance between the OEWG antenna and the patch sensor is fixed at 30 mm. It is observed that the temperature of the coaxial cable remains below 50°C even, when the heat pad is heated up to 1100°C.

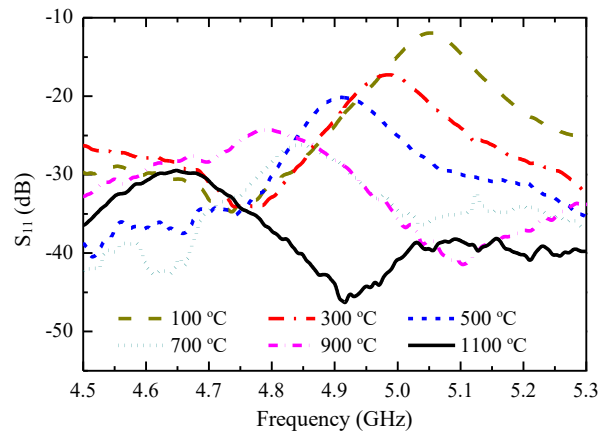


Figure 4.14: Measured  $S_{11}$  at successive temperatures up to 1100°C. Resonant frequency decreases with the increase in temperature.

Fig. 4.14 shows the measured  $S_{11}$  responses of the OEWG for temperatures from 50 to 1100°C in the air environment. For each temperature, the response curve has a unique peak with the highest signal level, corresponding to the resonant frequency of the patch antenna.

The resonant frequencies of the patch sensor for temperatures of 50-1100°C are extracted by reading each peak in Fig. 4.14, and plotted in Fig. 4.15. The resonant frequency decreases from 5.05 to 4.65 GHz in this temperature range, which corresponds to a measured sensor sensitivity

of 0.41 MHz/°C. Based on the dielectric constant of alumina characterized in Fig. 3.21, the resonant frequency of the reflective patch sensor is simulated up to 1000°C. It can be observed that the measurement match with the simulation very closely.

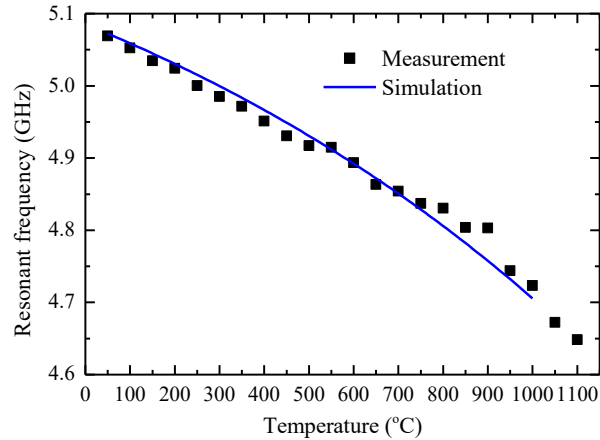


Figure 4.15: Simulated and Measured resonant frequency of the sensor versus temperature.

Considering the thermal expansion coefficient (CTE) of  $8.2 \times 10^{-6}/^{\circ}\text{C}$  for alumina substrate, the maximum dimensional change of the substrate is 0.86% from 50 to 1000°C, which is much less than the 15% resonant frequency change in this temperature range. Therefore, the dielectric constant change is the primary contributing factor to the resonant frequency variations.

The temperature sensors based on the reflective patch and the integrated resonator/antenna are compared in Table 4.1. Both two designs are able to survive high temperatures of at least 1000°C, due to the alumina substrate and platinum metallization. Compared with the rectangular cavity sensor, the patch sensor has easier fabrication because of the planar structure.

Table 4.1: Compare of different microwave high temperature sensors based on alumina.

	Mechanism	Dimensions (mm <sup>3</sup> )	Measured environment	$Q_T$ at 1000°C	Sensitivity
This work	rectangular reflective patch	21×21×0.635	Up to 1100°C in air	27	0.40 MHz/°C
[67]	Rectangular cavity resonator/antenna	22.86×5.93×1.016	Up to 1000°C in air	32	0.40 MHz/°C

#### 4.5 Conclusion

A novel wireless temperature sensor based on a reflective patch has been demonstrated for harsh environment applications. The reflective patch serves as both the temperature sensor and the radiating antenna simultaneously. Based on its simple design, low-profile, easy fabrication and high-temperature capability, the proposed temperature sensor is suitable for a wide range of applications such as gas turbine engines.

## CHAPTER 5      A ROBUST INTERROGATION ANTENNA

A robust antenna able to survive high temperatures is highly desirable for the wireless interrogation of sensors in harsh environment. In this chapter a robust antenna is realized to survive high temperatures up to 1300°C, after the fabrication process of platinum metallization and pattern is developed. In addition, this antenna is designed with a wide bandwidth by loading a rectangular stub in a slot antenna. Finally, by using this robust antenna, a temperature sensor is measured at high temperatures up to 1300°C.

### 5.1    Introduction of Robust Antennas for High-Temperature Applications

Based on the resonator/antenna integration presented in Chapter 3, a temperature sensor based on a cylindrical cavity resonator is also designed. This temperature sensor is fabricated using Si<sub>4</sub>B<sub>1</sub>CN ceramic substrate and platinum metal. In order to achieve high temperatures for the sensor measurement, a furnace is essential as shown in Fig. 5.1. This experiment setup facilitates the measurement of the Si<sub>4</sub>B<sub>1</sub>CN temperature sensor inside this furnace. For successful sensor measurement, a robust interrogation antenna is required to survive the high temperatures and remain working properly. In addition, the interrogation antenna requires a wide bandwidth to identify the sensor  $f_r$  which is dependent with the temperatures.



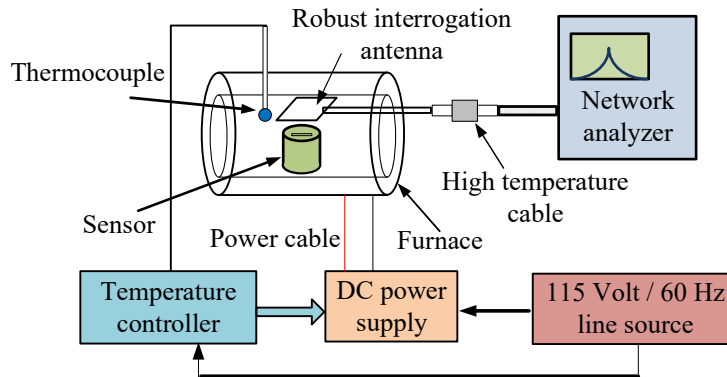


Figure 5.1: Schematic of measurement setup using a robust interrogation antenna.

The wireless interrogation of the sensor is shown in Fig. 5.2. During the measurement, the interrogation antenna transmits the microwave signal that excites the resonator sensor. Then the sensor re-radiates the resonant signal which is received by the interrogation antenna. Finally, the physical parameters detected by the microwave sensor can be measured wirelessly.

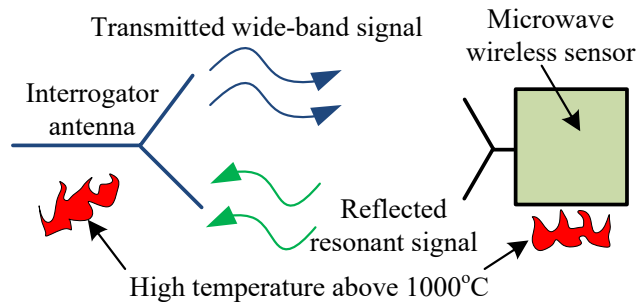


Figure 5.2: Schematic of wireless sensing system in harsh environment with proposed interrogation slot antenna.

However, there is no available robust antenna able to finish the sensor interrogation at high temperatures. A slot antenna with wide bandwidth was presented in [68] at around 2.2 GHz.

However, this antenna cannot survive in harsh environments due to the PCB fabrication. A folded slot antenna for harsh-environment application was proposed in [28]. This antenna was characterized up to 400°C, and it has a fractional bandwidth of 5% at 3.6 GHz. In addition, a ceramic patch antenna was presented in [69]. This antenna has a fractional bandwidth of 5% and is able to survive high temperatures up to 400 °C. All of the aforementioned antennas are not suitable for the high-temperature applications above 1000°C, due to the limited operating temperatures and narrow bandwidth.

## 5.2 Design and Analysis of the Proposed Robust Interrogation Antenna

In order to satisfy the aforementioned requirements as an interrogation antenna, a slot antenna with a wide bandwidth is proposed to survive high temperatures as shown in Fig. 5.3 [70]. The antenna impedance bandwidth is enlarged by loading a rectangular stub inside the slot antenna that is fed by a 50-ohm CPW line [68]. Additionally, this antenna is fabricated with a platinum metal layer on an alumina substrate with a thickness of  $h = 0.65$  mm, and is robust enough to operate properly at high temperatures.

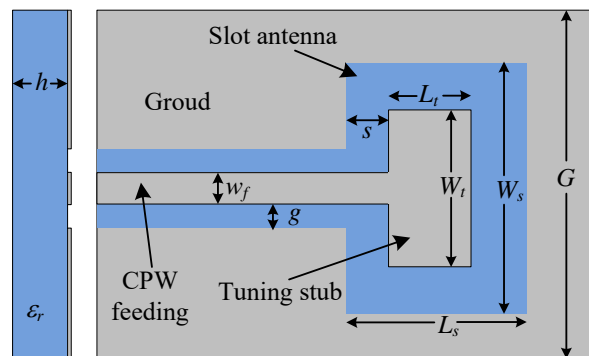


Figure 5.3: Structure of the slot antenna with a tuning stub.

The antenna design is performed by using the HFSS after a parameter study, and the process is described as follows.

(1) The effect of slot width  $W_s$  is simulated and shown in Fig. 5.4(a). It can be observed that the antenna matching is better by increasing  $W_s$ . So  $W_s = 8.4$  mm is chosen for the slot width.

(2) Fig. 5.4(b) shows that the decreased tuning-stub width  $W_t$  enlarges the impedance bandwidth. Therefore,  $W_t = 5.4$  mm is used.

(3) The tuning-stub length  $L_t$  and the slot length  $L_s$  are varied, and the simulated results are shown in Fig. 5.4(c) and Fig. 5.4(d), respectively. Finally,  $L_t = 1.9$  mm and  $L_s = 8.6$  mm are chosen for adjusting the center frequency and for better impedance matching. The impedance bandwidth of the designed antenna is 9.25-11.46 GHz.

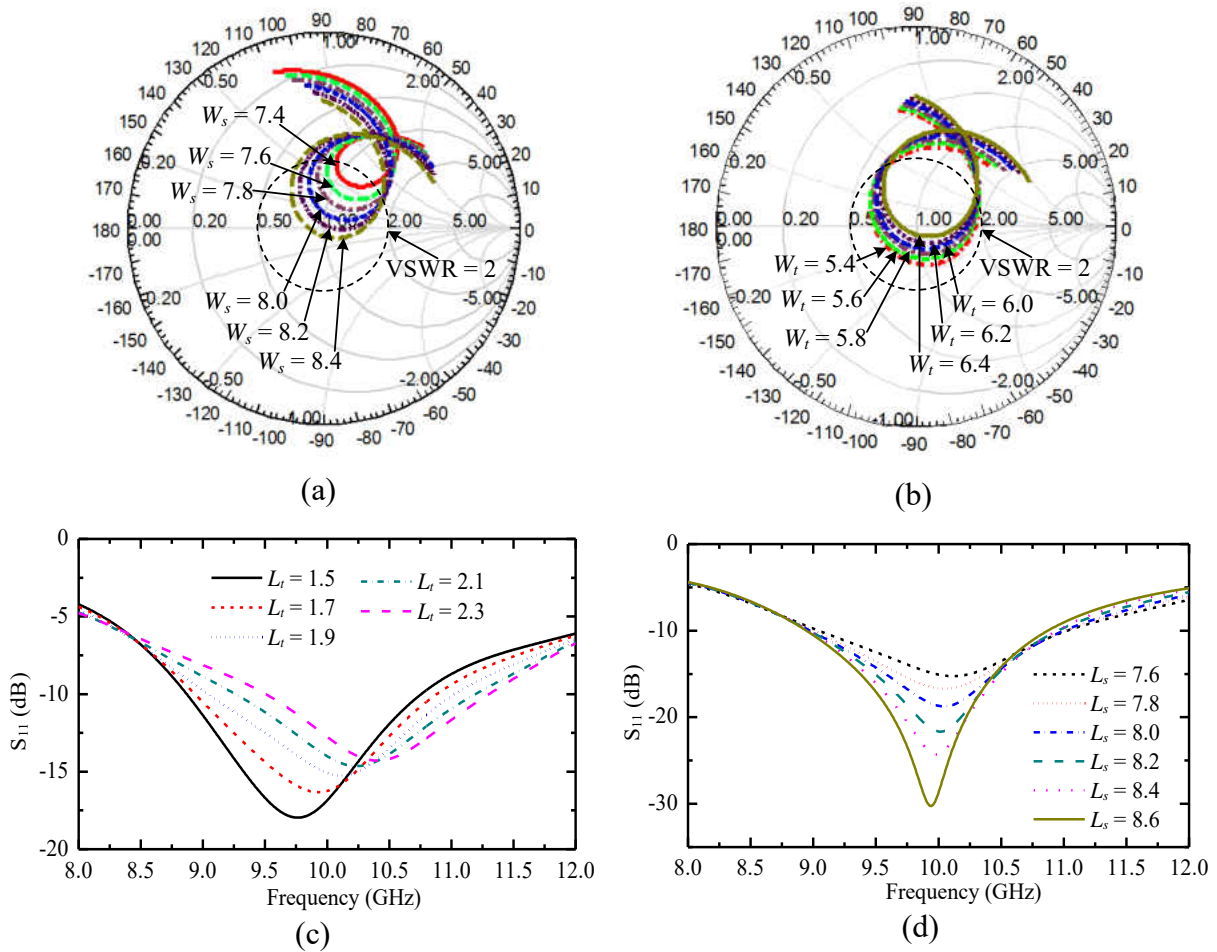


Figure 5.4: Simulated  $S_{11}$  responses for various antenna parameters: (a) slot width  $W_s$ . (b) tuning-stub width  $W_t$ . (c) tuning-stub length  $L_t$ . (d) slot length.

During the antenna design, the spacing between the tuning stub and the slot edge is fixed as  $s = 0.6$  mm. The antenna dimensions are summarized in Tab. 5.1. It should be noticed that the dielectric constant  $\epsilon_r$  of the alumina substrate increases with temperature, and this antenna design is based on  $\epsilon_r = 11.2$  at  $1000^\circ\text{C}$  [67].

Table 5.1: Dimensions of the designed slot antenna.

Symbol	Parameters	Values (mm)
$w_f$	Feed width	2.5
$g$	Gap	0.63
$s$	Spacing	0.6
$W_t$	Tuning-stub width	5.4
$L_t$	Tuning-stub length	1.9
$W_s$	Slot width	8.4
$L_s$	Slot width	8.6
$G$	Ground size	25
$h$	Substrate thickness	0.65

Electric field distribution in the slot area is simulated to analyze this slot antenna. Three frequencies inside the impedance bandwidth, i.e. 9.6, 10.6 and 11.4 GHz, are selected, and the corresponding electric fields are plotted in Fig. 5.5.

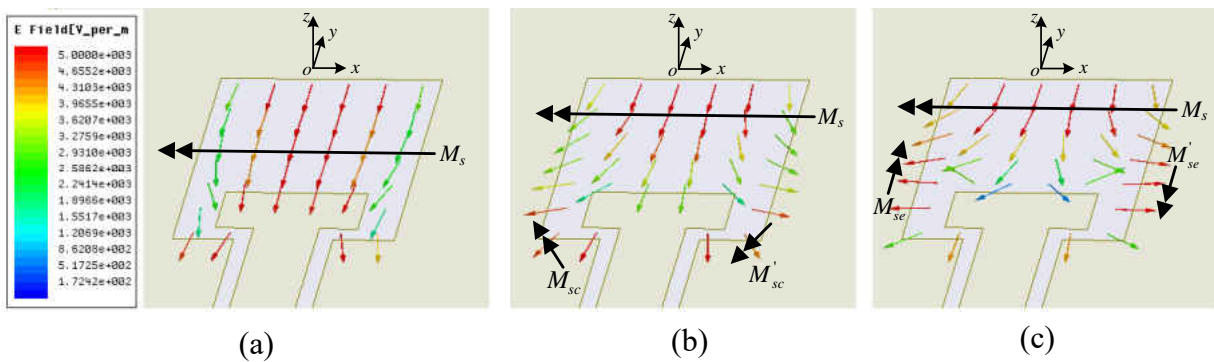


Figure 5.5: Electric field distributions in the slot area at (a) 9.6 GHz, (b) 10.6 GHz and (c) 11.4 GHz. The equivalent magnetic currents are labeled.

As shown in Fig. 5.5(a), the electric field at 9.6 GHz is mainly in the  $y$  direction and concentrates in the middle of the slot. Accordingly, the equivalent magnetic current  $M_s$  that leads to antenna radiation is represented as:

$$M_s = -\hat{n} \times E_a \quad (5)$$

Compared with Fig. 5.5(a) that corresponds to 9.6 GHz, Fig. 5.5(b) shows the existence of additional electric fields at the two slot corners at 10.6 GHz. The two corresponding magnetic currents  $M_{sc}$  and  $M_{sc}'$  are of the same magnitude but  $180^\circ$  out of phase. Therefore, the radiations caused by the two magnetic currents cancel with each other, and the total radiation of this slot antenna is mainly due to the  $M_s$  in  $x$  direction, similar to Fig. 5.5(a). Additionally, Fig. 5.5(c) shows that the radiation resulting from the  $M_{se}$  cancels that from the  $M_{se}'$  at 11.4 GHz.

By plotting the electric field distributions at different frequencies, the antenna polarization is observed to remain in the same direction inside the whole impedance bandwidth. The polarization analysis is useful for alignment of the interrogation antenna with the sensor/antenna to minimize the polarization mismatch loss during the sensor interrogation.

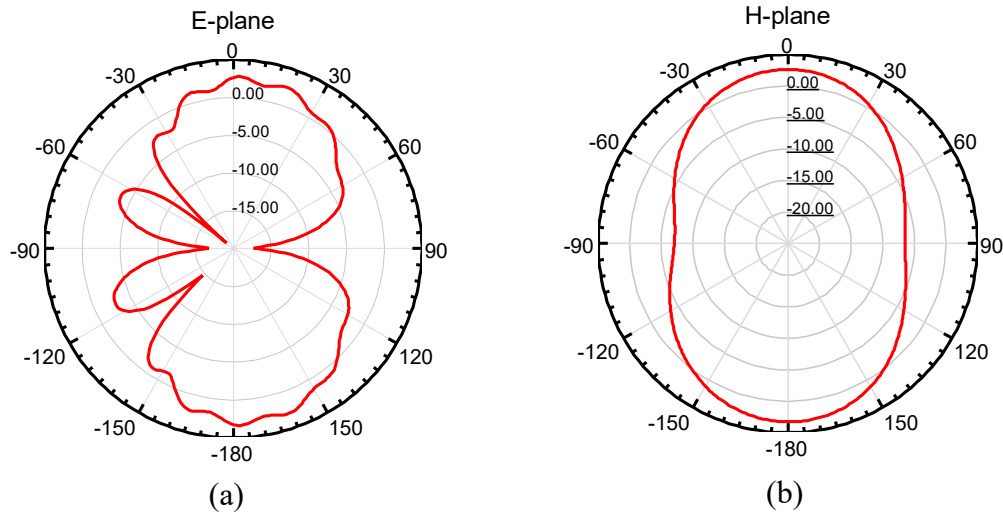


Figure 5.6: Radiation pattern of the slot antenna. (a) E-plane. (b) H-plane.

Fig. 5.6 shows simulated radiation patterns of the antenna on E- and H-planes. The antenna radiation is roughly bidirectional due to the slot structure: The antenna gain is 2.7 dBi on the front side (the platinum metal side) and 3.3 dBi on the backside (the alumina substrate side). Therefore, the sensor is placed under the interrogation antenna substrate for larger antenna gain during the wireless measurement. The antenna sidelobe on the E-plane plotted in Fig. 5.6(a) is due to wave leaking from the CPW-feeding line. The antenna efficiency is simulated to be 62% due to the relatively low platinum conductivity at high temperatures.

### 5.3 Fabrication of the Robust Antenna after Development of Platinum Pattern Process

A platinum pattern process is developed to fabricate this robust slot antenna. The process flow is shown in Fig. 5.7 and described as follows.

- (1) The designed antenna layout is printed on a toner transfer paper by using a laser printer with a printing resolution of 1200 dpi as shown in Fig. 5.7(a).
- (2) The transfer paper is placed on an alumina substrate and then the ink is transferred to the alumina substrate using a thermal compression process, as shown in Fig. 5.7(b).
- (3) Platinum paste (ESL 5542) is applied on the alumina substrate to form the antenna layout. Then the paste is dried on a hotplate for 2 minutes at 110°C as shown in Fig. 5.7(c).
- (4) A platinum layer is formed using a high-temperature sintering process that is also used for the metallization of the cylindrical resonator. Fig. 5.7(d) shows the antenna after the high-temperature sintering.

The metallization processes presented in Fig. 5.7(c) and (d) are repeated three times to accumulate the platinum layer thickness to around 25  $\mu\text{m}$ . Fig. 5.7(e) shows the fabricated antenna that is soldered with high-temperature solder (91Pb4Sn4Ag1In, melting point: 313°C, Indium Corporation).



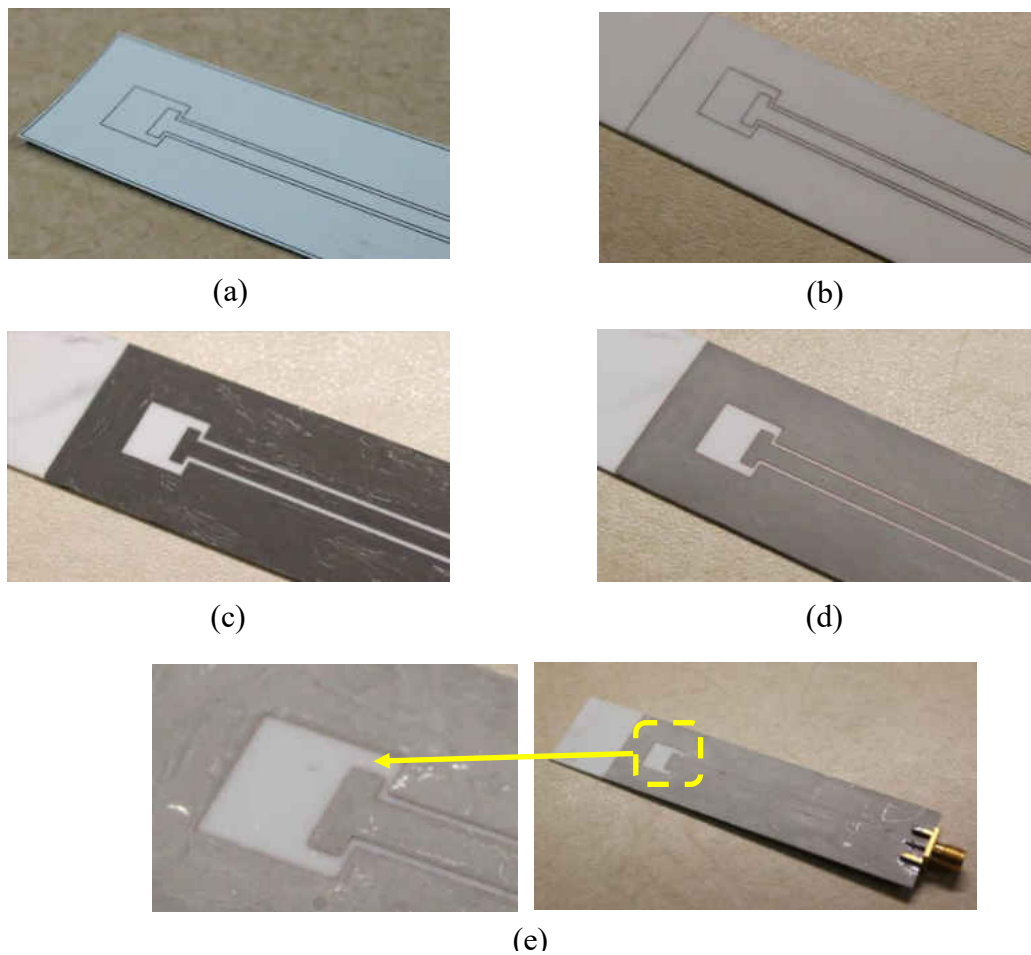


Figure 5.7: Fabrication of the slot antenna. (a) Antenna layout on transfer paper. (b) Antenna layout transferred to alumina substrate. (c) Pattern of the platinum paste. (d) Platinum after high temperature sintering. (e) Fabricated antenna.

Thru-Reflect-Line (TRL) calibration is performed to remove the effect due to the mismatching between the SMA connector and the CPW line [71]. PCB boards (Rogers 3010, thickness of 0.65 mm) that have same dielectric constant  $\epsilon_r$  and thickness  $h$  with the alumina substrate are used to fabricate the TRL calibration kits for the easy fabrication.

The fabricated calibration kits are shown in Fig. 5.8(a), and the lengths for the Thru, Reflect and Line kits are designed as 136 mm, 68 mm and 139.9 mm, respectively. After the TRL calibration,  $S_{11}$  response of the slot antenna is measured at room temperature and shown in Fig. 18. The measured  $S_{11}$  shows a center frequency of 10.36 GHz and a 21.3% fractional bandwidth, which matches with the simulation very well.

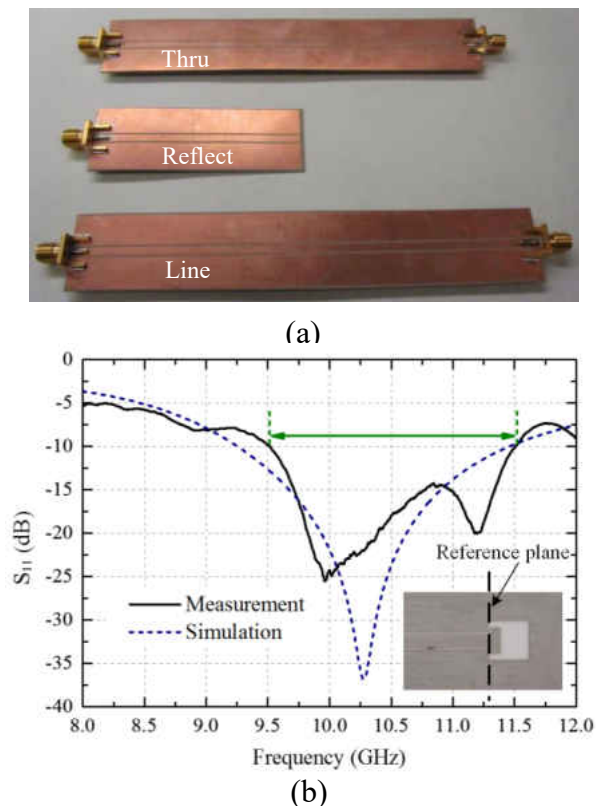


Figure 5.8: (a) TRL calibration kits. (b) Measured and simulated  $S_{11}$  response of the slot antenna at room temperature.

#### 5.4 Temperature Sensor Measurement by using the Robust Interrogation Antenna

The  $\text{Si}_4\text{B}_1\text{CN}$  temperature sensor, as shown in Fig. 5.9(a), is measured by using the robust interrogation antenna. The interrogation antenna and the sensor/antenna are aligned to minimize

the polarization loss, based on the electric field distribution analyzed in Fig. 5.5. Additionally, the sensor is placed under the alumina substrate of the interrogation antenna, since the antenna gain is maximal on the backside of the interrogation antenna as presented in Fig. 5.6.

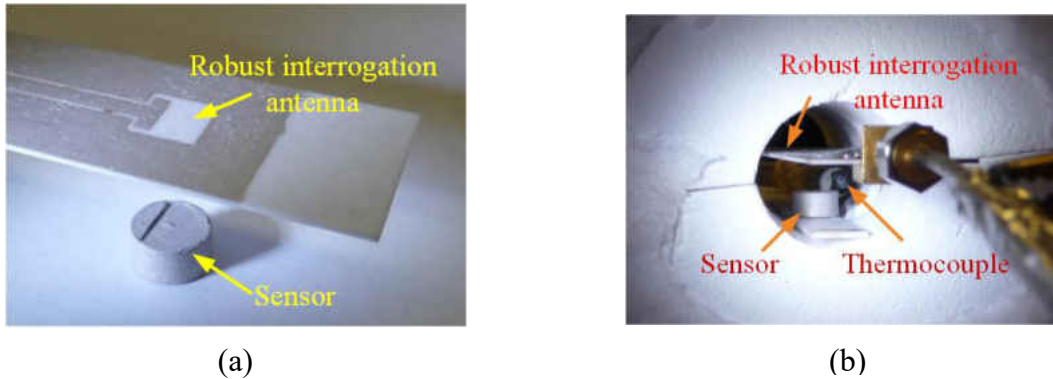


Figure 5.9: Measurement setup. (a) The interrogation antenna and the sensor/ antenna. (b) The interrogation antenna and sensor located in the furnace.

In order to measure the sensor responses at high temperatures, a measurement setup is custom-made by using a cylindrical furnace (Robust Radiator<sup>TM</sup> from Micropyretics Heaters International Inc., RHUL-MP1125-4) fed by a DC power supply as described in Fig. 5.2. The measurement temperature is monitored by a *K*-type thermocouple and controlled by a temperature controller. The interrogation antenna is connected with the Agilent 40-GHz PNA-L by using a high temperature cable (Time Microwave Systems).

During the measurement, the interrogation antenna is inserted into the furnace, while the SMA connector and the high temperature cable are located outside of the furnace as shown in Fig. 5.9 (b). In addition, alumina silica ceramic fiber extreme-temperature sheeting (alumina wool) is used to seal the two open ends of the cylindrical furnace for stable temperature. It is observed

that the temperature of the SMA connector is about 100°C, while the temperature inside the furnace increases up to 1300°C.

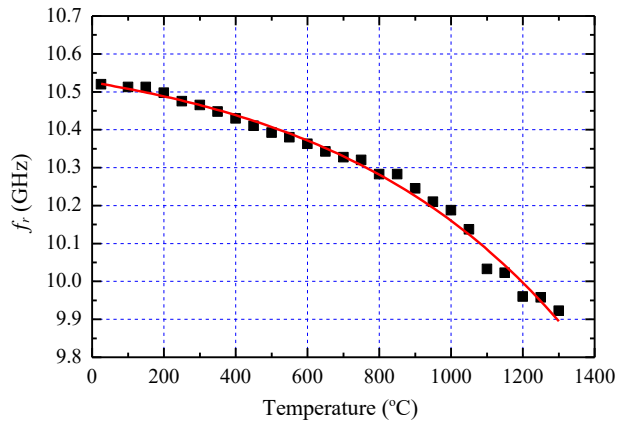


Figure 5.10: Measurement of the temperature sensor using  $\text{Si}_4\text{B}_1\text{CN}$  substrate.

The sensor using  $\text{Si}_4\text{B}_1\text{CN}$  substrate is measured up to 1300°C. The real-time  $f_r$  of the temperature sensor are extracted and shown in Fig. 5.10 after TD gating. It is observed that the measured  $f_r$  decreases monotonically from 10.5 to 9.9 GHz with the increasing temperature from 25 to 1300°C. In addition, the measured  $Q$  is 31 at temperatures.

## 5.5 Conclusion

A slot antenna is successfully designed with a wide bandwidth by loading a rectangular tuning stub in the slot area. In addition, the antenna polarization and pattern are also analyzed. After the process development of platinum metallization and pattern, this antenna is fabricated and measured. The measured antenna response at room temperature matches the simulated result

very well. By using this robust antenna as an interrogation antenna, a temperature sensor is measured at high temperatures up to 1300°C.

## **CHAPTER 6      A PRESSURE SENSOR BASED ON AN EVANESCENT-MODE RESONATORS**

This chapter presents a pressure sensor by using a newly developed SiACN ceramic for harsh-environment applications. The pressure sensor is low profile due to the compact design of an evanescent-mode resonator that is coupled with a patch antenna. A fabrication process of PDC machining is developed, and a ceramic pressure sensor is fabricated. Finally, the pressure sensor is characterized under various pressures at high temperatures.

### **6.1    Pressure Sensor Mechanism**

As introduced in Chapter 1, real-time monitoring of pressure is critical to improve the efficiency and reliability of a turbine engine. In this chapter, we will demonstrate a compact wireless passive pressure sensor for harsh-environment applications using high-Q evanescent-mode resonators, robust ceramic and metallic materials, and integrated antenna.

The authors presented an evanescent-mode-resonator-based wireless passive pressure sensor design with integrated slot antenna to achieve compact size [15]. In this chapter, we will use a similar evanescent-mode resonator structure [15] but employ an integrated patch antenna to enhance the sensing range. This integrated patch antenna also exhibits zero additional volume. The small size of the pressure sensor can minimize the adverse effects on the aerodynamic flow inside turbines or other devices. The proposed pressure sensor is made of high-temperature-stable materials including fully-dense SiAlCN and platinum, which have been proven to work

reliably above 1000°C [16]-[18]. This pressure sensor will be wirelessly interrogated by a high-temperature-stable antenna without the need of wire connections to the sensor. The schematic of the pressure sensor structure and wireless interrogation mechanism is illustrated in Fig. 6.1.

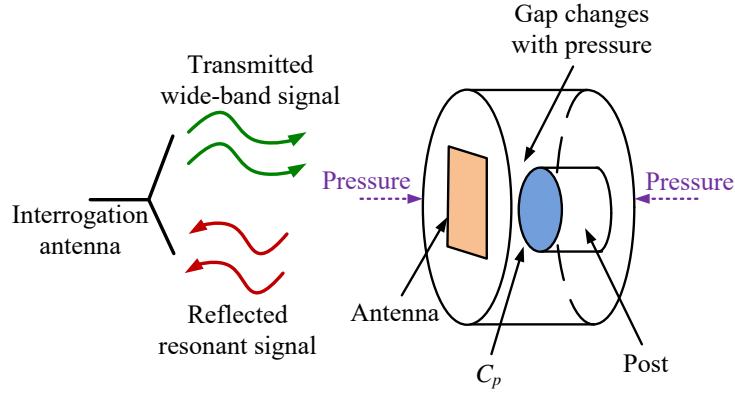


Figure 6.1: Schematic of the wireless pressure sensor based on an evanescent-mode cavity resonator.

The resonant frequency  $f_r$  of the evanescent-mode resonator is determined by [19]:

$$f_r = \frac{1}{2\pi\sqrt{L(c_p + c_r)}} \quad (6.1)$$

where  $c_p$  represents parallel-plate capacitance between the cavity cap and the cylindrical post inside the cavity,  $c_r$  is the remaining fringing capacitance, and  $L$  is the equivalent inductance. With pressure being applied on the cavity,  $c_p$  increases with the reduced gap due to cavity deformation. Therefore, the pressure can be wirelessly monitored by measuring the change in  $f_r$ . By adding the post structure in the cavity resonator as shown in Fig. 6.1, high sensitivity of the pressure sensor is achieved due to a small gap value [20]. It is worthy of mentioning that this type

of evanescent-mode resonators have been also used for high-Q widely-tunable filters [21]-[24], owing to the merits of reduced size and high sensitivity.

## 6.2 Characterization of the Fully-Dense SiAlCN PDC

Structure material of the pressure sensor is fully-dense SiAlCN ceramic which exhibits excellent thermal resistance and mechanical properties at high temperatures [16]-[17]. However, as a novel ceramic material, the dielectric properties at microwave frequency including dielectric constant and loss tangent were still unknown. Therefore, it is necessary to measure the dielectric properties of the fully-dense SiAlCN PDC before the sensor design and fabrication. Dielectric characterization is carried out by using the microwave cavity method presented in [18].

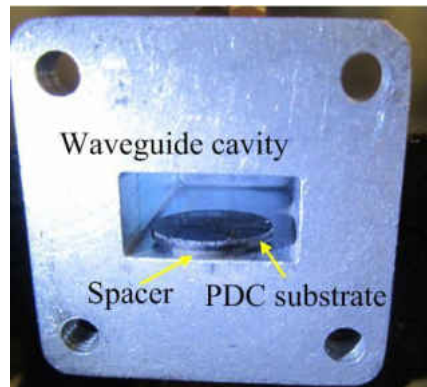


Figure 6.2: Characterization of dielectric properties of the SiAlCN PDC in a microwave cavity at room temperature.

The fully-dense SiAlCN PDCs are synthesized by using 10% and 30% poly (melamine-co-formaldehyde) acrylated solution (PVN, Sigma-Aldrich, St. Louis, MO) [25]. The SiAlCN PDC



substrate is placed on a spacer inside a Ku-band waveguide cavity for dielectric characterization, as shown in Fig. 6.2. Then the dielectric constant and loss tangent of the SiAlCN PDC can be extracted from the resonant frequency and loaded Q factor of the waveguide cavity [18]. The dielectric constant (loss tangent) for PDCs with 10% and 30% PVN are found to be 5.1 (0.01) and 6.3 (0.05), respectively. SiAlCN PDC with 10% PVN is selected to fabricate the sensor cap due to its lower dielectric loss. However, SiAlCN PDC with 30% PVN is used for sensor bottom since this composition can provide thick substrates without warping. Since the sensor bottom will be completely metallized using platinum, the loss inside the lossy PDC with 30% PVN will not affect the Q factor the pressure sensor.

### 6.3 Design of the Pressure Sensor and Robust Interrogation antenna

This wireless pressure sensor is designed for high-temperature applications, and therefore constraints from microwave resonator design, ceramic synthesis and fabrication limitation need to be carefully considered throughout the sensor design. A patch antenna is seamlessly integrated with the pressure sensor to receive the interrogation signal and transmit the sensor response. In addition, a robust interrogation antenna with sufficiently-wide fractional bandwidth is developed in order to perform sensor measurements.

#### 6.3.1 *Design of the Pressure Sensor based on an Evanescent-Mode Cavity Resonator*

The considerations from microwave resonator design, ceramic synthesis and machining are listed as follows. (1) There is a tradeoff between sensor size and Q factor. When the resonator is heavily loaded, the size of the sensor is reduced as well as the resonant frequency. The reduced

resonant frequency will lead to less free-space path loss and therefore increase sensing range. However, the associated reduction in Q factor will adversely affect the sensing range. Therefore, iterations in design are needed to maximize the sensing range. (2) The thickness of fully-dense SiAlCN PDC is limited to be below 1500  $\mu\text{m}$  in order to avoid cracks or warping during sintering. Details will be provided in Section 3. (3) The pressure sensor needs to be able to respond to 0-600 psi pressure change without mechanical structure breakdown. If the cap of the sensor is too thick, the pressure sensor is not sensitive to the pressure change. However, cap thicknesses below a critical value will lead to RF shorting when the cap touches the post. In addition, the sensor cap may break down when the stress caused by the external pressure exceeds the ultimate tensile strength (UTS) of the PDC ceramic, which is approximately 1000 MPa.

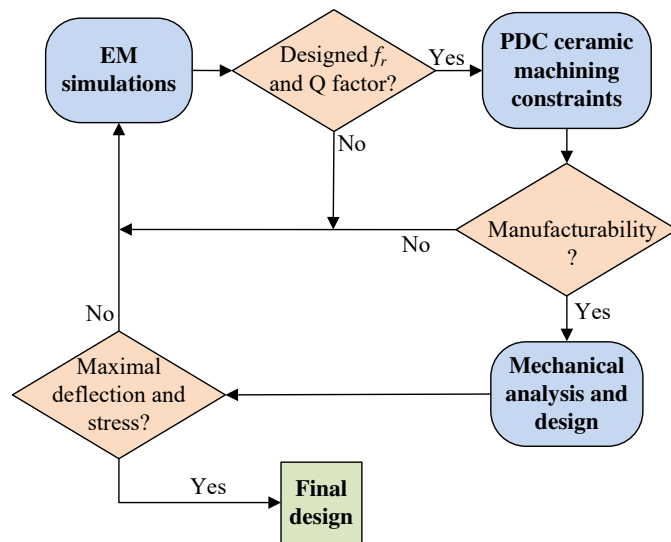
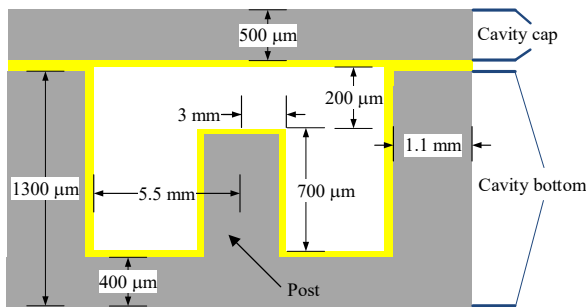


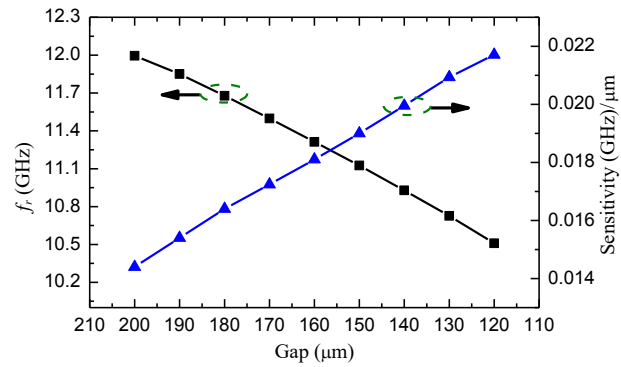
Figure 6.3: Flow chart to design the microwave pressure sensor.

The design flow chart is presented in Fig. 6.3. The dimensions of the pressure sensor after optimization are listed in Fig. 6.4(a). The relationship between resonant frequency and gap size

is presented in Fig. 6.4(b) using ANSYS High Frequency Structure Simulator (HFSS) simulations. It is noted that the resonant frequency decreases when the gap size (external pressure) becomes smaller (larger). The sensitivity of the sensor becomes higher when the gap size is smaller.



(a)



(b)

Figure 6.4: Optimized design of the evanescent-mode-resonator pressure sensor. (a) Side view with dimensions. (b) Simulated resonant frequency of the pressure sensor versus cavity gap.

To verify the robustness under pressure, this pressure sensor was simulated in ANSYS Mechanical. As shown in Fig. 6.5(a), the deflection of the cavity cap is found to be  $69.8 \mu\text{m}$  when the external pressure is 600 psi, which makes sure that no RF shorting will occur during sensor operation. In addition, the maximal stress in the sensor cap is simulated to be 298.6 MPa as shown in Fig. 6.5(b), which is much smaller than the UTS of PDC. During this mechanical simulation, the Young's modulus of the SiAlCN PDC is set as 100 GPa, and the bottom of the sensor is assumed to be flat, which corresponds to the case when the pressure sensor is mounted on a rigid surface.

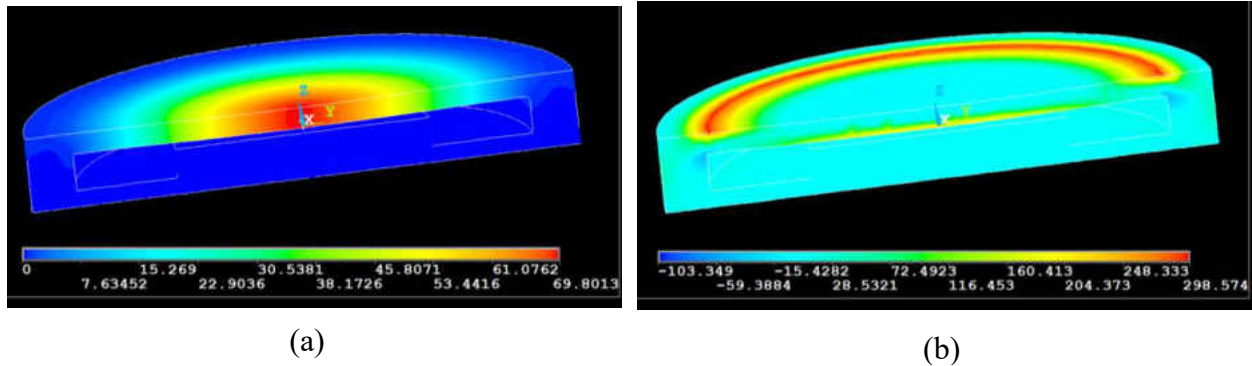


Figure 6.5: Mechanical simulations of the pressure sensor under 600 psi pressure. (a) Sensor deformation. (b) Stress distribution.

### 6.3.2 Design of the Patch Antenna Coupled with the Pressure Sensor

A patch antenna is designed to be seamlessly integrated with the pressure sensor in order to facilitate the wireless interrogation and minimize size as shown in Fig. 6.6. The patch antenna is located on the top surface of the sensor cap and coupled to the pressure sensor through a rectangular slot etched inside the ground plane on the bottom of the sensor cap. Similar to the filter/antenna integration technique presented in [26], this integrated patch antenna occupies zero additional volume and exhibits close to 100% antenna efficiency.

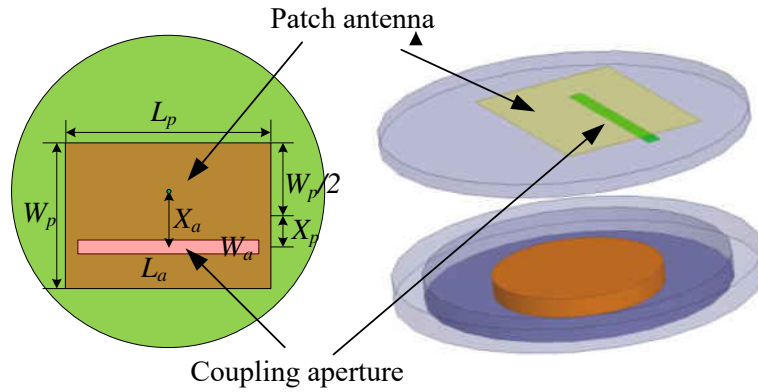


Figure 6.6: Top (left) and 3-D (right) view of the patch antenna integrated with the pressure sensor. The patch antenna is at the top surface of the ceramic cap. The coupling aperture is at the bottom surface of the ceramic cap.

The patch antenna is designed using the dielectric properties measured in Section 2. The patch length  $L_p$  and width  $W_p$  are found to be 5.4 and 7.1 mm, respectively at the resonant frequency of the pressure sensor, i.e.  $f_r = 11.9$  GHz. It is noted that  $\epsilon_r = 5.36$  (assuming 5% increase from  $\epsilon_r = 5.1$  at room temperature) is used for the PDC with 10% PVN at 700°C, based on the temperature-dependent dielectric properties of similar SiCN ceramics reported in [18].

The length of the coupling aperture  $L_a$  and location of the patch antenna  $X_p$  are then studied and optimized for maximum sensing range in HFSS. In order to carry out this parametric study, an X-band open-ended waveguide (OEWG) antenna with an aperture size of  $22.86 \times 10.16$  mm<sup>2</sup> is used to interrogate the pressure sensor as shown in Fig. 6.7(a). This OEWG antenna transmits a wide-band RF signal, which couples to the sensor through the integrated patch antenna. Only the frequency components close to the resonant frequency of the sensor resonate for many cycles and re-radiate back to the OEWG. By using a time-domain gating technique [27], the responses corresponding to the resonance inside the pressure sensor are isolated and identified by the

network analyzer. OEWG antenna  $S_{11}$  versus  $L_a$  and  $X_p$  are plotted in Fig. 6.7(b) and Fig. 6.7(c), respectively. The peaks of the curves correspond to the resonant frequency of the pressure sensor. Finally,  $L_a = 6$  mm and  $X_p = 0.8$  mm are chosen to achieve a good compromise between the received signal strength and Q factor (which determines the sharpness of the peaks). During the antenna design, the width and location of the coupling aperture are fixed as  $W_a = 0.5$  mm and  $X_a = 2$  mm, respectively.

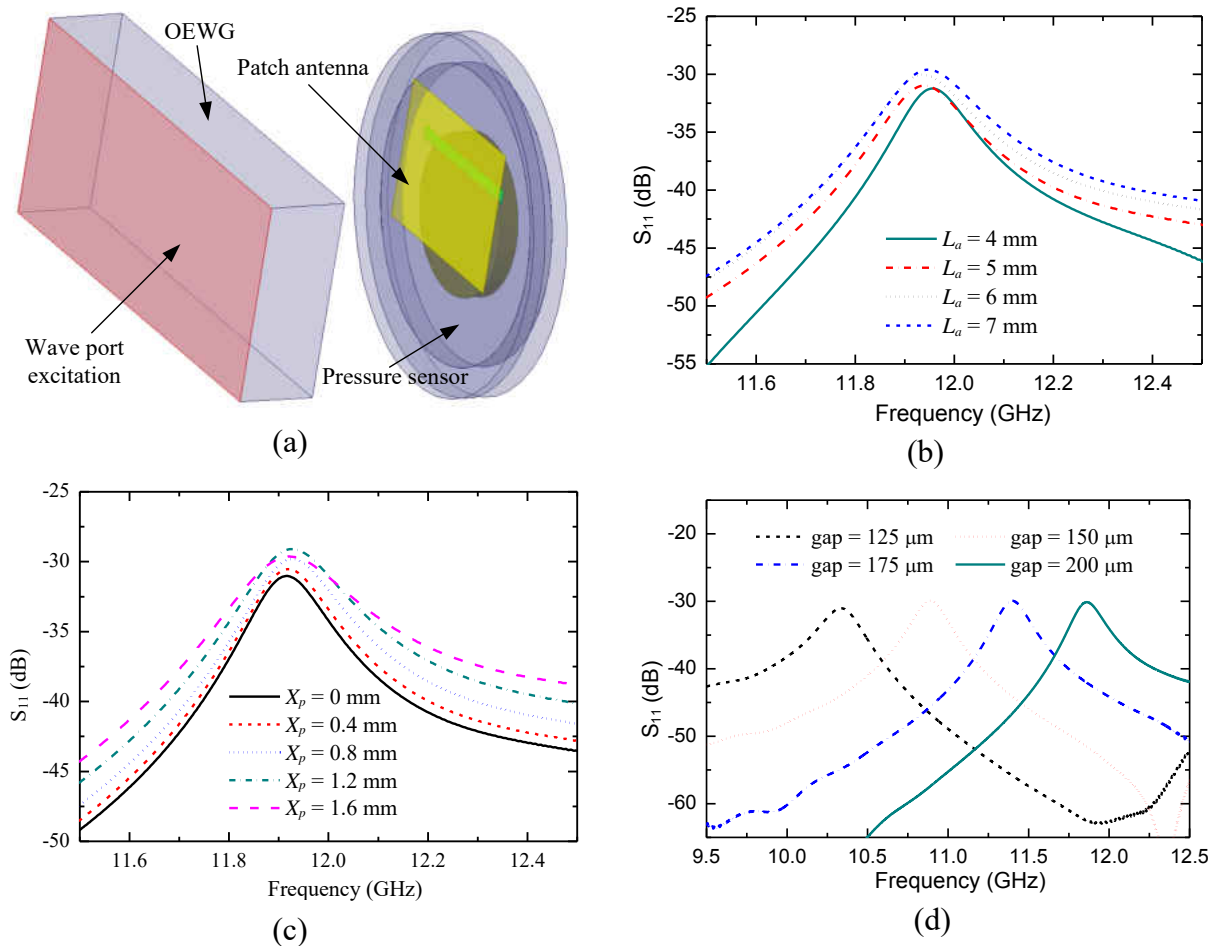


Figure 6.7: (a) Simulation setup for the wireless interrogation of the pressure sensor in HFSS. Parametric study of (b) patch length  $L_a$ . (c) coupling position  $X_p$  for the integrated patch antenna. (d) Sensor responses versus different gap sizes inside the cavity.

The dimensions of the patch antenna and coupling aperture are summarized in Table 6.1. To verify that this wireless interrogation can detect the resonant frequency change of the sensor, simulated sensor responses versus different gap sizes are shown in Fig. 6.7(d). It is apparent that under different external pressures, the resonant frequency of the pressure sensor can be wirelessly detected.

Table 6.1: The dimensions of the patch antenna.

Symbol	Parameters	Values (mm)
$W_p$	Patch width	7.1
$L_p$	Patch length	5.4
$W_a$	Coupling aperture width	0.5
$L_a$	Coupling aperture length	6
$d$	Coupling aperture location	2
$x_p$	Patch offset $X_p$	0.8

### 6.3.3 Design of the Robust Interrogation Antenna with Wide Bandwidth

Ideally, the wireless pressure sensor needs to be tested within a chamber with both high temperatures (up to 1000°C) and high pressures (up to 600 psi). In addition, RF signals need to be sent to the inside of the chamber in order to wireless interrogate the sensor. All these requirements call for very complicated and challenging measurement setup. In this paper, we will focus on the demonstration of the working mechanism of this novel wireless passive pressure sensors. Therefore, a measurement setup as shown in Fig. 6.8(a) is used instead. The temperature of the sensor is controlled by a heat pad under the pressure sensor. While the pressure on the sensor is applied with an alumina rod passing through the interrogator antenna.

This simple setup allows us to emulate the sensor cavity deformation caused by ambient pressure change. It should be noted that the loading effect of the alumina rod on the resonant frequency of the pressure sensor is negligible, i.e. a slight frequency down shift of 0.0048 GHz at 11.9 GHz through HFSS simulations.

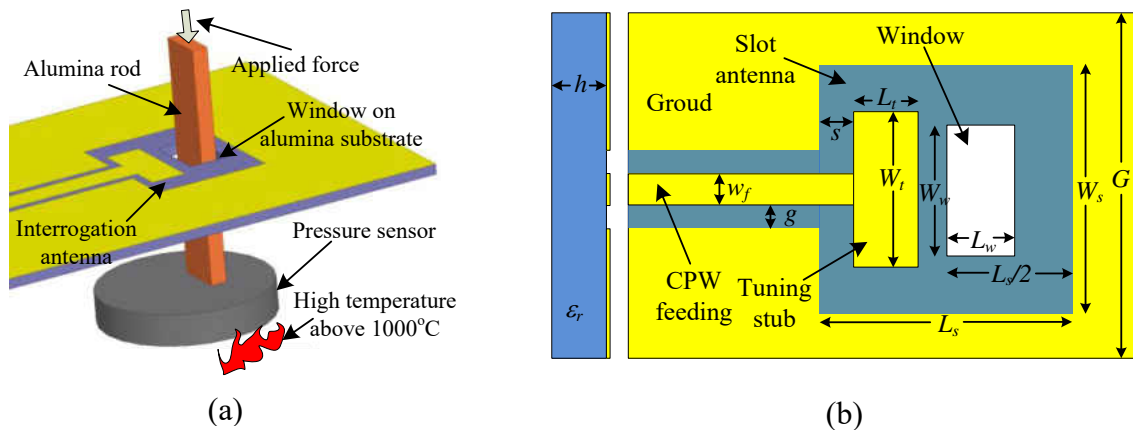


Figure 6.8: Interrogation antenna for pressure sensor measurement at high temperatures. (a) The schematic of the pressure sensor measurement with the interrogation antenna. (b) The schematic of the slot antenna loaded with a rectangular tuning stub.

There are two requirements for the interrogation antenna: (1) it needs to be robust to survive high temperatures; (2) its fractional bandwidth should be wide enough to cover the entire frequency range of the pressure sensor for different pressures. A robust antenna to interrogate temperature sensor was proposed in [28], and it is able to survive high temperatures up to 1300°C by using an alumina substrate and a platinum metal layer. Similarly, a robust antenna is designed herein for the pressure sensor measurement. As shown in Fig. 6.8(b), a tuning stub with CPW feeding is loaded inside the slot antenna to improve the antenna bandwidth. A window is cut inside the antenna substrate, allowing the alumina rod to apply a force on the pressure sensor.



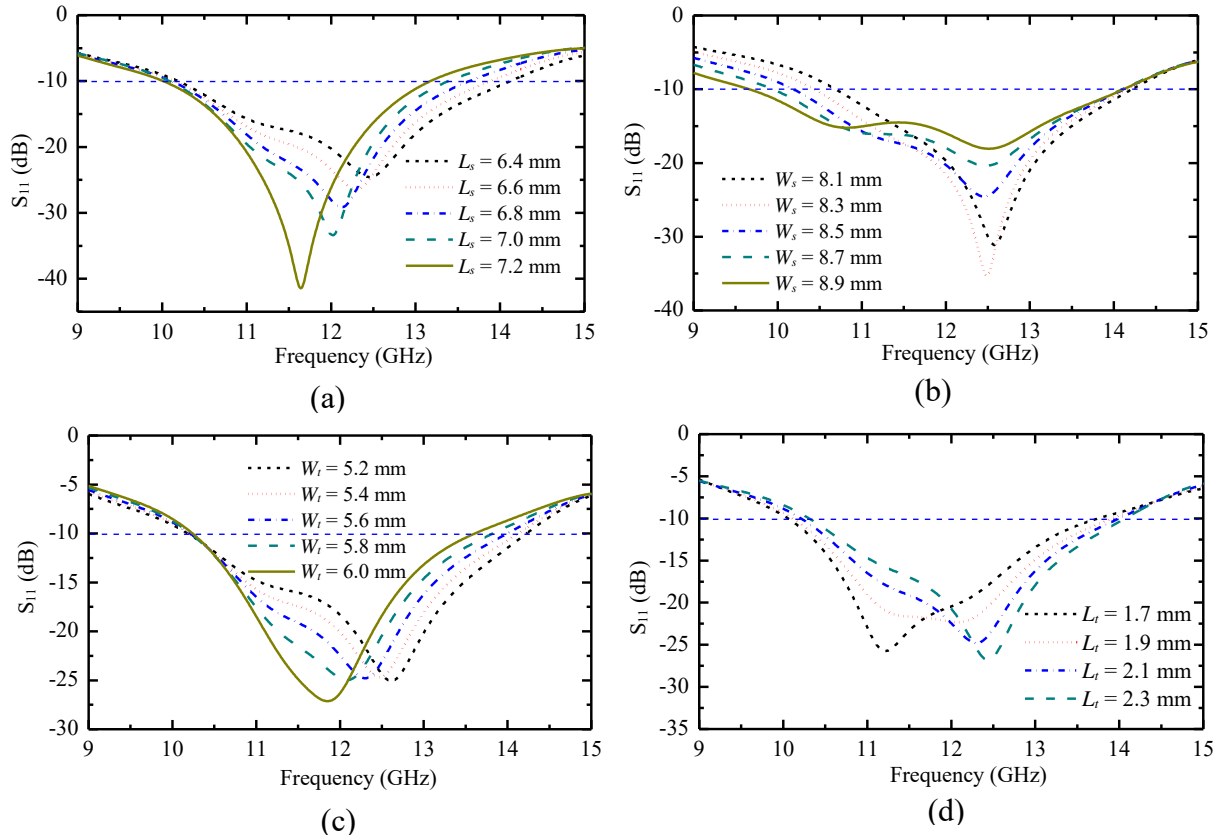


Figure 6.9: Parameter study of (a) the slot length  $L_s$ , (b) the slot width  $W_s$ , (c) the tuning-stub width  $W_t$  and (d) the tuning-stub length  $L_t$  of the interrogation antenna.

As shown in Fig. 6.9, the slot length  $L_s$ , slot width  $W_s$ , tuning-stub length  $L_t$ , and tuning-stub width  $W_t$  are studied to optimize the antenna bandwidth. It is noted that the spacing between the tuning stub and the slot edge is chosen as  $s = 0.6$  mm. Fig. 6.9(a) shows that the upper bound of the antenna impedance matching bandwidth is increased for smaller  $L_s$ . So  $L_s = 6.4$  mm is chosen for this antenna design. Then it is observed in Fig. 6.9(b) that the lower bound of the antenna impedance matching bandwidth is determined by  $W_s$ . Therefore,  $W_s = 8.5$  mm is used. Finally, the effects of  $W_t$  and  $L_t$  are studied and shown in Fig. 6.9(c) and Fig. 6.9(d), respectively.  $W_t =$

5.6 mm and  $L_t = 2.1$  mm are chosen for better impedance matching. The dimensions of the designed interrogation antenna are summarized in Table 6.2. The designed interrogation antenna exhibits a fractional bandwidth of 31% ( $S_{11} < -10$  dB) at the center frequency of 12.1 GHz.

Table 6.2: The dimensions of the interrogation antenna.

Symbol	Parameters	Values (mm)
$w_f$	Feed width	2.5
$g$	Gap	0.63
$s$	Spacing	0.6
$W_t$	Tuning-stub width	5.6
$L_t$	Tuning-stub length	2.1
$W_s$	Slot width	8.5
$L_s$	Slot width	6.4
$G$	Ground size	22.9
$h$	Substrate thickness	0.635
$L_w$	<i>Window length</i>	2.5
$W_w$	<i>Window width</i>	4

As shown in Fig. 6.8(a), an alumina rod with a cross-sectional area of  $0.9 \times 0.6 \text{ mm}^2$  is inserted through the interrogation antenna. The loading effect of the alumina rod on resonant frequency of the interrogation antenna is also verified in HFSS simulations. It is observed that the center frequency of the interrogation antenna is decreased by 0.1 GHz while the antenna fractional bandwidth remains the same, which is still sufficient to cover the sensor responses.

## 6.4 Fabrication of the PDC Pressure Sensor and the Robust Interrogation Antenna

In this section, the details of sensor fabrication using fully-dense PDC and platinum, as well as the interrogation antenna fabrication are presented.

### 6.4.1 Fabrication Process of PDC Pressure Sensor

Structure PDCs with thickness above 500  $\mu\text{m}$  typically exhibit cracks or warping [29]-[30]. To avoid this issue, a new PDC soft-lithography fabrication method is developed to realize PDC substrates up to 1500- $\mu\text{m}$  thick without the aforementioned problems.

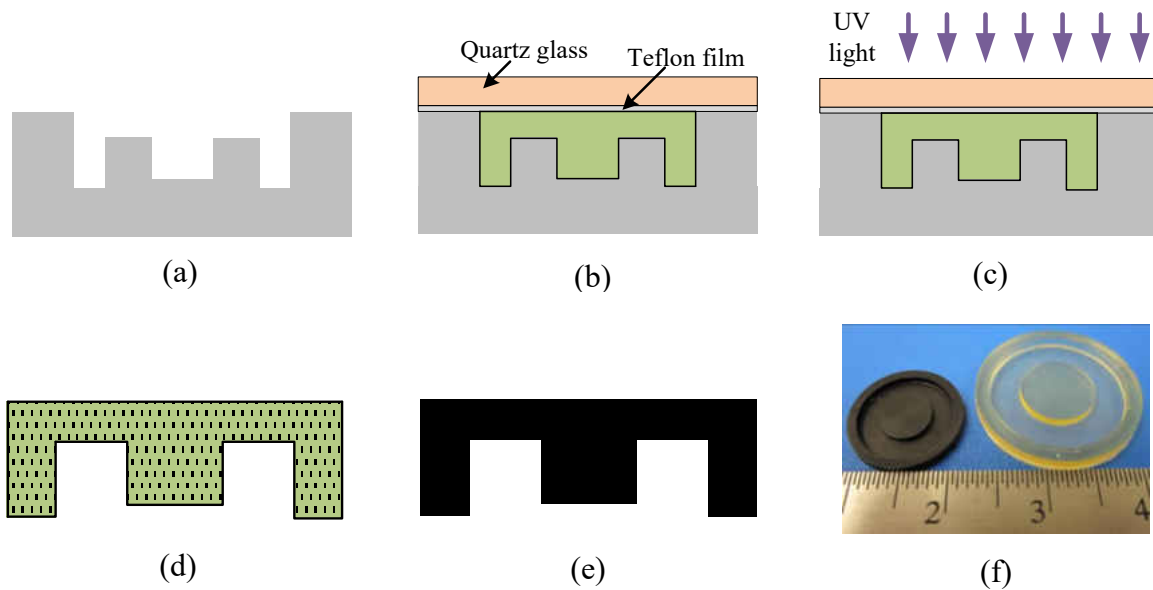


Figure 6.10: Fabrication process flow of the PDC cavity bottom. (a) Machining of the Teflon mould. (b) Liquid ceramic precursor in the mould. (c) UV exposure. (d) Polymer demoulding. (e) PDC sintering. (f) Photos of the polymer (right) and sintered PDC (left).

The fabrication process is outlined in Fig. 6.10 and described as follows. (1) Teflon is chosen as the mould material due to its non-stick and easy-to-machine properties. As shown in Fig. 6.10(a), a Teflon sheet is machined by micromilling using a three-axis machine tool with motion accuracy of  $0.25\ \mu\text{m}$  [31]. In order to compensate for the 31% dimensional shrinkage during ceramic sintering, the Teflon mould dimensions are proportionally enlarged in machining. For easier demoulding, silicon spray lubricant (3-IN-ONE 10041) is applied on the Teflon mould before the soft-lithography process. (2) The PDC precursor in liquid phase is filled into the Teflon mould as shown in Fig. 6.10(b). A quartz glass is then used to cover the top of the PDC precursor. Similarly, to avoid adhesion, a thin layer of Teflon film was attached to the quartz glass. (3) As shown in Fig. 6.10(c), the PDC precursor is exposed to UV light (Newport 66923) for 10 minutes at ambient atmosphere environment. After the lithography, the liquid ceramic precursor consisting of photo initiator is transformed into solid polymer. Then the polymer is removed from the Teflon mould, as shown in Fig. 6.10(d). (4) Pre-pyrolysis is carried out at  $150^\circ\text{C}$  for twenty-four hours in order to remove the residual stress which is generated during the fabrication process of molding and cross-linking of the polymer. After that, the polymer is pyrolyzed at  $1000^\circ\text{C}$  for four hours and converted to a fully-dense SiAlCN ceramic, as shown in Fig. 6.10(e). (5) Fig. 6.10(f) shows the pressure sensor cavity bottom before and after PDC sintering. Similarly, the cavity cap is fabricated with a thickness of  $490\ \mu\text{m}$ , compared with the design value of  $500\ \mu\text{m}$ .

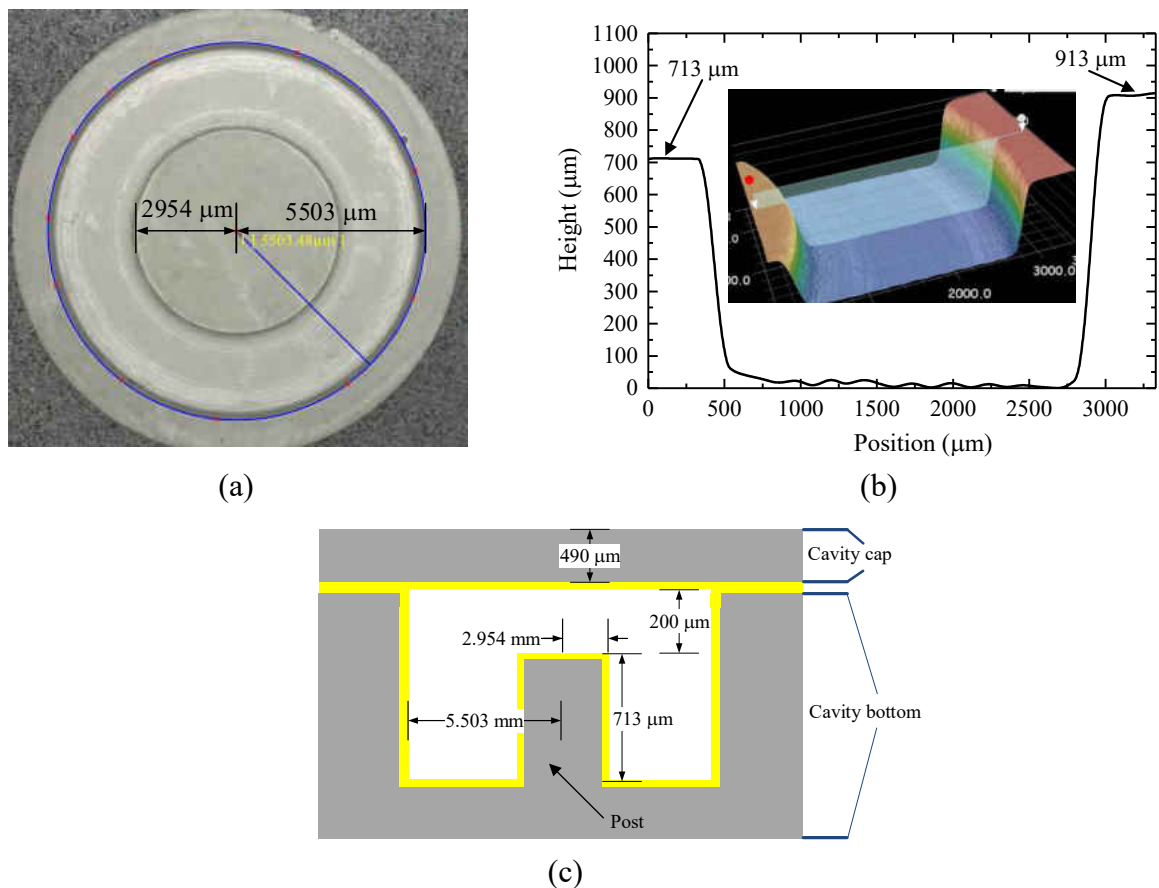


Figure 6.11: (a) Top view and (b) 3-D profile of the PDC cavity bottom after the platinum metallization. (c) Cavity dimensions after fabrication.

After the PDC machining, a thin layer of platinum is metalized on the PDC sensor bottom, which is necessary to form a microwave cavity resonator. This platinum metallization process was also used to fabricate robust antennas [28] and temperature sensors [32]. Platinum paste (ESL 5542) is applied to the PDC surface, and then dried for 2 minutes at 110°C. After that, the platinum paste is sintered at 1000°C for 10 minutes with a ramping rate of 10°C/min. The platinum paste is repeatedly applied for three times to form a thickness of approximately 25 μm without voids. Fig. 6.11(a) shows the ceramic cavity bottom after the platinum metallization. A 3-D profile of the

cavity bottom is measured by using a digital microscope (KEYENCE VHX-1000) and shown in Fig. 6.11(b). The dimensions of the metallized cavity are summarized in Fig. 6.11(c).

In the next step, platinum is patterned on both bottom and top surfaces of PDC cavity cap. As shown in Fig. 6.12(a), the PDC bottom is uniformly metalized to form the ground plane of patch antenna, except for the rectangular coupling aperture. In addition, the rectangular patch antenna is patterned and shown in Fig. 6.12(b). It should be noted that this platinum pattern process is also used to fabricate the robust interrogation antenna, which will be discussed in the Section 4.2. At last, the PDC cavity bottom and cap are bonded with a thin layer of platinum paste after a high-temperature sintering process and shown in Fig. 6.12(c).

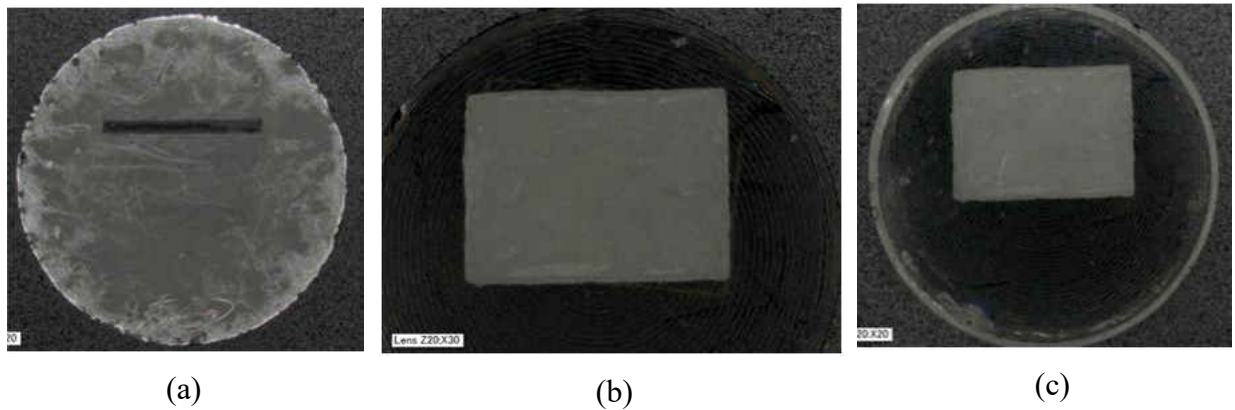


Figure 6.12: Platinum metallization and bonding process. (a) The coupling aperture on the ground plane of the patch antenna. (b) The patch antenna. (c) The bonded pressure sensor consisting of both PDC cavity bottom and cap.

#### 6.4.2 . *Fabrication of the Robust Interrogation Antenna*

The robust interrogation antenna is fabricated by using alumina substrate and platinum layer in order to survive high temperatures. The fabrication process to pattern the platinum film is specially developed and shown in Fig. 6.13. (1) The antenna layout is printed on a transfer paper by using a laser printer with a printing resolution of 1200 dpi as shown in Fig. 6.13(a). (2) A window with dimensions of  $2.5 \times 4 \text{ mm}^2$  is cut on an alumina substrate by using laser machining (Lasera Technology Corporation) as shown in Fig. 6.13(b). (3) The transfer paper is taped on the alumina substrate, while the antenna layout is aligned with the window on the alumina substrate. After a thermal compression process by using a thermal laminator, the antenna layout on the transfer paper is transferred to the alumina substrate as shown in Fig. 6.13(c). (4) Platinum paste (ESL 5542) is applied based on the transferred antenna layout under a microscope. Then the paste is dried by using a hotplate for 2 minutes at  $110^\circ\text{C}$  as shown in Fig. 6.13(d). (5) Fig. 6.13(e) shows the antenna after the high-temperature sintering process for platinum.

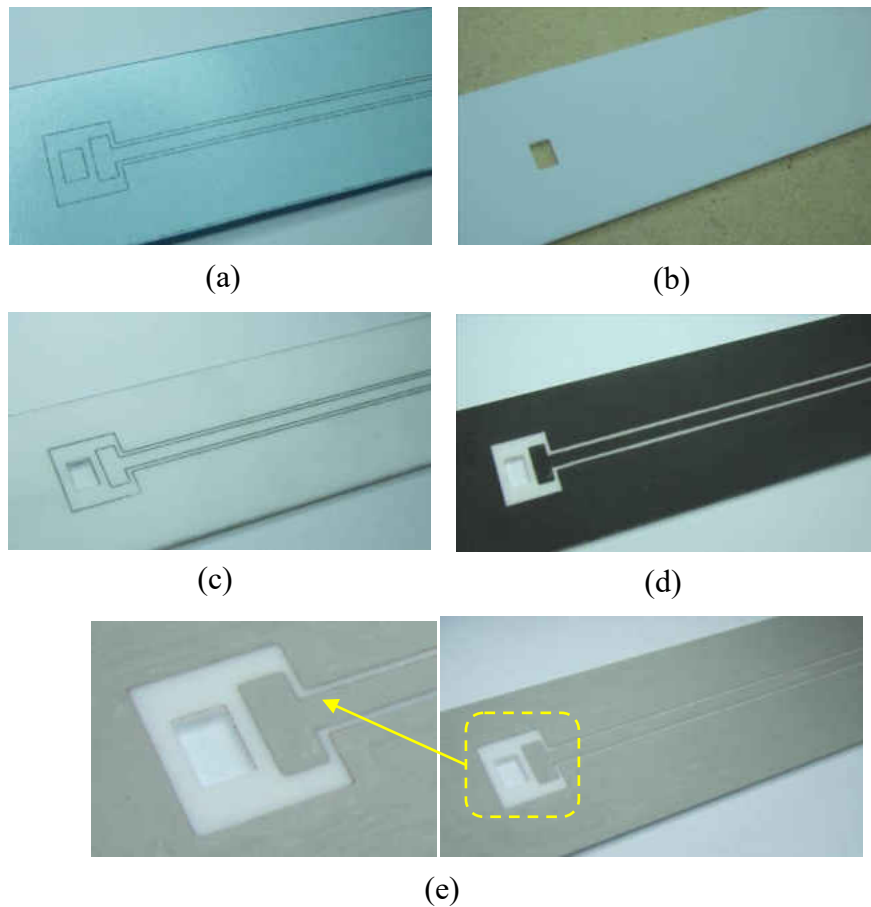


Figure 6.13: Fabrication of the robust interrogation antenna. (a) Antenna layout on a transfer paper. (b) Window cutting on an alumina substrate. (c) Antenna layout transferred to the alumina substrate. (d) Pattern of platinum paste. (e) Platinum pattern after high temperature sintering.

In order to measure the interrogation antenna, Thru-Reflect-Line (TRL) calibration is used to provide accurate antenna characterization at the reference plane as shown in Fig. 6.14 [33]. Rogers 3010 substrate, having the same dielectric constant  $\epsilon_r$  and thickness  $h$  compared with the alumina substrate, is used to fabricate the TRL calibration kits. The usage of PCB board for the calibration kits is cost effective and easy to fabricate. The fabricated calibration kits are shown in Fig. 6.14(a) and the length for Thru, Reflect and Line kits are 142 mm, 71 mm and 145.3 mm, respectively. After the TRL calibration, the interrogation antenna has a measured bandwidth of



31% at the center frequency of 11.8 GHz, which matches well with the simulation result as shown in Fig. 6.14(b).

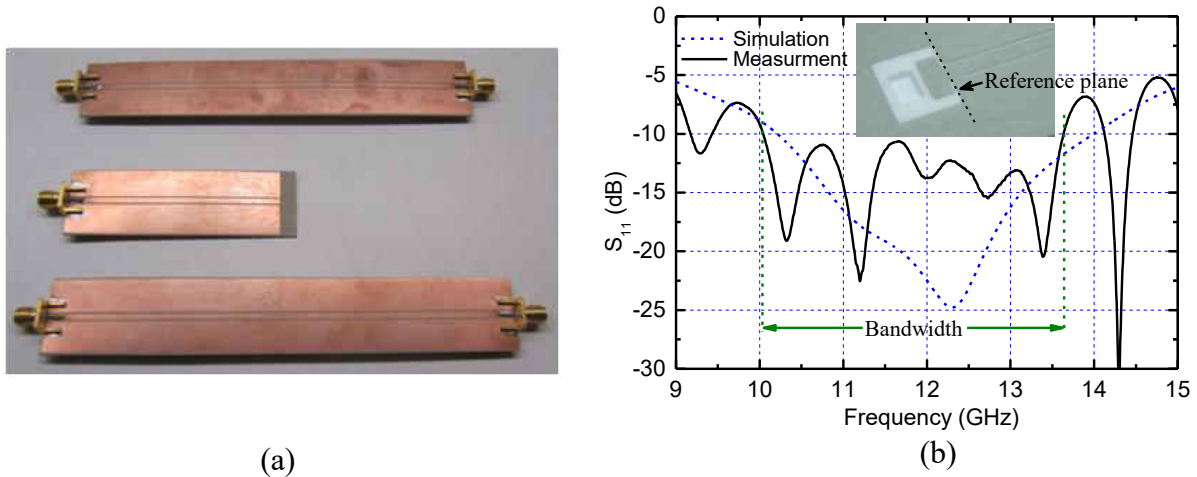


Figure 6.14: The measurement of the interrogation antenna. (a) Fabricated TRL calibration kits. (b) The measured  $S_{11}$  response of the interrogation antenna.

## 6.5 Measurement Setup and Results

A measurement setup is custom-made for the pressure measurement at high temperatures as shown in Fig. 6.15(a). A heat pad (Micropyretics Heaters International Inc.) is used to control the temperature of the pressure sensor under test with feedback from a *K*-type thermocouple (Omega HH11). A force is applied on the pressure sensor by using an alumina rod. In addition, a force gauge (Dillon GL050), attached on a test stand (Dillon CT), is used to provide precise control of applied force on the pressure sensor. Fig. 6.15(b) illustrates the detailed view of the pressure sensor under test. The alumina rod passes through the open window on the antenna substrate. Therefore, a force is applied via the alumina rod on the pressure sensor.

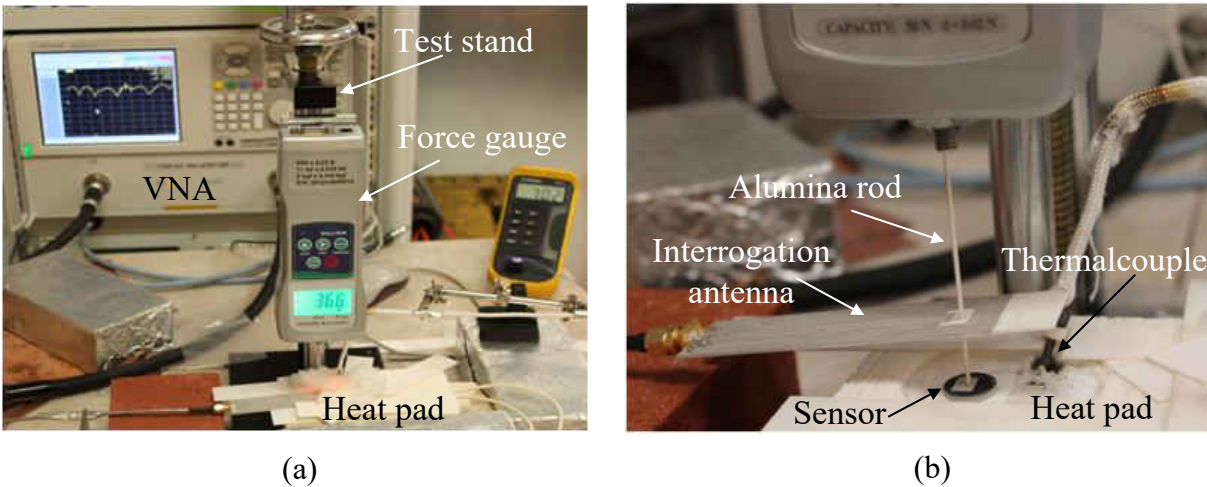


Figure 6.15: The measurement setup. (a) Pressure sensor measurement under high temperatures and external forces. (b) The external force is applied on the pressure sensor which is below the interrogation antenna.

Using this measurement setup, the pressure and temperature can be independently and simultaneously applied to the pressure sensor with precise control. Therefore, the change of the pressure sensor  $f_r$  due to the deflection of the sensor cap can be characterized at each temperature and applied force. This real-time measurement is performed with the Agilent 40-GHz PNA-L after time-domain gating [27].

The pressure sensor is measured at different temperatures up to 800°C with various forces up to 5N. The measured resonant frequency  $f_r$  is plotted in Fig. 6.16(a) for different temperatures and forces. It is observed that the  $f_r$  without applied force at room temperature is 12.2 GHz which is close to the simulated frequency of 11.9 GHz. In addition, the resonant frequency  $f_r$  decreases with the increasing applied force in a linear fashion due to reduced gap dimension. For example, the resonant frequency is reduced from 11.75 to 11.56 GHz when the external force increases from 0 to 5 Newton at 800°C. It should be noted that the resonant frequency  $f_r$  is also affected by

the temperature as shown in Fig. 6.16(a). Therefore, a temperature sensor is necessary for pressure sensor application to calibrate the frequency drift due to the temperature effect. The Q factor of the pressure sensor under 5-N loading decreases from 84.4 to 41.4 when the temperature increases from 25 to 800°C.

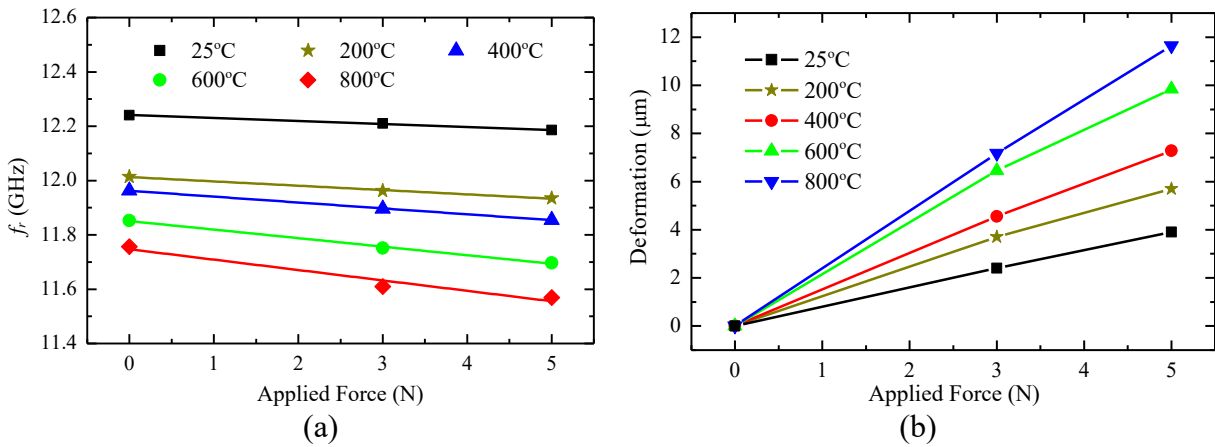


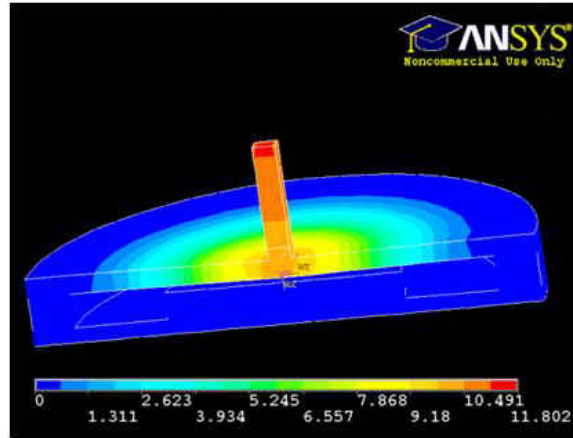
Figure 6.16: (a) Measured resonant frequency  $f_r$  of the pressure sensor versus the applied force at each temperature. (b) Extracted deflection of the pressure sensor cap due to the applied force at different temperatures.

The maximum wireless sensing range between the interrogation antenna and the pressure sensor depends on both temperature and pressure of the sensor, which correspond to different Q factors. The maximum sensing range is approximately 15 mm. This range is reduced when the temperature and pressure are raised. It is noted that a network analyzer (with limited power and dynamic range) is used for the measurement. This sensing range could be significantly increased by using customized amplification circuits. The sensor response above 800°C is not detectable, possibly due to the increased metallic loss of the platinum layer and dielectric loss of the PDC substrate. During the measurement when the applied force was above 10 N, cracks were observed inside the sensor cap, which could be due to the concentrated force within a small area

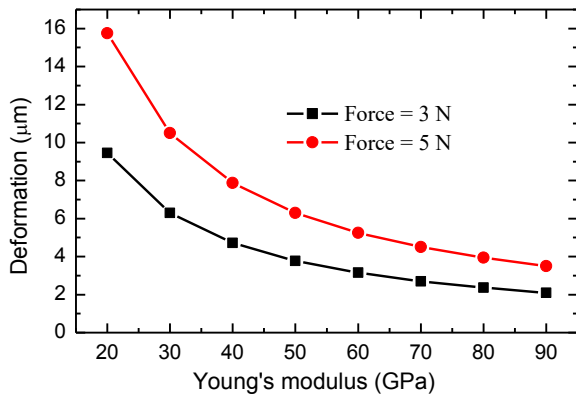
of the cap. Therefore, pressure sensor measurements were conducted for external force between 0 and 5 N to collect repeatable responses.

In order to investigate the deflection of the pressure sensor cap and estimate the change in the Young's modulus of the PDC under different temperatures, both electromagnetic and mechanical analysis is performed. By combining the slope analysis in Fig. 6.4(b) and the  $f_r$  change in Fig. 6.16(a), the cavity cap deflection versus applied force at different temperatures are calculated and plotted in Fig. 6.16(b). In addition, Fig. 6.16(b) shows that at higher temperatures, larger deflection occur for the same amount of change in the applied force, which implies a reduction in the Young's modulus of the PDC.

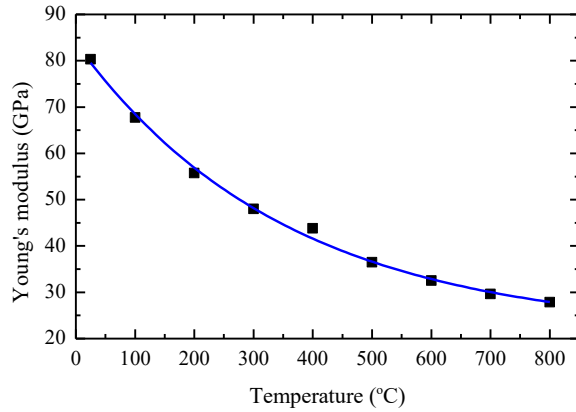
ANSYS Mechanical simulation is used to analyze the mechanical behavior of the pressure sensor with applied force for different Young's modulus. Fig. 6.17(a) shows the deflection of the PDC sensor cap corresponding to different external forces applied on the alumina rod. The maximal deflection of the sensor cap is 10.5  $\mu\text{m}$  for an applied force of 5 N, when the Young's modulus is set as 30 GPa. Additionally, the sensor deflections corresponding to applied forces of 3 and 5 N are plotted in Fig. 6.17(b) for different Young's modulus. By matching the simulated deflections in Fig. 6.17(b) with the measured results in Fig. 6.16(b), The Young's modulus of the SiAlCN PDC with different temperatures is calculated and plotted in Fig. 6.17(c). It is observed that the Young's modulus of the SiAlCN PDC is reduced from 81 to 28 GPa, when temperature is elevated from 25 to 800°C.



(a)



(b)



(c)

Figure 6.17: Mechanical analysis of the pressure sensor. (a) The pressure sensor under test simulated in ANSYS. (b) Simulated sensor deformation for different Young's modulus of the PDC. (c) Extracted Young's modulus of the PDC versus temperature.

## 6.6 Conclusion

In this chapter, we successfully demonstrated a wireless passive pressure sensor up to 800°C, owing to the robust PDC material and high-Q evanescent-mode resonator structure. This pressure sensor is compact by using an integrated patch antenna. In this research, the Young's modulus of SiAlCN PDC versus temperature was extracted in the sensor measurement. This information can be used for future pressure sensor design optimization. In addition, further

studies will be conducted in PDC material synthesis to reduce loss at high temperatures, thereby increasing the work temperatures of the pressure sensor above 1000°C. A wireless sensor test setup with ambient high temperatures and high pressures will be constructed to measure these pressure sensors.

# CHAPTER 7 SUMMARY AND FUTURE WORK

## 7.1 Summary

This dissertation presents promising solutions for temperature and pressure monitoring in harsh environment. By using robust alumina and SiAlCN substrates, temperature and pressure sensors are realized with the capacity to survive high temperatures. The two sensors are achieved with compact volume based on an integrated resonator/antenna which is also used for filter/antenna integration. In addition, robust antennas are developed for wireless interrogations of the temperature and pressure sensors. The research work in this dissertation is illustrated in Fig. 7.1.

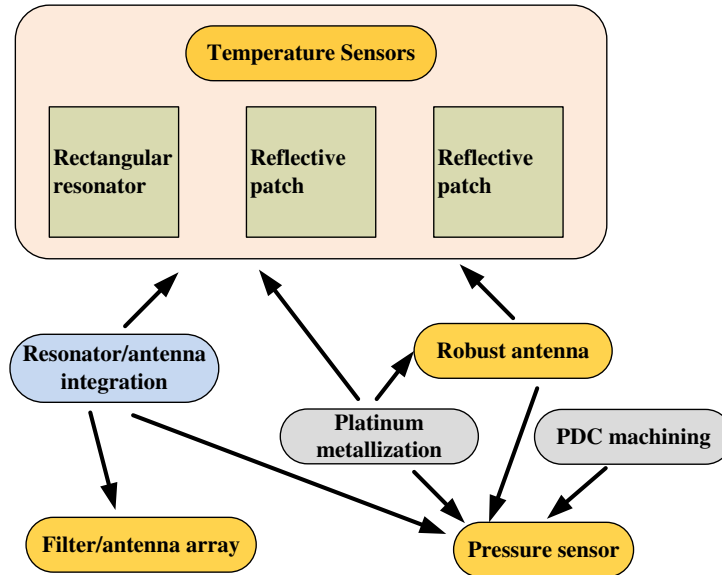


Figure 7.1: Summary map of this dissertation.

Temperature sensors based on integrated resonator/antennas and reflective patches are realized in this dissertation, respectively. Both sensors utilize the temperature-dependent alumina substrate, and the temperature is wirelessly detected by measuring the resonant frequency of the microwave resonator. The temperature sensor based on a rectangular cavity resonator minimizes the sensor dimension by adopting the seamless design between the resonator sensor and antenna. Additionally, the reflective patch sensor has an easy design and fabrication due to its planar structure. Both temperature sensors are characterized above 1000°C.

The pressure sensor is also fabricated using SiAlCN ceramics for high-temperature applications. This pressure sensor is based on an evanescent-mode resonator, and has a compact sensor size by connecting a low-profile antenna to the sensor. The pressure sensor is characterized under various pressures at high temperatures up to 800°C.

To wirelessly interrogate the temperature and pressure sensors at high temperatures, robust antennas are developed with wide bandwidth. This specially-developed antenna is able to survive a record-setting temperature of 1300°C.

Unique fabrication processes are developed for the fabrication of the sensors and antennas. Platinum metallization by using platinum paste is used to form the metal layer which is essential for microwave resonator sensors and robust antennas. Platinum pattern process enables the metal pattern on the interrogation antenna and the pressure sensor. In addition, the machining of the SiAlCN PDC, by using soft lithography, greatly improves the sintered ceramic thickness, and is used for the pressure sensor fabrication.



## 7.2 Future Work

### *7.2.1 Temperature Sensors for Harsh-Environment Applications*

Future research will include precise calibration of the sensor and will also address issues such as sensing resolution and accuracy in presence of noise and harsh and dynamic environment inside the turbine. In addition, effects of a turbine environment, including metallic obstacles, on the performance of the sensor will be evaluated in future reports. Finally, using higher transmitted power and adapting more sophisticated radar detection techniques will significantly improve the S/N ratio of the received signal, which results in better performance of the sensor.

### *7.2.2 Pressure Sensors for Harsh-Environment Applications*

Hermetic bonding of the pressure sensor can be studied for high-temperature applications in the future. The hermetic test can be carried out at room and high temperatures. Sputtering and electroplating processes can be developed to improve adhesion and reliability of platinum metallization on robust ceramic substrates. Additionally, a test environment consisting of high temperature and high pressure can be custom-made with the capacity for microwave propagation.

### *7.2.3 Robust Antennas*

Robust antennas can be developed for communication applications in harsh environment. Different types of antennas can be realized based on the application requirements. For example, an antenna array can be designed for its high directivity. In addition, the platinum metallization

process can be improved for higher metal conductivity at high temperatures, which results in higher antenna efficiency. Antenna measurement at high temperatures can be carried out with a custom-made antenna chamber.

#### *7.2.4 Multifunctional Integrated Filters*

Integration of filters and antennas with a large degree of tunability is desirable to achieve a compact and reconfigurable unit. The tunable filters can be realized by using MEMS actuators, and the antennas can be tuned with varactors. In addition, co-design of antennas, filters and LNAs as a whole unit can achieve the highest level of integration, which leads to a compact RF front-end with much lower noise figures.

## LIST OF REFERENCES

- [1] M. P. Boyce, *Gas Turbine Engineering Handbook, Third Edition*: Gulf Professional Publishing, 2006.
- [2] T. J. Carter, "Common failures in gas turbine blades," *Eng. Fail. Anal.*, vol. 12, pp. 237-247, 2005.
- [3] N. Eliaz, G. Shemesh, and R. Latanision, "Hot corrosion in gas turbine components," *Eng. Fail. Anal.*, vol. 9, pp. 31-43, 2002.
- [4] M. Moore, "NOx emission control in gas turbines for combined cycle gas turbine plant," *P. I. Mech. Eng. A-J. Pow*, vol. 211, pp. 43-52, 1997.
- [5] S. M. Sze and K. K. Ng, *Physics of semiconductor devices*: Wiley. com, 2006.
- [6] P. G. Neudeck, S. L. Garverick, D. J. Spry, L. Y. Chen, G. M. Beheim, M. J. Krasowski, and M. Mehregany, "Extreme temperature 6H - SiC JFET integrated circuit technology," *physica status solidi (a)*, vol. 206, pp. 2329-2345, 2009.
- [7] A. C. Patil, X.-a. Fu, M. Mehregany, and S. L. Garverick, "Fully-monolithic, 600 °C differential amplifiers in 6H-SiC JFET IC technology," in *IEEE CICC*, San Jose, CA, Sept. 13-16, 2009 pp. 73-76.
- [8] P. Herfurth, D. Maier, L. Lugani, J.-F. Carlin, R. Rösch, Y. Men, N. Grandjean, and E. Kohn, "Ultrathin Body InAlN/GaN HEMTs for High-Temperature (600° C) Electronics," 2013.
- [9] J. Yang, "A Silicon Carbide Wireless Temperature Sensing System for High Temperature Applications," *Sensors*, vol. 13, pp. 1884-1901, 2013.
- [10] J. Yang, "A Harsh Environment Wireless Pressure Sensing Solution Utilizing High Temperature Electronics," *Sensors*, vol. 13, pp. 2719-2734, 2013.
- [11] Z. Zhang, K. Grattan, and A. Palmer, "Fiber - optic high - temperature sensor based on the fluorescence lifetime of alexandrite," *Rev. Sci. Instrum.*, vol. 63, pp. 3869-3873, 1992.
- [12] S. Fricke, A. Friedberger, H. Seidel, and U. Schmid, "A robust pressure sensor for harsh environmental applications," *Sens. Actuators A*, vol. 184, pp. 16-21, 2012.
- [13] S. Guo, H. Eriksen, K. Childress, A. Fink, and M. Hoffman, "High temperature smart-cut SOI pressure sensor," *Sens. Actuators A*, vol. 154, pp. 255-260, 2009.

- [14] D. J. Young, J. Du, C. A. Zorman, and W. H. Ko, "High-temperature single-crystal 3C-SiC capacitive pressure sensor," *IEEE Sensors J.*, vol. 4, pp. 464-470, 2004.
- [15] Q. Tan, C. Li, J. Xiong, P. Jia, W. Zhang, J. Liu, C. Xue, Y. Hong, Z. Ren, and T. Luo, "A High Temperature Capacitive Pressure Sensor Based on Alumina Ceramic for in Situ Measurement at 600° C," *Sensors*, vol. 14, pp. 2417-2430, 2014.
- [16] P. Childs, J. Greenwood, and C. Long, "Review of temperature measurement," *Rev. Sci. Instrum.*, vol. 71, pp. 2959-2978, 2000.
- [17] M. Sen and H. Shan, "A review of electrochemical macro-to micro-hole drilling processes," *Int. J. Mach. Tool. Manu.*, vol. 45, pp. 137-152, 2005.
- [18] H. A. Walter, H. Honen, and H. E. Gallus, "Adaptor for monitoring a pressure sensor to a gas turbine housing," US5612497 A, 1997.
- [19] M. A. Fonseca, J. M. English, M. Von Arx, and M. G. Allen, "Wireless micromachined ceramic pressure sensor for high-temperature applications," *J. Microelectromech. Syst.*, vol. 11, pp. 337-343, 2002.
- [20] J. Xiong, Y. Li, Y. Hong, T. Cui, Q. Tan, S. Zheng, and T. Liang, "Wireless LTCC-based Capacitive Pressure Sensor for Harsh Environment," *Sens. Actuators A*, vol. 197, pp. 30-37, 2013.
- [21] E. D. Birdsell, J.-W. Park, and M. G. Allen, "Wireless ceramic sensors operating in high temperature environments," in *40 th AIAA/ASME/SAE/ASEE Joint Propulsion Conference*, Fort Lauderdale, FL, July 11-14, 2004
- [22] Q. Tan, H. Kang, J. Xiong, L. Qin, W. Zhang, C. Li, L. Ding, X. Zhang, and M. Yang, "A Wireless Passive Pressure Microsensor Fabricated in HTCC MEMS Technology for Harsh Environments," *Sensors*, vol. 13, pp. 9896-9908, 2013.
- [23] A. Canabal, P. Davulis, G. Harris, and M. Pereira da Cunha, "High-temperature battery-free wireless microwave acoustic resonator sensor system," *Electronics letters*, vol. 46, pp. 471-472, 2010.
- [24] A. Canabal, P. Davulis, T. Pollard, and M. Pereira da Cunha, "Multi-sensor wireless interrogation of SAW resonators at high temperatures," in *IEEE Int. Ultrasonics Symp.*, San Diego, CA Oct. 11-14, 2010 pp. 265-268.
- [25] H. Fritze, "High-temperature piezoelectric crystals and devices," *J. Electroceramic.*, vol. 26, pp. 122-161, 2011.

- [26] R. Fachberger, G. Bruckner, R. Hauser, J. Biniash, L. Reindl, and C. Ruppel, "Properties of radio frequency Rayleigh waves on Langasite at elevated temperatures," in *IEEE Int. Ultrasonics Symp.*, Montreal, Quebec, Canada, Aug. 23-27, 2004 pp. 1223-1226.
- [27] G. E. Ponchak, J. L. Jordan, and M. C. Scardelletti, "High temperature characteristics of coplanar waveguide on r-plane sapphire and alumina," *IEEE Trans. Adv. Packag.*, vol. 32, p. 146, 2009.
- [28] M. C. Scardelletti, J. L. Jordan, and G. E. Ponchak, "Temperature Dependency (25°C-400°C) of a Planar Folded Slot Antenna on Alumina Substrate," *IEEE Antennas Wireless Propag. Lett.*, vol. 7, pp. 489-492, 2008.
- [29] G. E. Ponchak, J. L. Jordan, and M. C. Scardelletti, "Temperature dependence of thin film spiral inductors on alumina over a temperature range of 25 to 475 C," in *Proc. Electron. Compon. Technol. Conf.*, Las Vegas, NV, June 1-4, 2010 pp. 713-719.
- [30] S. Fargeot, D. Guihard, and P. Lahitte, "Dielectric characterization at high temperature (1600° C) for space applications," in *Proc. IEEE Int. Conf. Microw. Technol. Comput. Electromagn.*, Beijing, China, May 22-25, 2011 pp. 48-50.
- [31] R. Raj, L. An, S. Shah, R. Riedel, C. Fasel, and H. J. Kleebe, "Oxidation kinetics of an amorphous silicon carbonitride ceramic," *J. Am. Ceram. Soc.*, vol. 84, pp. 1803-1810, 2001.
- [32] L. An, R. Riedel, C. Konetschny, H. Kleebe, and R. Raj, "Newtonian viscosity of amorphous silicon carbonitride at high temperature," *J. Am. Ceram. Soc.*, vol. 81, pp. 1349-1352, 1998.
- [33] Z. C. Wang, F. Aldinger, and R. Riedel, "Novel Silicon - Boron - Carbon - Nitrogen Materials Thermally Stable up to 2200° C," *J. Am. Ceram. Soc.*, vol. 84, pp. 2179-2183, 2001.
- [34] Y. Wang, W. Fei, Y. Fan, L. Zhang, W. Zhang, and L. An, "A silicoaluminum carbonitride ceramic resist oxidation/corrosion in water vapour," *J. Mater. Res.*, vol. 21, pp. 1625-1628, 2006.
- [35] L. An, Y. Wang, L. Bharadwaj, L. Zhang, Y. Fan, D. Jiang, Y. Sohn, V. H. Desai, J. Kapat, and L. C. Chow, "Silicoaluminum Carbonitride with Anomalously High Resistance to Oxidation and Hot Corrosion," *Adv. Eng. Mater.*, vol. 6, pp. 337-340, 2004.
- [36] X. Ren, S. Ebadi, Y. Chen, A. Linan, and X. Gong, "Characterization of SiCN Ceramic Material Dielectric Properties at High Temperatures for Harsh Environment Sensing Applications," *IEEE Trans. Microw. Theory Tech.*, vol. 61, pp. 960-971, 2013.

- [37] L.-A. Liew, W. Zhang, V. M. Bright, L. An, M. L. Dunn, and R. Raj, "Fabrication of SiCN ceramic MEMS using injectable polymer-precursor technique," *Sens. Actuators A*, vol. 89, pp. 64-70, 2001.
- [38] D. Seo, S. Jung, S. J. Lombardo, Z. Feng, J. Chen, and Y. Zhang, "Fabrication and electrical properties of polymer-derived ceramic (PDC) thin films for high-temperature heat flux sensors," *Sens. Actuators A*, vol. 165, pp. 250-255, 2011.
- [39] J. Chuang, D. Thomson, and G. Bridges, "Embeddable wireless strain sensor based on resonant RF cavities," *Rev. Sci. Instrum.*, vol. 76, pp. 094703-094703-7, 2005.
- [40] D. Thomson, D. Card, and G. Bridges, "RF cavity passive wireless sensors with time-domain gating-based interrogation for SHM of civil structures," *IEEE Sensors J.*, vol. 9, pp. 1430-1438, 2009.
- [41] X. Gong, W. J. Chappell, and L. Katehi, "Reduced size capacitive defect EBG resonators," in *IEEE MTT-S Int. Microw. Symp. Dig.*, Seattle, WA, June 2-7, 2002 pp. 1091-1094.
- [42] D. Senior, X. Cheng, P. Jao, C. Kim, J. Kim, and Y. Yoon, "Wireless passive sensing application using a cavity loaded evanescent mode half mode substrate integrated waveguide resonator," in *16th International TRANSDUCERS conference*, Beijing, China, June 5-9, 2011 pp. 2014-2017.
- [43] M. Jatlaoui, F. Chebila, P. Pons, and H. Aubert, "Working principle description of the wireless passive EM transduction pressure sensor," *Eur. Phys. J-Appl. Phys.*, vol. 56, p. 1281, 2011.
- [44] Y. Zhao, Y. Li, B. Pan, S.-H. Kim, Z. Liu, M. M. Tentzeris, J. Papapolymerou, and M. G. Allen, "RF evanescent-mode cavity resonator for passive wireless sensor applications," *Sens. Actuators A*, vol. 161, pp. 322-328, 2010.
- [45] X. Ren, S. Ebadi, and X. Gong, "A single-antenna wireless passive temperature sensing mechanism using a dielectrically-loaded resonator," in *IEEE AP-S Int. Symp.*, Chicago, IL, July 8-14, 2012 pp. 1-2.
- [46] X. Ren, S. Ebadi, H. Cheng, Y. Chen, L. An, and X. Gong, "Wireless resonant frequency detection of SiCN ceramic resonator for sensor applications," in *IEEE AP-S Int. Symp.*, Spokane, WA, July 3-8, 2011 pp. 1856-1859.
- [47] L. Harle and L. P. Katehi, "A vertically integrated micromachined filter," *IEEE Trans. Microw. Theory Tech.*, vol. 50, pp. 2063-2068, 2002.

- [48] K. Ahn and I. Yom, "A Ka-band multilayer LTCC 4-pole bandpass filter using dual-mode cavity resonators," in *IEEE MTT-S Int. Microw. Symp. Dig.*, Atlanta, GA, June 15-20, 2008 pp. 1235-1238.
- [49] J.-H. Lee, N. Kidera, G. DeJean, S. Pinel, J. Laskar, and M. M. Tentzeris, "A V-band front-end with 3-D integrated cavity filters/duplexers and antenna in LTCC technologies," *IEEE Trans. Microw. Theory Tech.*, vol. 54, pp. 2925-2936, 2006.
- [50] Y. Yusuf and X. Gong, "Compact Low-Loss Integration of High-Q 3-D Filters With Highly Efficient Antennas," *IEEE Trans. Microw. Theory Tech.*, vol. 59, pp. 857-865, 2011.
- [51] R. J. Cameron, C. M. Kudsia, and R. R. Mansour, *Microwave filters for communication systems: fundamentals, design, and applications* vol. 1: Wiley-Interscience, 2007.
- [52] "simplified filter tuning using time domain," *Application Note 1287-8*, Agilent Technologies Corp. 2001.
- [53] S. Scott and D. Peroulis, "A capacitively-loaded MEMS slot element for wireless temperature sensing of up to 300 C," in *IEEE MTT-S Int. Microw. Symp. Dig.*, Boston, MA, June 7-12, 2009 pp. 1161-1164.
- [54] Y. Yusuf and X. Gong, "A new class of 3-D filter/antenna integration with high quality factor and high efficiency," in *IEEE MTT-S Int. Microw. Symp. Dig.*, Anaheim, CA May 23-28, 2010 pp. 892-895.
- [55] Z. Ma and Y. Kobayashi, "Error analysis of the unloaded Q-factors of a transmission-type resonator measured by the insertion loss method and the return loss method," in *IEEE MTT-S Int. Microw. Symp. Dig.*, Seattle, WA, June 2-7, 2002 pp. 1661-1664 vol.3.
- [56] H. A. Haus, *Waves and fields in optoelectronics* vol. 1: Prentice-Hall Englewood Cliffs, NJ, 1984.
- [57] "Time Domain Analysis using a Network Analyzer," *Agilent Application Note 1287-12*, Agilent Technologies Corp. 2007.
- [58] H. Cheng, S. Ebadi, X. Ren, Y. Yusuf, and X. Gong, "A compact wireless passive sensing mechanism based on a seamlessly integrated resonator/antenna," in *IEEE AP-S Int. Symp.*, Spokane, WA, July 3-8, 2011 pp. 1350-1353.
- [59] H. Cheng, Y. Yusuf, and X. Gong, "Vertically Integrated Three-Pole Filter/Antennas for Array Applications," *IEEE Antennas Wireless Propag. Lett.*, vol. 10, pp. 278-281, 2011.

- [60] Y. Yusuf, H. Cheng, and X. Gong, "A Seamless Integration of 3-D Vertical Filters With Highly Efficient Slot Antennas," *IEEE Trans. Antennas Propag.*, vol. 59, pp. 4016-4022, 2011.
- [61] Y. Yusuf, C. Haitao, and G. Xun, "Co-designed substrate-integrated waveguide filters with patch antennas," *IET Microwaves, Antennas & Propagation*, vol. 7, pp. 493-501, 2013.
- [62] Y. Yusuf and X. Gong, "Integration of three-dimensional high-Q filters with aperture antennas and bandwidth enhancement utilising surface waves," *IET Microwaves, Antennas, Propagat.*, vol. 7, pp. 468-475, 2013.
- [63] M. Violetti, J.-F. Zurcher, J. Geisheimer, and A. K. Skrivervik, "Design of antenna based sensors for blade tip clearance measurement in gas turbines," in *Proc. EuCAP*, 2010 pp. 1-4.
- [64] E. Walton, J. Young, J. Moore, and K. Davis, "EM propagation in jet engine turbines," *Proc. AMTA Meeting*, 2006.
- [65] C. A. Balanis, *Antenna theory: analysis and design*: John Wiley & Sons, 2012.
- [66] R. Garg, P. Bhartia, I. Bahl, and A. Ittipiboon, *Microstrip antennas design handbook*: Artech House, 2001.
- [67] H. Cheng, S. Ebadi, and X. Gong, "A Low-Profile Wireless Passive Temperature Sensor Using Resonator/Antenna Integration Up to 1000°C," *IEEE Antennas Wireless Propag. Lett.*, vol. 11, pp. 369-372, 2012.
- [68] H.-D. Chen, "Broadband CPW-fed square slot antennas with a widened tuning stub," *IEEE Trans. Antennas Propag.*, vol. 51, pp. 1982-1986, 2003.
- [69] R. Hauser, R. Fachberger, G. Bruckner, R. Reicher, and W. Smetana, "Ceramic patch antenna for high temperature applications," in *Proc. 28th ISSE*, Wiener Neustadt, May. 19-22, 2005 pp. 159-164.
- [70] H. Cheng, X. Ren, S. Ebadi, and X. Gong, "A Wide-band Square Slot Antenna for High-Temperature Applications," in *IEEE AP-S Int. Symp.*, Orlando, FL, July 7-13, 2013 pp. 242-243.
- [71] "Agilent network analysis applying the 8510 TRL calibration for non-Coaxial measurements," *Agilent Technologies Corp.*, Santa Clara, CA, Product note 8510-8A 2001.